Low-Cost, High Performance Solar Vapor Generation

By

George Wei Ni

Submitted to the Department of Mechanical Engineering
in partial fulfillment of the requirements for the degree of

Doctor of Philosophy
at the
MASSACHUSETTS INSTITUTE OF TECHNOLOGY
February, 2018

© Massachusetts Institute of Technology 2018. All Rights Reserved

Signature redacted

Author .....
.....
Department of Mechanical Engineering
January 15th, 2018

Signature redacted

Certified by.....
.....
Gang Chen
Department Head
Carl Richard Soderberg Professor of Power Engineering
Thesis Supervisor

Signature redacted

Accepted by.....
Rohan Abeyaratne
Chairman, Department Committee on Graduate Theses

ARCHIVES
MASSACHUSETTS INSTITUTE OF TECHNOLOGY
FEB 09 2018
LIBRARIES

MIT Libraries

77 Massachusetts Avenue
Cambridge, MA 02139
http://libraries.mit.edu/ask

DISCLAIMER NOTICE

Due to the condition of the original material, there are unavoidable flaws in this reproduction. We have made every effort possible to provide you with the best copy available.

Thank you.

The images contained in this document are of the best quality available.

Low-Cost, High Performance Solar Vapor Generation

by

George Wei Ni

Submitted to the Department of Mechanical Engineering on January 15, 2018,
in partial fulfillment of the requirements for the degree of Doctor of Philosophy

Abstract

Sustainable access to energy and access to water are two of the defining technological problems that society currently faces. Threats of climate change and depletion of fossil fuel reserves are forcing a shift towards more renewable sources of energy, such as solar energy and others. At the same time, water resources are becoming scarcer, caused by unsustainable extraction of ground water resources. Current projections show that by 2025, the population of people living in water-stressed areas is expected to increase to 3.9 billion. Exacerbating this problem is continuing urbanization, which stresses local water supplies further. The two problems of energy and water are inextricably tied together. Water processing, such as desalination and wastewater management, fundamentally requires energy inputs, while energy production often requires water for operational cooling.

This thesis focuses on developing technologies for low-intensity utilization of solar energy for desalination and wastewater management. Traditional solar thermal technologies collect sunlight, and use motorized optical concentrators to concentrate the weak solar flux to create high temperature steam, often 400°C or higher. These optical concentrators are costly and require maintenance that are unattractive in many small-scale and low-intensity applications. These applications include distributed desalination, medical sterilization, wastewater management, and more. In this thesis, the research has focused on 1) evaporation mechanisms in nanofluids for solar applications, 2) a solar steam generation structure that operates without optical concentrators, and 3) a floating solar still that produces water without the need for periodic cleaning of excess salts, and has a material cost of $3 to supply individual daily drinking water needs, which can be paid back quickly for some regions like the Maldive.

One of the first approaches to solar vapor generation was to use nanoparticles suspended in water, or nanofluids, to localize solar absorption to near the evaporation surface. This approach reduces the temperature drop between the heat generation site and the evaporation surface, increasing the evaporation rate. This thesis first explores the vapor generation mechanisms in nanofluid-based solar vapor generation, and develops a small-scale nanofluid-based solar receiver that could generate vapor at 70% efficiency. A theory was developed to show how nanoparticle suspension could affect the nanofluid transient performance.

This thesis next demonstrates a small-scale floating solar steam generator, that does not require optical concentration. This was achieved by further extending the heat localization concept, using various widely available materials to reduce radiative, convective, and conductive losses. By reconfiguring the device, steam at 100°C or vapor at 70% efficiency could be produced. The basic steam generator was then improved and adapted to reject excess salts left behind from vapor formation. The salt rejecting structure was coupled with a condensation cover, to form a floating solar still that was demonstrated to operate in the ocean, simultaneously producing drinkable water and rejecting the excess salts. Salt rejection experiments were conducted to prove the long-term ability of the structure to operate in saline waters.

Thesis Supervisor: Gang Chen

Title: Department Head, Carl Richard Soderberg Professor of Power Engineering

Acknowledgements

I appreciate the support from the innumerable people I've met during my time at MIT. My PhD advisor, Professor Gang Chen, has made my achievements possible through his patient yet demanding mentorship. I am indebted to his relentless drive for perfection, his willingness to spend long hours reviewing my work, as well as his trust in giving me space to decide my research directions. I feel lucky to have met Gang, knowing that many other graduate students end up in poor relationships with their advisors.

The NanoEngineering group has comprehensively supported my development as a researcher. In my earlier years, I marveled at how knowledgeable and confident the senior students appeared. Each student had an impressive breadth of knowledge, from traditional mechanical engineering topics such as heat transfer and device fabrication in the machine shop, to interdisciplinary topics such as near-field radiation, semi-classical models for energy transport, and semiconductor devices like photovoltaic cells. Ken McEnaney, Kimberlee Collins, Daniel Kraemer, Maria Luckyanova, Matthew Branham, Poetro Sambegoro, Sangyeop Lee, Qing Hu, Austin Minnich, Sheng Shen, Andy Muto, and others exemplified this. Other students opened my eyes to new areas, such as entrepreneurship (Anurag Bajpayee), which would play a role in my later years as a student funded under an entrepreneurship-minded project. Now, in my waning months as a graduate student, I am impressed with the quality of the junior students. Although they are still learning, they are confident enough to discuss research problems with faculty and senior researchers. I am fortunate to have met Jiawei Zhou, Laureen Meroueh, Yi Huang and many others. Most importantly, my peers have provided a sense of camaraderie, through professional and personal discussions, and most importantly for me, a benchmark for my own progress. My cohorts include Bolin Liao, Lingping Zeng, Edi Hsu, Jonathan Tong, Lee Weinstein, Jonathan Mendoza, Vazrik Chiloyan, Sam Huberman, Jianjian Wang. I will always remember my initial years in graduate school, doing homework in the evenings in the lab, and grabbing people to eat dinner in Chinatown on Friday nights. Without the companionship of the NanoEngineering group, my graduate studies would have been far more difficult.

The postdocs and research scientists of the NanoEngineering group hold a special place in my academic heart, for I have worked most closely with them. They provided a level of guidance that complemented Gang's: whereas Gang showed me where I needed to be, the NanoEngineering staff made me believe that I could find my own way there. I thank Dr. Hadi Ghasemi, Dr. Nenad Miljkovic, Dr. Svetlana V. Boriskina, Dr. Hadi Zandavi, and Dr. Thomas Cooper for the chance to work with them, learn from them, and grow through them. Dr. Ghasemi was indispensable in revitalizing my academic career after my difficult Master's work. Dr. Miljkovic provided an optimistic voice in helping me publish my first research paper. Dr. Svetlana V. Boriskina was instrumental in helping me write my second research paper, published in the prestigious Nature family of journals, despite having little prior knowledge in the field. She has also provided invaluable insight as a senior researcher, and has provided many new views on academia and politics. Dr. Zandavi has worked closely with me on the last topic of my thesis work, and I find working with him to be a joy. He brings not only a rich expertise in phase change physics, but a collegial and friendly working environment. I have worked with Dr. Thomas Cooper less than the others, but I have been most impressed with his engineering knowledge and competence. One of my regrets is not having been more involved in his projects.

As any graduate student knows, the friends you make during your program can make all the difference. I have had the privilege of being surrounded by many friendly faces during my time at MIT. I was lucky to have many alumni from the University of Michigan join me here in Boston, including Jeremy Cho, Doug Yeung, Eric Liao, Teresa Wang, Kris Kojian. We spent many weekends together watching Michigan football and basketball. Despite my initial reservations about the locals, I met many wonderful people from Boston, including my neighbors Leona, Michael, and Luis. At MIT, I found a chance to learn ice hockey, a lifelong dream. I now play hockey several times a week with the local hockey community, which keeps me physically healthy, and allows me to meet people from all walks of life. These people include from MIT (Bill McBride, Chad Martinovich, Dave Hunter, Evelina Polyzoeva, Sasha Soane, Niki Jepsen, Yury Polyanskiy, Timur, Rvachov, Brian Callahan, Fritzy, the Harvard Saturday morning Physics group, David Autor, Neil Thompson, Nathaniel Hendren, the rest of Jerry's Kids hockey (who introduced me to hockey), all the people of GAME hockey (Mechanical Engineering, Brooks Reed, David Bierman, Chris Bachman, Patrick Barragan, Tyler Wortman, David Taylor, Arny Leroy, Claudio Hail, and more), the Physics Department Annihilation Operators team, the

recreational hockey group (Michael Fahie, Dan Logcher, George, Tommy, Professor Wornell, and more), and the Malden summer hockey group (Nic and Mark Rinaldi, Alex Wing Lake Yee, Matt Li, Sherry Chu, Jennifer Tang, Eddie, and tons more). I met many students from other universities in the area, either from living near Boston University, or by ice skating there (Dela Bai, Rob).

I want to make special mention of my motorcycle (a yellow Kawasaki 2002 ZX-6R), which provided me endless hours of joy and discovery. The motorcycle taught me to be independent, at a time when I had few friends in Boston. I explored little crooks and niches of different neighborhoods in Boston, from the upscale Seaport district, all the way to blue-collar Dorchester and Quincy. I eventually made my way all over New England (with just Vermont left to visit). The motorcycle also taught me to how to work on mechanical devices, and I bought my first tool set trying to change the air filters. The mechanical experiences translated over to my research, influencing my experimental design and device fabrication.

Finally, I thank my parents, my brother Andy, and my sweet and supportive wife Wenjia for their continuing support, their patience, and their excitement for my successes. Although my son Adam was not born until a week before my thesis defense, he is here to provide new experiences as I turn to the next chapter of my life.

Contents

List of Figures

Chapter 1

1. Introduction

Access to sustainable energy and water sources are the defining engineering challenges of our times. Our reliance on fossil fuels to power society's industrialization has increased atmospheric greenhouse gas concentrations, overwhelmingly considered to foreshadow climate change. Among the many dire consequences predicted include significant rise in sea level, from 10-100cm by 2100,[1,2] which will displace up to 13 million people in the continental US alone.[3] Despite the inundation of inhabited areas with rising seas, the Earth's populations are increasingly experiencing a shortfall in freshwater, with 4 billion people facing water scarcity for more than one month each year.[4] Desalination of otherwise unsuitable water for drinking purposes has thus far provided less than one percent of the total global water consumption, yet consumes nearly the same percentage of total global power production.[5] Clearly, parallel problems of energy and water access are entwined. This thesis aims to attack both problems by harnessing the abundant energy of the sun to drive solutions in water consumption and management.

1.1. The Current Energy Landscape

The world's energy consumption is expected to continue to accelerate, as developing countries outside of the Organization for Economic Cooperation and Development (OECD) continue to modernize. Global energy consumption is expected to grow 240,000 TWh in 2040, up 48% from 2012.[6] Although OECD countries such as the US have maintained or even decreased their energy consumption in recent years,[7] non-OECD countries are expected to increase consumption 71% over current levels. New sources of renewable energy are needed to help non-OECD countries achieve sustainable power generation.

Current sources of energy can be split into three main types: fossil fuels, nuclear fuels, and renewables. Fossil fuels have historically provided the bulk of directly harvested energy, and come from sources such as coal, natural gas, and various petroleum products. Fossil fuels provide over three-quarters of our energy consumption, but are by far the largest emitters of the

greenhouse gases responsible for climate change. Carbon dioxide, or CO_2, is a direct waste product of the combustion reaction used to generate energy. Nuclear fuel sources, in contrast, generate very little CO_2 during energy generation, but have their own disadvantages. The general public is wary of connections with nuclear weapons and widely publicized nuclear accidents in Chernobyl, Ukraine, Three-Mile Island in the US, and Fukushima, Japan. Furthermore, though nuclear power waste products are relatively small in volume, their radioactivity can last for thousands of years. In the US, storage of nuclear waste has a history of contention. These effects have limited nuclear to supply less than 5% of global power consumption. Last, we have various types of renewable energy sources, ranging from hydro, biomass, wind, geothermal, solar, and more. Renewable energy has recently outpaced nuclear energy, providing nearly 12% of global power consumption in 2012. Numerous technical challenges remain in integrating renewable energy sources with traditional energy infrastructures, but renewable sources remain among the most promising to support a future independent of greenhouse gas emissions.

1.2. Solar Energy as an Abundant Source

A tantalizing renewable source, solar energy is the origin of most other energy sources, and the most abundant of them all. Solar energy is so abundant that the globally incident energy in one hour is enough to satisfy *annual* global energy consumption. Furthermore, sunlight is available nearly everywhere, in contrast to other energy sources such as hydro and geothermal. Despite these great advantages, solar energy use has thus far been limited primarily due to its dispersed nature. The average peak solar intensity is roughly only 1kW per square meter, and varies with latitude as well as climate. The dispersed nature requires large and expensive collectors to be used to capture sunlight over broad areas.

Various standards are used to characterize solar intensity, the energy flux per area per unit time, as it passes through the atmosphere. ASTM G-173-03 is the most commonly used one, correlating with the solar intensity at a latitude corresponding with the center of global population density. As sunlight pass through the atmosphere, a portion arrives at Earth diffusely due to atmospheric scattering, while the remainder passes directly through the atmosphere. ASTM G-173-03 is split into AM1.5G, which includes all solar intensity incident on an area from a hemisphere, and AM1.5D, which only includes solar intensity directly from the sun and a

cone 2.5° surrounding the sun. Factors such as humidity, atmospheric dust, and cloud cover can change the ratio of scattered and directly transmitted sunlight.

Current solar technology can be categorized as either photovoltaic technologies, or solar thermal technologies. These technologies use electric fields and optics, respectively, to capture and concentrate solar energy. Photovoltaic technologies directly convert sunlight into electricity, and have the advantages in modularity and cost. Solar thermal technologies convert sunlight into thermal energy, which can be directly used for heating or further converted into electrical energy. Solar thermal is advantageous for the ease of storing generated energy for dispatchable use, such as nighttime electricity generation. The generated heat energy can also be used in a wide variety of applications. Examples of solar thermal technologies include solar hot water heaters,[8] which are used worldwide in residential roof-top installations, and concentrated solar power installations,[9] which use large fields of concentrating optics to generate high temperature steam for electricity generation.

1.3. Increasing Water Scarcity

Freshwater sources are becoming increasingly scarce. A primary reason for increasing scarcity is the over reliance of groundwater sources in certain regions, which may be counterintuitive when considering nature's closed-loop water cycle. However, the scarcity results from a mismatch in withdrawal and recharge rates, owing to groundwater's drastically slow recharge rate.[10] Flow in aquifers can be as slow as feet per year or decade, rendering aquifers as essentially finite reservoirs of freshwater, similar to petroleum deposits. Other causes of increasing freshwater scarcity can be attributed to climate change, which is predicted to cause extreme weather effects.

Around the world, regions are suffering from over extraction of local aquifers. These include major urban centers with their dense populations. Beijing has only 150m^3 of renewable water per capita, well under the World Bank's 1,000m^3 definition of water scarcity. In addition, over extraction of groundwater can have other undesirable effects, such as sinking the land above (subsidence) due to removal of water volume underneath. In Mexico City, subsidence is so severe that the city sinks 3 meters annually.[11] Urban centers are not the only areas suffering from water scarcity, as many rural regions are now parched. In the US, large parts of the south west

are undergoing years-long drought. In many tropical islands, groundwater is non-existent, and the only source of freshwater is unreliable rainfalls.

1.4. Conventional Desalination Technologies

There has been a long history of conventional desalination technologies which extract freshwater from a contaminated water source, or feed water, leaving behind a concentrated waste product, also known as the reject water. These technologies can be categorized as either membrane-based or thermal distillation based approaches. For membrane approaches, the dissolved ions are isolated by the membrane, and water molecules are forced through the membrane. Reverse osmosis (RO) [12,13] is the most common approach, and relies on applying a positive hydrostatic pressure to force feed water through a semi-permeable membrane. The pressure gradient must be higher than the osmotic pressure of the feed water, such that freshwater (permeate) is forced through the membrane. In RO membranes, the flow of water is typically due to solution-diffusion theory.[14] The freshwater flowing through the membrane, or permeate, is highly pure, with typical total dissolved solids (TDS) levels of around 100-500ppm.[15]

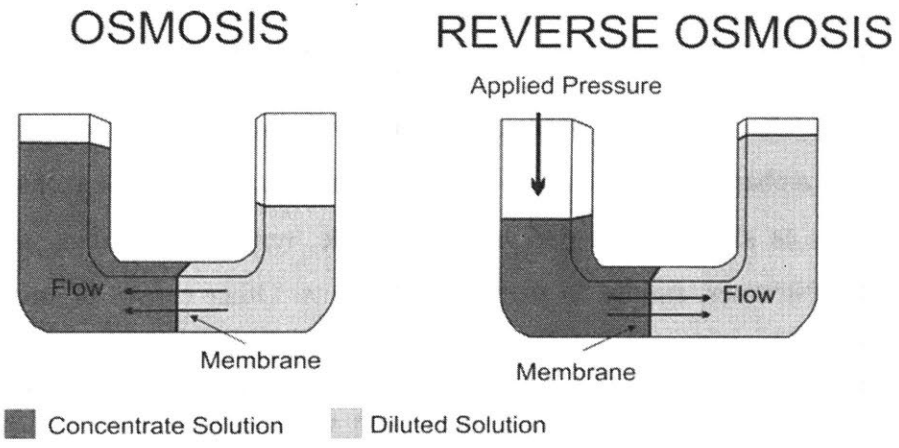

Figure 1.1: Schematic of osmosis and reverse osmosis principle.[16] In osmosis (left), a semi-permeable membrane separates a concentrated solution (dark) from a dilute one (light). Water flows from dilute to concentrate, and the resulting liquid difference is the osmosis pressure. In reverse osmosis, pressure is externally applied to force water to flow through a semi-permeable membrane from concentrated to dilute solution.

Proper design of the membrane is critical to good performance of reverse osmosis units. Membranes exclude dissolved solids and ions from passing through using size rejection, charge rejection, and physical-chemical interactions. RO membranes are prone to surface fouling, which can block feed water flow as well as permeate flow through the membrane. Along with feed water contamination levels, fouling is correlated with membrane roughness and membrane hydrophilicity.[17] Smoother membranes reduce the surface energy reduction when salts adhere to membrane surface, while increased membrane hydrophilicity is shown to reduce bacteria adhesion. Nanostructured surfaces have also been shown to reduce bacteria adhesion, but may increase salt adhesion.[18]

Pretreatment of the feed water is another method to prevent membrane fouling.[19] Pretreatments can include the addition of acids, coagulants, particle filtration, and biological disinfectants. Acids increase the solubility of salts prone to scaling, especially those already at concentration near saturation such as calcium carbonate. Coagulants prepare the feed water for particle filtration. Particles can then be filtered out using filtration beds made of sand, pumice, gravel, and other porous materials. Disinfectants are needed to prevent bacterial growth on membranes, which can cause clogging.[20,21] Bacteria adhere to membranes and secrete a matrix of disaccharides which forms a gel, which increases the diffusion resistance for water to reach the membrane pores. Oxidants are commonly used to disinfect, though they must be chemically compatible with the membrane. Most common RO membranes are degraded by chlorine, so other oxidants such as chloramine and ozone are used. Disinfectants also produce chemical byproducts, so care must be taken to minimize their use.

Electrodialysis (ED)[22] is another type of membrane-based technology, which uses an electric field and ion-selective membranes to separate out ionic contaminants. In ED, a feed water stream is sandwiched by cation and anion ion-selective membranes. Positive and negative dissolved ions in the feed water migrate through their respective membranes, in response to the applied electric field. As a result, the feed water purifies as water flows along the membranes. These membranes can then be stacked, such that alternative layers of concentrated and dilute water flows form. As with RO, membrane fouling is a major concern and pretreatment of feed water is necessary. One ED-specific anti-fouling method is to reverse the polarity of the electric field, such that ions are forced through the membrane in opposite directions. This flushes out solid deposits, and minimizes accumulation. ED energy consumption depends on the feed water salt concentration,

and thus ED is generally used only for brackish water desalination (TDS < 0.5wt%). Compared to RO, ED is more expensive due to electrode cost and membrane cost, and shortened membrane lifetime from electric field exposure.[23]

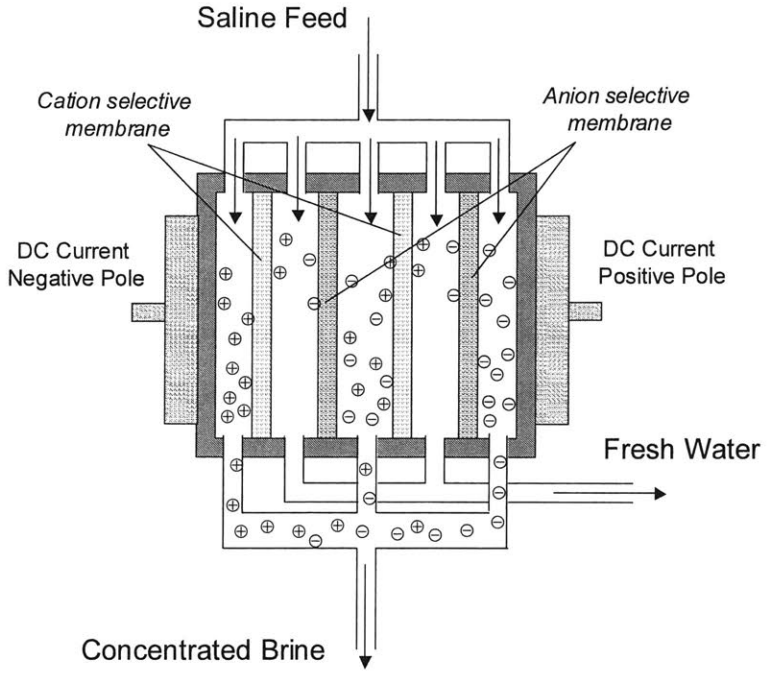

Figure 1.2: Schematic of electrodialysis (ED).[23] Ions from a feed water are separated out using ion-selective membranes, resulting in purified water.

Membrane Distillation (MD) is a [24-27] newer type of desalination technology, which uses hydrophobic membranes and thermal energy to distill water. In MD, heated feed water is flowed along a porous hydrophobic membrane. Because of the hydrophobicity, liquid water does not infiltrate the membrane, but water vapor to pass through. At the opposite side of the membrane, water vapor is condensed on a cold surface separated by an air gap (air gap membrane distillation),[26,28] or a flowing cold water (direct contact membrane distillation),[29] or other methods including sweeping air gap MD and vacuum MD. MD membranes have larger pores (~10μm) than in RO, and are less susceptible to fouling, and MD can also utilize waste heat (~80°C being common operating temperatures). MD also does not require specialized piping for high pressure that RO requires. However, MD is less energy efficient compared to RO. As a thermal process, MD can benefit from multi-staging, which reuses the rejected heat from one condensing stage to heat the feed water of a following stage. [30,31] Although there have been

commercial demonstrations of multistage membrane distillation, the performance has remained relatively low, with gained-output-ratios (GORs) below 4.[32] GOR is defined as the latent heat of the produced freshwater divided by the energy input required. The work developed in this thesis could in the future be coupled with the multi-stage MD concept, and we are currently working on these efforts.

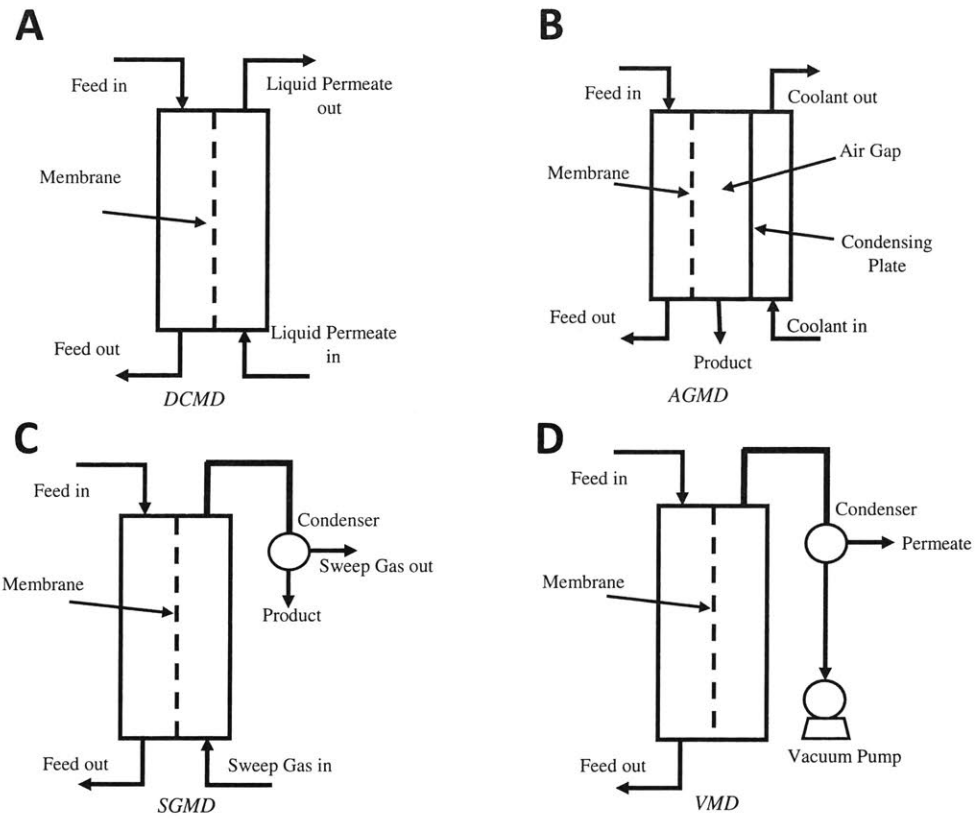

Figure 1.3: Four main types of membrane distillation. [29] The differences arise from how water vapor is condensed. The feed water is always heated so that vapor diffuses through the hydrophobic membrane to the condenser side. The condensed vapor becomes drinkable water.

For thermal distillation approaches, multi-stage flash (MSF)[33,34] and multi-effect distillation (MED) are time-tested approaches, widely utilized when deslination was initially commercialized. These technologies generally apply heat to vaporize the feed water. As the specific latent heat of water is large (2.2-2.5 MJ/kg), efforts to improve efficiency revolve around recycling the latent heat lost during condensation of vapors. This is achieved by rejecting

the latent heat to a series of lower pressure feed waters, such that the boiling temperature of the subsequent feed water section is lower than the condensation temperature of the previous feed water section. Thermal distillation approaches are relatively insensitive to the makeup of the feed water, since heat of vaporization has a small dependence on water concentration. In contrast, RO and ED have energy expenditures highly dependent on feed water purity. MSF and MED are attractive due to high reliability, simplicity of construction, and the maturity of the technology.

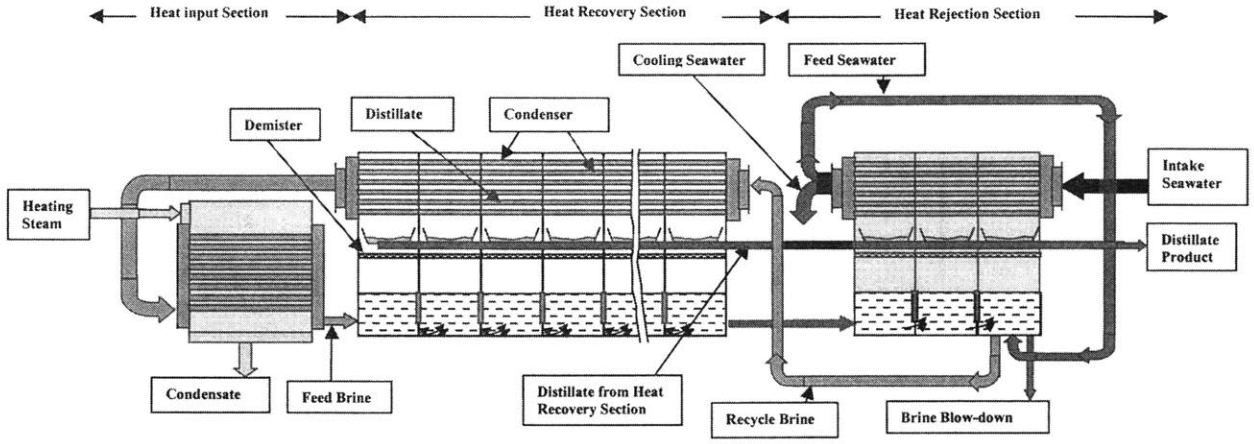

Figure 1.4: Schematic for multi-stage flash distillation (MSF).[35]

In MSF, warm feed water is circulated through successive stages of lower pressure. As it enters each stage, a small amount of vapor is "flashed" so that the feed water saturation temperature and pressure are matched with the stage pressure. The feed water temperature lowers through each successive stage. The produced vapor is condensed, with the excess latent heat recycled to reheat cooled feed water after it has flashed through each stage. Multiple stages are used instead of a single stage, so that the reheated feed water can reach a higher temperature before restarting the flash cycle. Otherwise the reheated feed water would have an intermediate temperature between the hot feed water and cooled feed water. The main difference between MSF and MED is that in MSF, the recaptured latent heat is used to heat a single stream of incoming feed water at the same pressure, whereas in MED the recaptured latent heat is used to heat different stages of feed water, each at successively less pressure.

A major technical concern with desalination technologies is the management of fouling, which is the accumulation of solid matter on equipment. Fouling can be both chemical and biological in

nature. As the feed water is concentrated into reject water, the dissolved solids are concentrated towards their saturation limits, and can come out of solution and nucleate on available surfaces. Although NaCl is far from saturated in seawater (saturation at 26 wt%), many contaminants such as $CaCO_3$ and sulfates are near saturation. An additional concern is the temperature behavior of saturation limits of certain dissolved ions. Alkaline salts typically have a negative correlation of temperature and solubility, which is of particular concern due to the higher temperatures required for thermal distillation approaches.[36] Non-dissolved solids such as silica can also accumulate and clog equipment. Biological fouling occurs through the growth of bacteria into large mats consisting of extracellular disaccharides.[20,21,37] Growth can be inhibited by the use of biocides and disinfectants, although improper dosing with low concentration biocides may encourage bacteria to secrete extra extracellular disaccharides as a defense mechanism. [21]Fouling of any sort is typically undesirable, hindering equipment performance and requiring maintenance or replacement.

The adoption of desalination technologies are now limited by the cost of water, which is approaching production costs below $0.50 per cubic meter at state-of-the-art facilities (Figure 1.5).[38] Cost is dominated by the energy required to separate out the water molecules, with thermal approaches requiring roughly twice the cost in energy, compared to reverse osmosis. In one analysis of seawater desalination,[33] MSF and MED are estimated to require $0.26/m^3 of water produced in thermal and electrical energy. In RO, the energy cost is strictly electrical, costing about $0.15/m^3. The remaining cost of desalination is largely in the capital expenditures of the desalination plant. Operations and maintenance comprise of roughly 5% of the final cost of water. Borsani *et al* have a detailed breakdown of the various expenditures in MSF, MED, and RO plants.[33] Thermal distillation approaches are generally more expensive than RO, and are mechanically complex due to the high number of pressurized stages required for competitive efficiencies. However, for membrane based approaches, such as RO, the energy consumption is highly dependent on the salinity of the feedwater. For both thermal and membrane based approaches, cost decreases with increasing scale. Large scale plants, such as the recently constructed Carlsbad plant in the San Diego region operate on the scale of 100,000 to 1,000,000 cubic meters per day. Most desalination plants require skilled labor for operation maintenance, access to replacement parts and membranes, as well as access to reliable and quality energy sources.

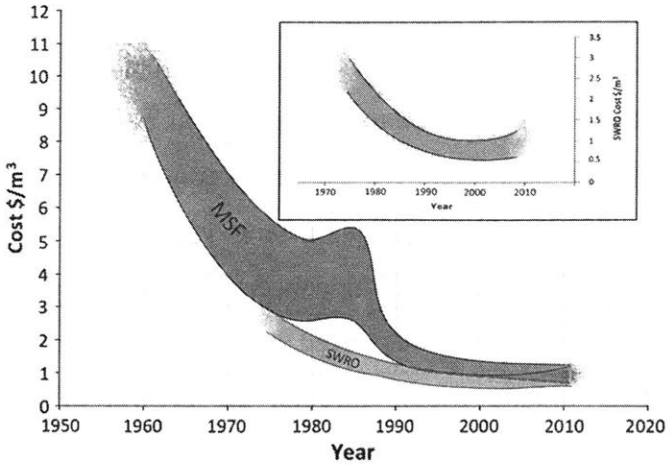

Figure 1.5: Cost of desalination per cubic meter of water produced over time.[39]

Currently, there is high interest in powering desalination with renewable energy sources. Global desalinated water accounts for only 0.6% of global water supply, yet consumes 0.4% of global electricity supply.[5] Society needs to increase desalination 20x in order to cover current unsustainable groundwater extraction. However, increasing global fossil fuel consumption 8% to supply the needed energy is unfeasible, so new sources of cheap and sustainable energy is needed to expand adoption of desalination technology.

1.5. Evaporation Pond Water Management

Evaporation ponds are used to hold waste waters deemed economically untreatable. Waste water, sometimes called produced water, is produced as a byproduct by industries such as oil & gas, mining, textiles and dyes, agricultural, salt production, and more. The desalination industry itself produces waste water in the form of concentrated brine leftover from fresh water extraction.[40] In the oil & gas industry alone, 250 million barrels of waste water is produced *per day*, globally.[41] The waste water is often contaminated with hazardous substances such as organic hydrocarbons, heavy metals and naturally occurring radioactive material (NORM), or minerals such as NaCl, and can have higher concentrations of total dissolved solids than seawater. In some cases, the TDS level can be as high as 200,000 ppm, or 20 wt%.[42] The high concentrations and wide range of contaminants make managing the waste water a challenge, and current solutions are

inadequate. For membrane-based technologies, fouling becomes a greater challenge with the higher TDS levels. Furthermore, waste water is often produced at small-scale, in distributed locations. For example, each hydraulic fracturing well may produce 2000m^3 of contaminated water over several years.[43] This makes centralized, large-scale desalination plants economically unfeasible. One common solution to managing waste water is injecting it down deep mine shafts. However, this practice has caused local earthquakes, even in region without a recorded history of earthquakes.[44] In addition, many locations are not near adequate mines, which can increase the cost of transporting produced water from \$0.50 to \$80 per barrel (\$5-800 per m^3).[45]

Often the default waste water management strategy becomes construction of on-site evaporation ponds.[40,46] The operational concept is simple: expose the waste water to ambient air, and use the incident solar energy and winds to evaporate the freshwater component. Evaporation ponds are especially useful in warm and dry climates with access to abundant sunlight. Evaporation rates in the ponds are a function of several parameters, such as ambient temperature, ambient vapor pressure, local wind speed, and available sunlight. Typical evaporation rates vary depending on geography, but can vary from 30-50 inches per year, in areas from Pennsylvania, USA to Utah, USA respectively.[47] The advantages of evaporation ponds include simple construction and the ability to reduce and concentrate liquids until solid.

1.6. An Underserved Market: Small-scale Desalination

Although desalination technology has seen significant adoption, an underserved market still exists in the area of small-scale desalination, especially in regions where access to energy is limited or expensive. RO, while costing \$0.50 per cubic meter at large scale (100,000m^3/day capacity), can be 4x as expensive when scaled down to a still significant 1,000m^3/day. Figure 1.6 shows RO plant capital investment per m^3/day increasing sharply for smaller capacity desalination plants. Thermal distillation facilities such as MSF and MED are cost effective compared to RO only above capacities of 3,000 m^3/day.[48] This capacity serves the daily drinking needs of 750,000 people, at a WHO recommended 4L per day per person.[49] In addition, it may be difficult to obtain financing for large capacity systems; the Carlsbad plant cost 1 billion USD, an unreasonable price for small populations. Scant data is available for commercial systems on

the order of 1-10m^3/day, alluding to the high cost and unattractive prospects. Such low capacity systems can be adequate for low income villages of several hundred individuals.

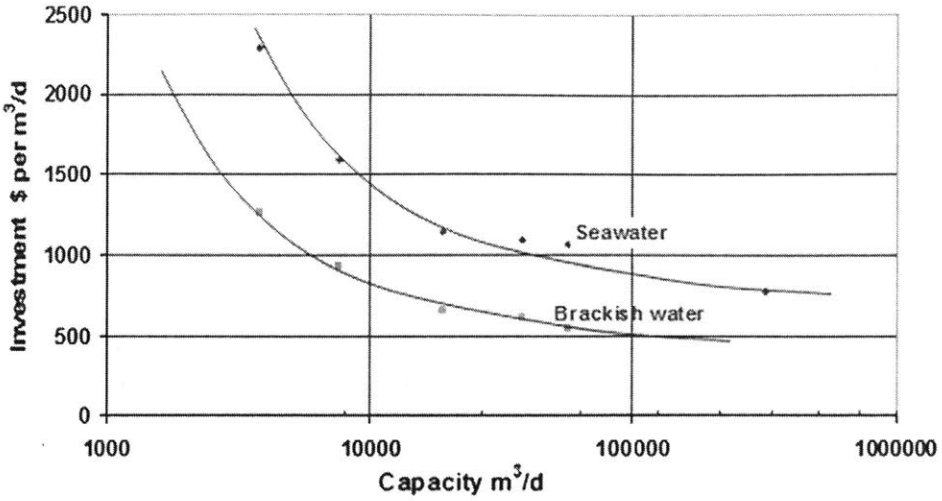

Figure 1.6: Investment cost vs capacity (m^3 per day) goes up sharply as capacity decreases.[39]

One time-tested method for small-scale desalination is the solar still. The solar still is a simple solar collector that heats water in a basin, and condenses the evaporating vapors. Because water is condensed from vapor, the purity of the distillate can be very high. In one study, the distilled water had electrical conductivities below 10^{-3} Sm^{-1}, corresponding to a very low TDS of ~6ppm.[50] However, volatile contaminants such as organic solvents would be expected to stay in solution, as they tend to vaporize along with water. Solar stills offer high scalability, ease of maintenance and do not require solar concentration (e.g. focusing mirrors or lenses), in contrast with other solar-powered technologies. However, the main challenge facing solar stills is their low efficiency: on an annual basis, at most 30-40% of the incident energy can be used to evaporate water. Several key shortcomings of the conventional single-basin solar still are the need to heat an entire volume of water, the need to regularly clean out the accumulated contaminants, and the generous land area needed to collect adequate sunlight. A rich portfolio of research has been conducted to attempt to improve the unit cost of water from solar stills. These research include attempts at heat localization through using porous sponge cubes,[51] floating absorbers,[52,53] isolated evaporation wicks,[54-57] and more. Other attempts include enhancing condensation of the produced vapor through liquid cooling,[58] separate condensation compartments,[59] fans to enhance internal circulation.[60] Research has also been conducted on

improving optical transmission via optimal angling of the glass condensation cover,[61] as well as introducing double-sloped solar stills.[62] Multiple-effect solar stills have been implemented to improve thermal efficiency, by reusing the condensed latent heat to drive evaporation-condensation in a subsequent solars stills.[63] There was a slight decrease in cost (~15%) in going from single to double effect.[63] Due to the low overall efficiency combined with high installation costs ($38 to 300 per m^2), solar stills produce water at high cost (~$15 per m^3 water).[64]

An ideal small-scale desalination system should have both low production costs, in dollar per m^3 water produced, as well as low capital costs to ensure easy financing and minimal financial risk for the investors.

1.7. Thesis Outline

This thesis will contain three topical chapters. The first two chapters detail efforts to create high efficiency solar evaporation structures for vapor and steam formation, which can be used for a variety of applications, from desalination to others such as sterilization and wastewater management. The last topical chapter deals with structures to collect and condense the generated vapors into drinkable pure water.

In chapter 2, nanofluid-based solar vapor generation will be discussed. A labscale solar vapor generator was built using various carbon-based nanoparticles as a solar absorber. This solar vapor generator operated under 10x solar concentration, the maximum concentration achievable without tracking the sun. Solar-to-vapor efficiencies as high as 70% are measured, and various models are created to understand the underlying heat transfer mechanisms of nanofluids under solar illumination. In chapter 3, a solar steam generator was created that operates under ambient sunlight, without any optical concentrators. This device was created out of a >$5/m2 of common materials, and could generate both 100°C or 71% efficient vapor generation. Finally, chapter 4 discusses the construction of a low cost condensation system to pair with the aforementioned solar vapor generators. Information collected from a market research trip is presented, as is experimental and analytical evaluation of the condensation system. A new evaporation structure designed for long-term evaporation of seawater is displayed. The combination of these chapters ultimately aims to demonstrate a cheap, portable, and personal solar desalination technology.

Chapter 2

2. Nanofluid-Based Solar Vapor Generation

Traditional solar-thermal receivers consist of surface absorbers that convert the majority of the incoming solar radiation into heat while minimizing thermal re-radiation loss. [65-76] This heat can then be used to generate steam or vapor. Although these receivers have high photothermal conversion efficiencies, surface absorbers are ill-suited for heating carrier fluids because the heat generation is separated from the fluid to be heated. At high solar concentrations (>50 suns), such as those used in industrial-scale solar thermal power plants,[77-85] a large temperature difference forms between the absorber and the fluid, leading to high surface temperatures and high radiative losses. One approach to minimizing the absorber-to-fluid temperature difference is to use volumetric absorption within the carrier fluid itself, which has been predicted to lead to a 5-10% increase in photothermal efficiency.[81,86,87] Volumetric absorbers such as porous media,[88-93] gas-particle suspensions,[86,94-98] molten salts,[65,70] and nanoparticles suspended in fluids (nanofluids)[77,79-85,99,100] have been used to minimize surface temperatures of receivers, thereby reducing the receiver heat losses. Volumetric absorbers can have surface temperatures lower than even the bulk fluid temperature,[81,100,101] otherwise known as thermal trapping.[88,90,102]

One approach to volumetric solar absorption is to use dispersed nanoparticles in a working fluid, and the pairing is termed a *nanofluid.* In nanofluids, the nanoparticles act to scatter and absorb the incident solar energy, and effectively "directly" heating the working fluid. For the solar desalination market, nanofluids are attractive because of the potential for ease of transportation and on-site preparation. Recently, nanofluids have been studied for direct steam generation using solar energy.[86,94,96,98,101,103] In addition, nanofluids have been shown to enhance critical heat flux in certain boiling applications.[104,105] Neumann *et al.* demonstrated the use of nanofluids for direct water vapor generation,[70,106] reaching device efficiencies of 24% at solar concentrations of 1000 suns (1 sun = 1 kWm^{-2}). Although a novel approach, the exact mechanism of vapor generation has been debated over the past few years.[70,99,100]

2.1. Two Proposed Mechanisms for Nanofluid Solar Vapor Generation

Two potential mechanisms have been proposed to explain the vapor generation mechanism for nanofluids under solar illumination.[100,101,107] In one mechanism, nanoparticles isolate the heat generation to very near the particle-liquid interface in a non-equilibrium manner such that the surrounding bulk fluid remains cold while the particle heats up to a temperature which nucleates a vapor bubble locally. Several researchers have studied nanoscale-to-microscale bubble formation surrounding individual and arrayed nanoparticles. Lukianova *et al.* conducted pulse-laser illumination of gold nanoparticles to show that a critical laser fluence equivalent to $3x10^8$ suns was required before bubble formation initiated.[84,102,107-109] Fang *et al*, performed continuous laser illumination experiments of gold nanoparticles on a substrate and observed a similarly high nanobubble formation intensity threshold, on the order of $3x10^7$ suns.[101,110] Lombard *et al.* modeled theoretically the kinetics of nanobubble formation around gold nanoparticles,[100,106] showing that an intensity of $\sim 1x10^{10}$ suns was required to nucleate a bubble. Though nanobubble formation has been observed, a combined optical absorption and heat conduction model using achievable illumination intensities does not give the required temperature differential.[70,111,112]

In the second mechanism, nanoparticles rapidly reach equilibrium with the surrounding fluid, and vapor generation is purely due to the rise in temperature of the bulk fluid.[66,100,107,113,114] Several experiments have shown that the interparticle fluid temperatures can reach as high as the spinodal decomposition temperature of water (594 ± 17K) before bubble formation.[84,107-109,115] In addition, Keblinski and Cahill simulated an array of 5000 nanoparticles, and found that two time scales exist in the heating profile of nanofluids.[110,116] They found that heating on the macroseconds scale is due to global heating of the fluid, but on the nanoscale the heating is confined near to the nanoparticle. Finally, a recent work by Hogan *et al* has focused on using high intensity lasers ($\sim 10^6$ W/m^2) to show the effect of light scattering leading to localized absorption on the direct vapor generation from nanofluids. They simulated light propagation through the nanofluid, and compared experimentally with nanoparticles of varying scattering cross sections. In their work, they concluded that Fourier-law heat conduction adequately describes the nanoparticle-based direct steam generation.[66,100]

Based on the previous studies, there exists a need to 1) increase the efficiency of the direct solar vapor generation process to make the technology more competitive with existing solar vapor

generation techniques,[70,111,112] 2) seek solutions that utilize the full spectrum of solar energy at lower optical concentrations (≤10 suns) than previous work to achieve commercial viability and minimize system cost,[66,113,114,117] and 3) gain a better understanding of the physical mechanisms governing solar vapor generation. Through rational design and detailed experiments, we show highly efficient direct vapor generation (69±4% at 80°C). We attain these results using water based nanofluid solar receivers at low optical concentrations (≤10 suns), in comparison to all previous work, which used high intensity lasers or high optical concentration solar flux. A solar concentration of 10 suns is approximately the highest achievable without active sun-tracking, *via* non-imaging optics.[115,118] In some concentrated solar plants (CSP) the optical collection field can comprise up to 30% of the total installed cost.[116,119] In addition, we report that well-dispersed nanofluids can lead to higher vapor generation in transient conditions. Furthermore, through a consistent set of numerical simulation, analytical modeling, and experimental validation, we clarify that the solar vapor generation of nanofluids is in fact due to global heating of the bulk fluid and related classical evaporation phenomena. This chapter advances a direct solar vapor generation platform that promises to be low cost and has potential for a wide-range of solar-based applications such as power generation,[66,120] distillation,[70,96] and sterilization.[117,121]

2.2. Experimental Setup for a Nanofluid Solar Vapor Generator

To study the effect of different nanofluids on the receiver efficiency, we performed solar vapor generation experiments on a custom-built lab-scale receiver. To supply solar energy to the nanofluid samples, a solar simulator was used in conjunction with a Fresnel lens and aperture to generate and focus concentrated solar light (Figure 2.1a). The nanofluid container was constructed out of two concentric acrylic tubes, with a layer of aerogel particles in between to serve as an insulator to minimize radial heat losses (Figure 2.1b). The aerogel particles were sealed from the environment with acrylic discs. The nanofluid was exposed to the ambient to vent the vapor. No insulation was used over the top of the nanofluid, which maximized the evaporation efficiency by allowing faster vapor diffusion. Four E-type thermocouples were inserted into the nanofluid container to measure the fluid temperature at different distances from the nanofluid-air interface. As the nanofluid evaporated, the fluid level dropped below each thermocouple, allowing temperature measurement of the liquid-vapor interface location. The mass loss was measured using a high accuracy weight scale (see Supplementary Section 2.6).

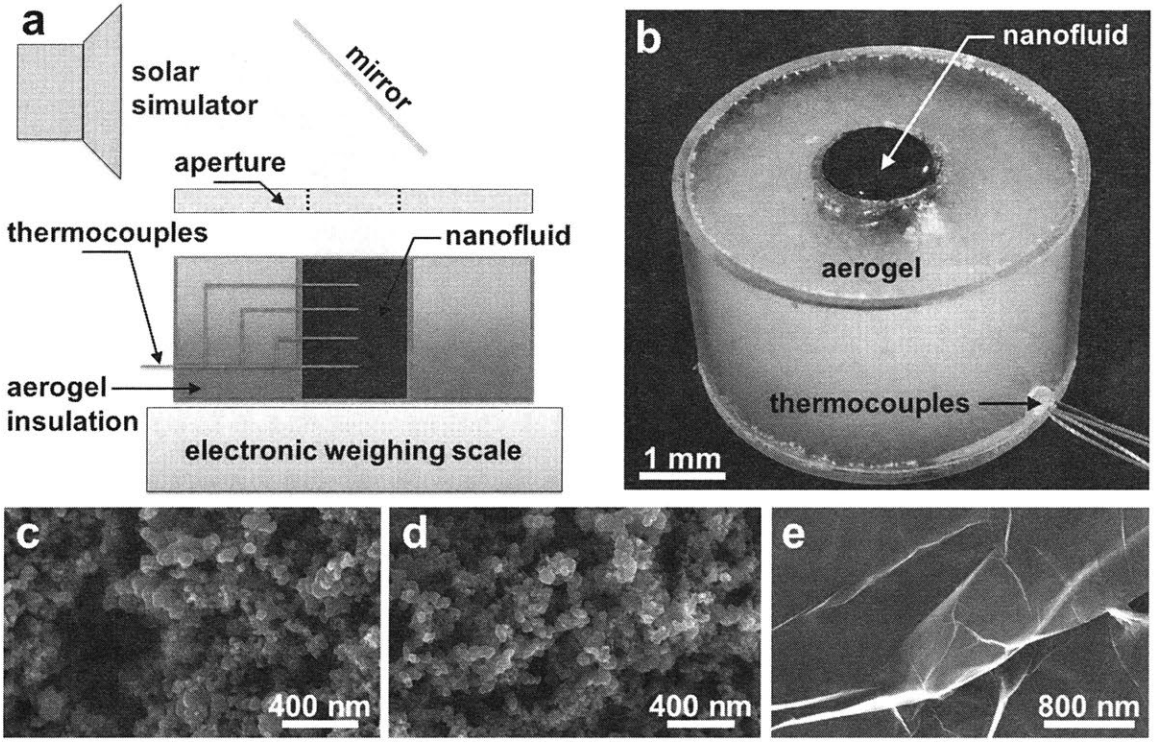

Figure 2.1. (a) Schematic of solar vapor generation device. (b) Image of the nanofluid container showing the aerogel insulation, black nanofluid, and thermocouple feed through. Scanning electron micrographs (SEM) of (c) graphitized carbon black, (d) carbon black, and (e) graphene nanoparticles. To obtain SEM images, the nanofluids were dehydrated prior to imaging.

The nanofluids studied were based on carbon nanoparticles, which are significantly lower cost than metal nanoparticle suspensions, and have better broadband solar absorptance.[122] Three different highly absorbing nanofluids were synthesized for this thesis: graphitized carbon black (GCB, Figure 2.1c), carbon black (CB, Figure 2.1d), and graphene particles suspended in water (Figure 2.1e). The nanofluids were created by sonicating 0.5 wt% of the various nanoparticles in distilled water for 1 hour. We chose the nanoparticle concentration to be 0.5wt % based on previous works in studying the effect of nanoparticle fraction on photothermal properties of nanofluids.[122] The GCB (Sigma-Aldrich, 699632-25G <500nm) and CB (Cabot, Vulcan 9 N110) were commercially purchased. The graphene nanosheets were made using an electrochemically stimulated exfoliation process.[70,118] All three nanofluids appeared stably suspended throughout

the duration of the test. During storage, the GCB nanofluid was stable for months at a time, whereas the graphene nanofluid was stable for over a year. The CB nanofluid was stable for periods less than a week.

To study the non-constant nature of solar irradiance during the day, both steady-state and transient receiver efficiencies were measured.

2.3. Performance of a Nanofluid Solar Vapor Generator

Figure 2.2 shows the experimental mass change of the nanofluid container as a function of time for each of the studied nanofluids at 10 sun illumination. The absolute mass change rate ($|dm/dt|$) started at zero and gradually increased with time due to the photothermal conversion of solar radiation to enthalpy of evaporation. As the nanofluid absorbed more solar radiation, the temperature of the bulk nanofluid solution gradually increased in conjunction with the evaporation rate. After an initial heating period of ≈4000 seconds, the system reached steady-state operating conditions where the evaporative and parasitic heat losses balanced the absorbed solar radiation. The evaporation efficiency at steady-state conditions was determined by dividing the gained enthalpy in the generated vapor by the total incoming solar radiation input,

$$\eta = \frac{\dot{m} h_{fg}}{Q_S A} \tag{2.1}$$

where $\dot{m}$ is the steady-state vapor mass flux, h_{fg} is the latent heat of vaporization for water at 1 atm (2.257 $MJkg^{-1}$), A is the area of the aperture (4.95 cm^2), and Q_S is the total incoming solar flux (10 kWm^{-2}) after concentrating optics, hence the efficiency reported is an internal efficiency. The sensible heat of the evaporating fluid is not accounted for, since the evaporation is a batch process without influx of cold fluid. The steady-state efficiency was determined by using the data where the mass loss is linear to within an R^2-value of 0.999. Although the addition of nanoparticles to water has been reported to change the thermophysical properties such as heat capacity[115,119] and thermal conductivity,[120,123,124] the small concentration of nanoparticles used in

this study (0.5 wt%, 0.23 vol%) was determined to have a negligible effect on both properties.[96,125]

The system evaporates nanofluids similarly to a continuous process. The addition of replenishing fluid would add two details to our analysis: 1) conduction of heat to the underlying and flowing liquid, and 2) use of some of the absorbed solar energy to heat the nanofluid up to operating temperature (sensible heating). The receiver had already reached within 2% of steady-state evaporation, while thermocouples showed the underlying liquid to be near room temperature (<30°C). This shows that conduction into the liquid is not a dominant heat loss mechanism. The sensible heat increase in the generated vapor phase ($\dot{m}c_p\Delta T$) was small (~7%) compared to the latent heat of vaporization ($\dot{m}h_{fg}$), and was purposely excluded to conservatively estimate the efficiency.

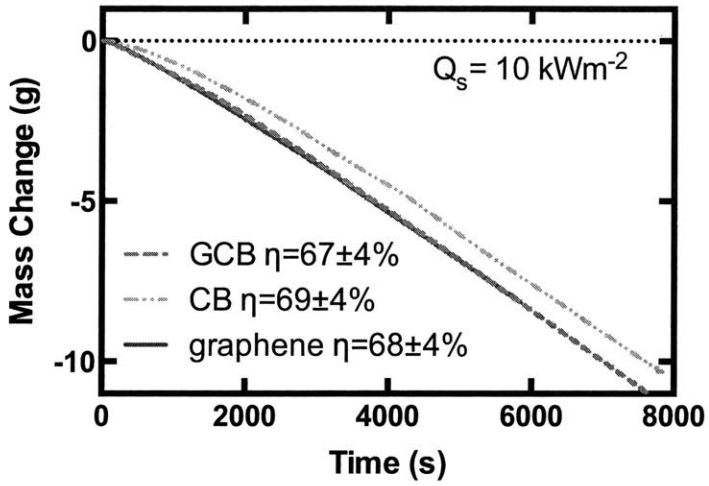

Figure 2.2. Nanofluid receiver mass change as a function of time for the carbon black (CB), graphitized carbon black (GCB), and graphene nanofluids while illuminated by 10 suns of radiation (Q_s = 10 kWm^{-2}). At steady-state (t > 4000s) the mass change rate was approximately equal for all of the nanofluids ($dm/dt = \dot{m} \approx$ -1.5x10^{-3} gs^{-1}).

The steady-state evaporation efficiency was approximately the same for all three nanofluids tested ($\eta \approx 69\%$), with all calculated values being within the measurement uncertainty (±4%). Of the losses from our system, radiation was calculated to be 4%. The measured specular reflectivity of the nanofluids was <1% (see Supplementary section 2.10). The losses into the

container were modeled using a COMSOL simulation and matching the boundary conditions to the embedded thermocouples. The conduction into the bulk underlying nanofluid was ≈9%, and the losses to the surrounding aerogel insulation and ambient were ≈12%. The air convection from the evaporating nanofluid surface accounted for ≈3% of the total losses (see Supplementary section 2.8). Transmission losses were not present for the nanofluids studied here due to all of the incoming radiation being absorbed prior to reaching the bottom of the nanofluid container.

It is important to note that the 69% efficiency includes the incident power on the receiver, but not the losses from the optics. If a Fresnel lens with modest optical efficiency of ≈83% were used to supply concentrated solar light,[121,126] a system vapor generation efficiency of 57% would be achieved. Even with the additional optics loss included, our reported vapor generation efficiency of 57% is higher than achieved in a previous study (≈24%).[70,121] In addition, our nanofluids-based receiver utilized a much lower solar concentration (10x vs. 1000x), one achievable with less stringent tracking requirements and lower cost components.[100,115]

Since the measured steady-state efficiencies for each nanofluid were approximately identical, it can be inferred that the global absorptance of the different nanofluids are similar. Furthermore, the high steady-state vapor conversion efficiency shown here can be attributed to the high absorptivity of the nanofluid in the solar spectrum, and the unrestricted vapor extraction. In addition, the utilization of low thermal conductivity aerogel insulation ($\sim$0.02 $Wm^{-1}K^{-1}$) helped to minimize side loses and allow for a majority of the photothermal energy conversion to be utilized for water phase change. In a larger application-scale nanofluids-based solar receiver, the side losses would be smaller than in the lab-scale device due to a lower surface-to-volume ratio, and even higher efficiencies are potentially achievable.

Transient Performance

To examine the transient performance of the nanofluid receiver, we compared the mass change on a smaller time scale ($0 < t <$ 300s). Each of the nanofluids was first measured under dark conditions for 10 minutes, to ensure that the nanofluid temperature was consistent with the lab ambient temperature. The cover was removed from the aperture, and data acquisition was initiated. Figure 2.3a shows the mass loss as a function of time during the transient period for the three nanofluids. The GCB-based nanofluid evaporated the most water during the transient

period (≈0.3 ± 0.001 g), followed by the graphene (≈0.22 ± 0.001 g) and regular CB nanofluids (≈0.1 ± 0.001 g). The transient performance of the nanofluids was related to how well-dispersed the nanoparticles in the fluids were. The CB nanofluid was noticeably less well-dispersed, and the meniscus was more transparent with particle agglomerates discernible by eye. Nanofluids with well-dispersed particles generated heat closer to the liquid-vapor interface, and had a higher interfacial temperature and overall evaporation rate. The nanofluid dispersity is shown later to be related to the extinction coefficient of the nanofluid. The reason for the variable nanofluid dispersions is due to the different zeta potentials of the nanoparticles in the water solution, which is related to nanofluid stability. Nanofluids with high magnitude of zeta potential (negative or positive) are electrostatically stabilized, while nanofluids with low magnitude zeta potentials tend to agglomerate.[123,124,127] CB nanofluids have been reported to have a zeta potential of only ≈-10 mV,[125,127,128] resulting in agglomeration and lack of stability, while the graphene and GCB nanofluids reportedly have lower zeta potentials (higher magnitude, ≈ -40mV),[100,126] resulting in better nanofluid stability, less agglomeration, and enhanced transient performance.

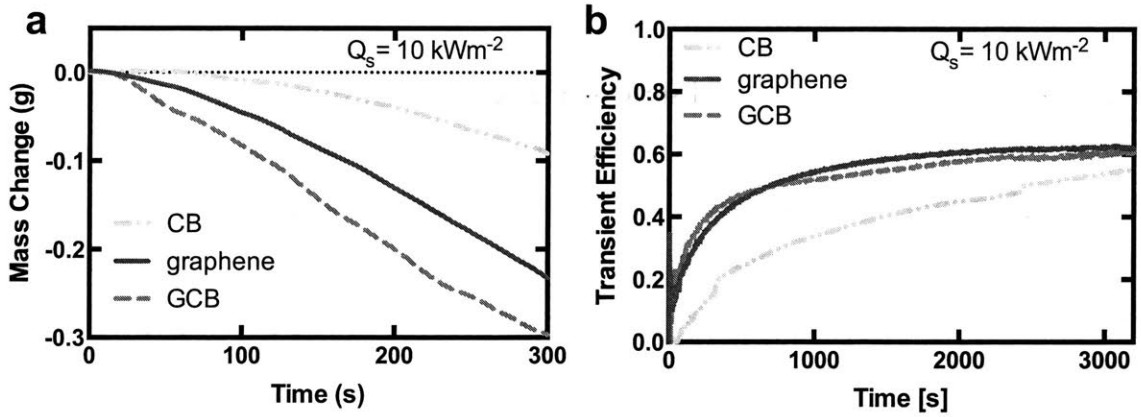

Figure 2.3. (a) Mass change in transient conditions and (b) transient efficiency as a function of time for the CB, GCB, and graphene nanofluids while illuminated by 10 suns of solar radiation (Q_s = 10 kWm^{-2}). The GCB-based nanofluid had the highest transient evaporation efficiency, followed by the graphene and regular CB nanofluids.

To quantify the transient performance in terms of vapor generation efficiency, we define a transient efficiency, η_T, as the total amount of water evaporated since illumination began divided by the total solar energy incident on the nanofluid receiver during that time interval,

$$\eta = \frac{\int_0^t \dot{m}\left(h_{fg} + c_{p,l}\Delta T\right)dt}{\int_0^t Q_s A\, dt} \tag{2.2}$$

where $c_{p,l}$ is the specific heat of liquid water (4.19 $kJkg^{-1}K^{-1}$), and ΔT is the temperature rise of the liquid prior to evaporation. The transient efficiency depends on the temporal length of the measurement, but is appropriate when considering varying solar power over the course of the day. Despite the GCB nanofluid reaching steady-state faster (Figure 2.3a), the graphene nanofluid reaches a similar transient efficiency (69±4% for $0 < t <$ 6000s). The transient efficiencies of GCB and graphene nanofluids are 7% higher than that of CB nanofluid. At shorter measurement times, this transient efficiency discrepancy increases as shown in Figure 2.3b. The measured transient receiver efficiency of 69±4% can again be coupled with a modest Fresnel lens optical efficiency of 83%,[121,129] giving a system transient vapor generation efficiency of 57%.

Steady-state vs. Transient Performance

It is important to note that the identical steady-state performance does not indicate that all three nanofluids will achieve the same performance in a given solar application. The transient performance becomes crucial when choosing nanofluids for applications that may have intermittent interruptions in illumination such as rolling cloud cover. Another situation where transient performance becomes important is cases where solar tracking is not used, such as in residential homes. In these cases, the solar illumination angle is constantly changing, and therefore the incoming radiation is changing throughout the course of the day. In the case of transient incoming solar radiation, the GCB nanofluid would perform the best due to its ability to reach steady state the fastest and generate the most vapor in the transient period of operation.

2.4. Heat Transfer Modeling of Nanofluids Solar Vapor Generator

To explain the transient absorption mechanism, we developed an analytical heat transfer model to show that the transient efficiency is dependent on the extinction coefficient of the nanofluid, which is determined by the absorption and scattering characteristics of nanoparticles and their

agglomerate size (r_o). A previous study of nanofluids based on metal nanoparticles has shown a positive correlation between the nanoparticle extinction coefficient and nanofluid evaporation rates.[100,129] Since all the nanoparticles are carbon based, we mainly consider the effect of the agglomerate sizes, which were experimentally measured using optical characterization methods, and the dependence of calculated evaporation flux on the extinction coefficient was determined using the developed analytical model.

The nanoparticle agglomerate sizes were determined using dynamic light scattering (DLS) and optical microscopy, depending on the agglomerate size. The GCB nanoparticles were well dispersed, and had smaller agglomerates (r_o~110 nm) suitable for DLS measurement. The CB nanoparticles are less well dispersed, and their agglomerates were larger (r_o ~5 μm) and observable with optical microscopy (see Supplementary Section 2.11). The agglomerate sizes determined the particle density in the nanofluids, since the volume fractions were the same.

Once the nanoparticle agglomerate sizes were determined, an extinction coefficient was calculated for GCB and CB nanofluids, using Mie theory in the independent scattering regime,[127,130] and indices of refraction from literature (see Supplementary section 2.12).[127,128,131] The calculated scattering and absorption cross sections of nanoparticle agglomerates were of similar magnitudes. To approximate the heat generation, the total extinction coefficient calculated was used in the heat generation term for Eq.(2.3) in our transient efficiency model shown later. In the event that forward scattering dominates back scattering, as is the case with the studied nanoparticle agglomerates, our calculations will under predict the difference in transient efficiency. Figure 2.4. shows the calculated efficiency factors $Q_{ext}, Q_{abs}, Q_{sca}$ for extinction, absorption, and scattering. Using the efficiency factors, the extinction coefficients for GCB and CB were calculated and found to differ more than two orders of magnitude. The estimated extinction coefficients for GCB and CB nanofluids were 5.6×10^5 m^{-1} and 1.6×10^3 m^{-1} respectively. Again, the difference in extinction coefficients is largely due to the particle (agglomerate) number density, which given a same amount of material is related to the stability of the suspension.

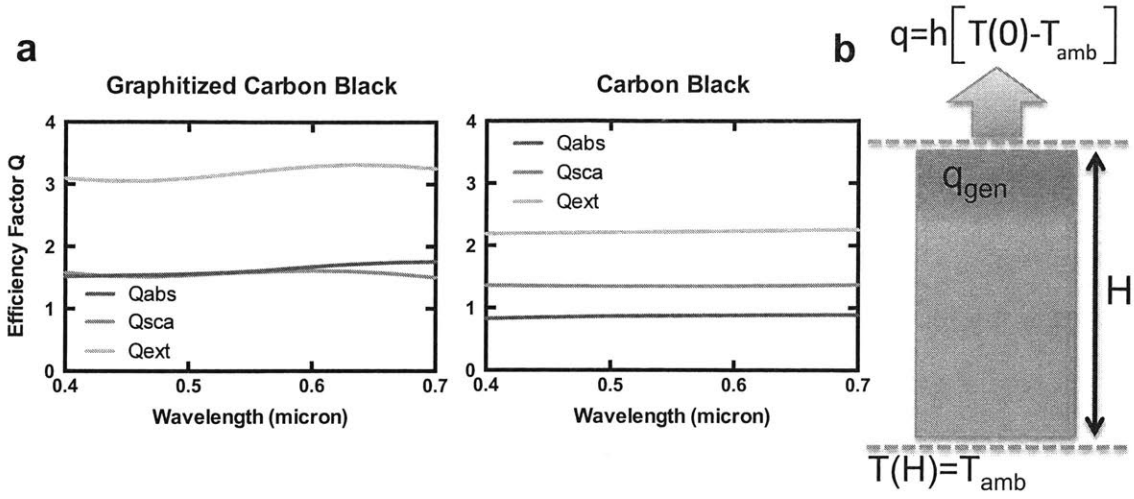

Figure 2.4: (a) Efficiency factors for the nanoparticles calculated using Mie theory. $Q_{ext}, Q_{abs}, Q_{sca}$ are the efficiency factors for extinction, absorption, and scattering. The carbon black has a smaller extinction efficiency than the graphitized carbon black. (b) A visual schematic of the transient efficiency model.

Using the estimated extinction coefficients of the nanofluids, we constructed an analytical heat transfer model of the nanofluid receiver to determine the effect of extinction coefficient on the transient performance. Our model neglects convection and considers transient conduction effects coupled with absorption. Only conduction is considered because the heat generation occurs at the top end of the receiver, thereby minimizing natural convection inside. The weaker extinction coefficient shifts the heat generation deeper into the nanofluid receiver, and reduces the temperature of the nanofluid-air interface. This ultimately reduces the evaporation efficiency of the device. A schematic of the transient efficiency heat transfer model can be seen in Figure 2.4c. The analytical model is shown in Eq.(2.3), where λ is an exponential constant for heat generation, and q_0 is the incident light intensity.

$$\frac{\partial \Theta(x,t)}{\partial t} = \alpha_x \frac{\partial^2 \Theta(x,t)}{\partial x^2} + \frac{q_0 \lambda e^{-\lambda x}}{\rho c_p} \tag{2.3}$$

Boundary Condition #1: $\Theta(H,t) = 0$

$$\text{Boundary Condition \#2: } -k_x \frac{\partial \Theta(0,t)}{\partial x} + h\Theta(0,t) = 0$$

$$\text{Initial Condition: } \Theta(x,0) = 0$$

The boundary and initial conditions for the heat transfer model are: 1) convectively cooled temperature bath on one end (the evaporation side, $x = 0$), with h ($150 \frac{W}{m^2 K}$) fitted from the COMSOL simulation of the nanofluids receiver, and 2) constant ambient temperature at the other side ($x = H$), and 3) initially, the nanofluid receiver is at ambient temperature. The model is solved using the Green's function method. The results of the simulation are shown below in Figure 2.5.

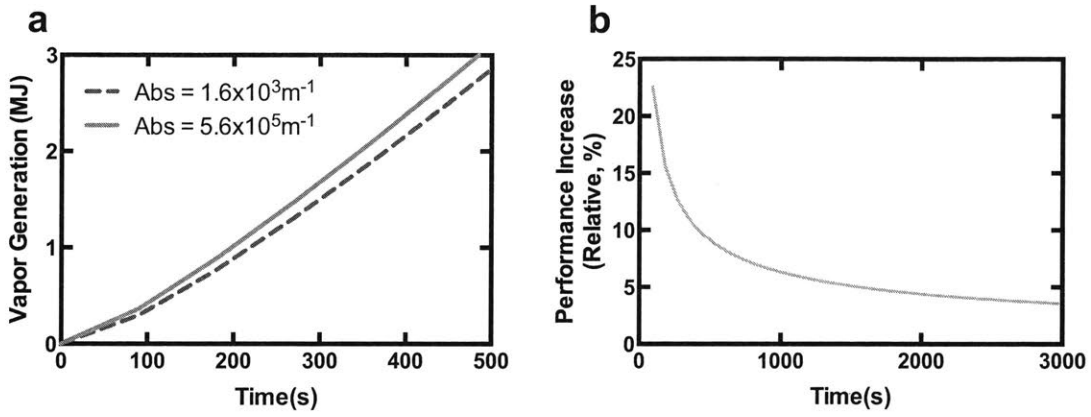

Figure 2.5. (a) The calculated energy loss through evaporation plotted as a function of time, for nanofluids with different extinction coefficients. The higher extinction coefficient leads to higher evaporation flux due to heat localization at the nanofluid-air interface and higher surface temperature. (b) The relative vapor generation increase in total evaporated energy between the nanofluids considered in (a).

Figure 2.5a shows the calculated total water vapor generated from the nanofluid as a function of time for the GCB and CB nanofluids. It can be seen that the nanofluid with the larger extinction coefficient (GCB) has the higher vapor generation rate. To help quantify the performance difference between the two nanofluids, Figure 2.5b shows the relative vapor generation increase between the two nanofluids, which is defined below.

$$\eta_{relative} = \frac{h\Theta_{GCB}(0,t)}{h\Theta_{CB}(0,t)} \tag{2.4}$$

where η_{relative} is the relative performance increase of the GCB nanofluid over the CB nanofluid. The performance increase is particularly significant shortly after illumination, and decreases over time. At 3000 seconds, the total vapor generated for the two nanofluids differs by about 4%. This is smaller than the experimentally measured relative difference of 10% in the transient receiver efficiency (Figure 2.3). We attribute this discrepancy to the use of a constant heat transfer coefficient in the model, whereas in reality the evaporation rate will increase non-linearly with temperature. This is due to the non-linear dependence of vapor pressure, the driving force for evaporation, on temperature. Nonetheless, the experimental and model results show good agreement. This analytical model shows how heat localization due to a larger effective extinction coefficient in the nanofluid can increase the transient evaporation, corroborating recent work on metal particles[100,132] , but does not clarify the mechanism for vapor generation.

2.5. Solar Vapor Generation Mechanism for Nanofluids

Two heat transfer models were created to understand the evaporation mechanisms in nanofluids: 1) a horizontally illuminated lumped capacitance model, and 2) an individual particle heating model.

Horizontal Illumination: Lumped Capacitance Model

To provide insight into the experimental results, and support the mechanism of global fluid heating for vapor generation in these nanofluids, we conducted additional experiments and developed the corresponding model (see Supplementary Section 2.7). We show from the experiments and model that the evaporation heat transfer coefficients developed to model the evaporation of pure water can also be used to describe the evaporation behavior of nanofluids. We illuminated the nanofluids from the side to achieve uniform temperatures throughout the nanofluid. This allows us to utilize the lumped capacitance approximation in the model. The following assumptions were made: 1) the fluid is isothermal throughout the cuvette ($Bi =$

$\bar{h}L/k_w \approx 0.1$, where Bi, $\bar{h}$, L, and k_w are the Biot number, external heat transfer coefficient to air ($\bar{h} \approx 5$ $Wm^{-2}K^{-1}$), thickness length scale of the cuvette ($L \sim 10$ mm), and nanofluid thermal conductivity ($k_w \approx 0.6$ $Wm^{-1}K^{-1}$), respectively. 2) The boundary condition at bottom of the cuvette was considered insulated. 3) The side walls are modeled as heated vertical plates undergoing natural convection to the surrounding ambient air,[129,133,134] and radiative losses. 4) The top evaporating surface undergoes both natural convection and evaporation.[129] 5) All incident solar radiation is absorbed by the nanofluid ($\varepsilon \approx 1$). The high solar absorption was validated by measuring the transmission of solar light through a nanofluid filled cuvette using a UV-VIS spectrophotometer (see Supplementary Section 2.10).

It is important to note that although our transient efficiency model showed that the fluid temperature is in fact non-uniform and dependent on the extinction coefficient, the assumption of lumped capacitance in this model is still valid, due to the different illumination conditions. Furthermore, this model is not meant to further elucidate or resolve the transient performance discrepancy from sample to sample, but rather to give a physical picture of the vapor generation process in terms of a global energy balance and validate the classical heat loss mechanisms present in the experiment.

Accounting for all of the heat transfer pathways, the differential equation for the bulk nanofluid temperature, T is (for full derivation, please see Supplementary Section 2.7)

$$\rho_w c_p V \frac{dT}{dt} + \rho_w c_p T \frac{dV}{dt} = q - \left(\overline{h_s} A_s + \overline{h_t} A_t\right)(T - T_\infty) - \varepsilon\sigma A_T\left(T^4 - T_\infty{}^4\right) - \overline{h_e} A_t\left(P(T) - \varphi P(T_\infty)\right), \tag{2.5}$$

where ρ_w is the nanofluid density ($\approx$1000 kgm^{-3}), V is the nanofluid volume, q is the radiative heat input from the solar simulator (1 kWm^{-2}), $\overline{h_s}$ and $\overline{h_t}$ are the side and top cuvette surface natural heat transfer coefficients, respectively, $\overline{h_e}$ is the evaporation coefficient,[130] A_s, A_t, and A_T are the cuvette side, top, and total surface areas, respectively, T_∞ is the ambient air temperature ($T_\infty = T_{amb} \approx 24°C$), $P(T)$ is the water saturation pressure at the bulk nanofluid

temperature, φ is the relative humidity, and $P(T_\infty)$ is the water saturation pressure at the ambient temperature.

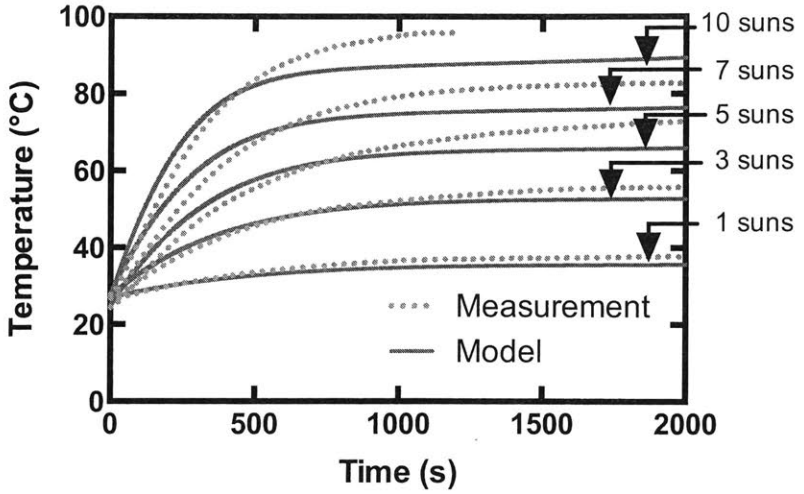

Figure 2.6. Graphitized carbon black nanofluid temperature as a function of time for 5 different solar concentrations. The experimental results are shown in red solid lines, while the analytical model results (Eq. (2.5)) are shown in blue dotted lines. The bulk fluid temperature was calculated by calculating the arithmetic mean of the four thermocouple probes in the nanofluid. The experimental error in the thermocouple measurement is approximately ±0.5°C.

Figure 2.6 shows the experimental and model results of the nanofluid temperature as a function of time for a range of solar concentration ratios ($1 < C < 10$ suns, see Methods). As the incoming solar light was absorbed by the nanofluid, the bulk fluid temperature began to rise due to sensible heating of the nanofluid. As the nanofluid temperature continued to increase, the evaporation rate and parasitic heat losses (*i.e.* natural convection and radiation) began to dominate the energy transfer mechanisms, until the steady state was reached ($t > 2000$ s) where all of the incoming solar energy was being converted to evaporation and parasitic heat losses.

The heat transfer model agrees well with the experimentally measured time-dependent temperature profile of the bulk nanofluid. This indicates that the fluid is directly heated *via* conduction by the absorbing nanoparticles at the surface and that vapor is not being generated at the nanoparticles themselves in a non-equilibrium fashion as described previously. If the vapor

was indeed generated at the nanoparticle, and not the liquid-air interface, the bulk temperature profile would be reduced, due to the localized heat generation.

Our model becomes less accurate in steady-state operation ($t > 2000$ s) due to the changing concentration of nanoparticles as water leaves the system, especially near the liquid-air interface. The evaporation of water left a concentrated layer of hydrophobic GCB particles, which formed a skin at the interface, and restricted evaporation. This reduced the evaporation heat transfer coefficient below that of pure water (used in the model), and contributed to the increasing temperature of the bulk fluid.[131] Furthermore, the latent heat of vaporization of nanofluids has been shown to potentially be significantly higher than the aqueous constituent alone,[132] leading to more energy required to evaporate the liquid water, lower evaporation rates, and higher steady-state temperatures. Although the lumped capacitance nanofluid model developed here does well at predicting the experimental behavior during nanofluid vapor generation, it fails to give a mechanistic understanding of the energy conversion mechanisms at the nanoparticle scale, which must be reconciled with additional modeling in order to gain a better understanding of the heat generation physics.

Particle Heating Model

To study the nanoparticle-fluid temperature difference, we used a 3D numerical simulation (COMSOL) to model an array of nanoparticles distributed evenly in a fluid medium. For such periodic structures, we can focus on the heat transfer in one unit cell to understand the entire structure. The COMSOL model consists of a particle-in-a-box, a single heated nanoparticle in a fluid domain (Fig.7a). The following details were used to construct the model. The dimensions of the box were based on the average nanoparticle spacing in the nanofluid, which for a 0.5 wt% GCB nanofluid was calculated to be ≈3 μm for a nanoparticle radius of 250 nm. The boundaries of the fluid box were insulated, due to symmetry (Fig.7b). A boundary heat flux was placed at the nanoparticle surface, which simulated the absorption of solar energy. The nanoparticle was assumed to be spherical, isothermal, and surrounded by liquid water. Only transient heat conduction was considered at these small length scales. Non-equilibrium nanoscale heat

conduction effects were not considered due to the relatively high interfacial conductance at carbon-water interfaces.[133,134]

At time scales on the order of a few seconds, the temperature variation across the fluid box was negligible, < 0.01 K. This is not surprising, as the spacing between nanoparticles in the fluid is very small (< 3 μm), and the corresponding Fourier number is high ($Fo > 10^4$). This further supports a global temperature rise in the fluid medium as the proposed mechanism of evaporation.[110] Only at very short time scales (~μs) and high solar intensities (~10^5 suns) can a temperature difference of 100K be found over the fluid box. This high solar concentration is roughly in agreement with the laser intensities required for nanobubble formation in previous studies, and is larger than achievable solar concentrations.[101,102,106]

To study the effect of overlapping thermal boundary layers of nearby nanoparticles on the bulk fluid temperature, the particle separation distance ($2L_{\text{fluid}}$) was varied. In previous works, models of a single nanoparticle in an infinite medium have been considered.[70,106] However, this ignores the heating effects of nearby nanoparticles in a real fluid and is only valid for short time scales where the individual heating profile has not reached the neighboring particles.[110,135] Fig.7c shows the fluid temperature profile as a function of normalized distance from the nanoparticle wall in the x-direction for different particle spacings (nanoparticle concentration) and a constant heating time of 2 μs. The results show that the 3μm box approaches the limit of the heated sphere in an infinite medium, and increasing the box size does not decrease the temperature profile of the liquid. Conversely, decreasing the fluid domain size to approach $L_{\text{fluid}} \approx 0.75$ μm resulted in significant thermal boundary overlap and fluid heating. The results show that the sustained heating of a large number of dispersed nanoparticles can produce a significant global fluid temperature rise.

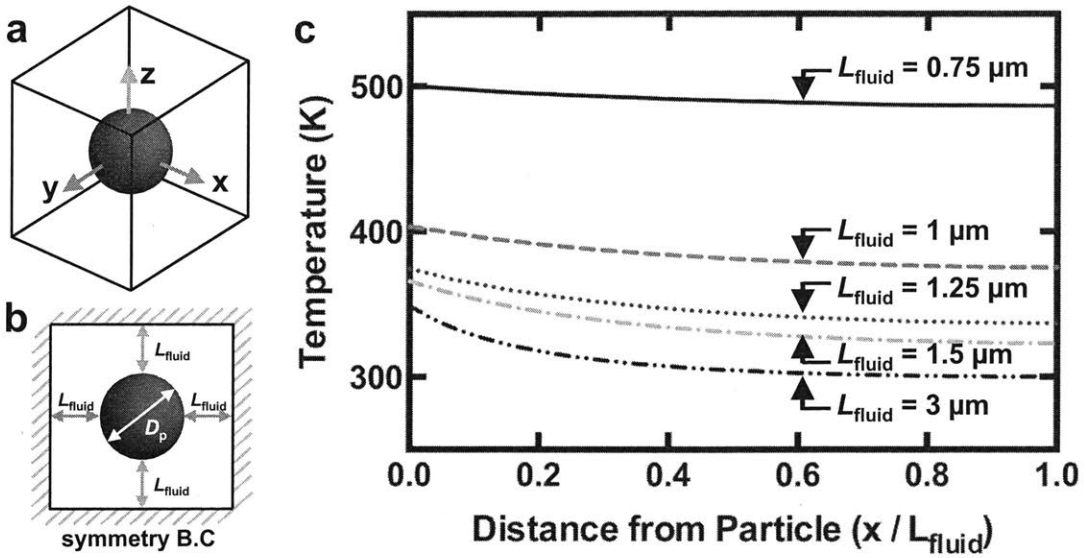

Figure 7. (a) Isometric view of the COMSOL model domain showing the heated nanoparticle (red sphere) in a fluid box surrounding it. (b) Side view of the fluid domain showing the critical simulation dimensions: particle diameter (D_p), and distance from the particle edge to the domain boundary (L_{fluid}). (c) Mean fluid temperature as a function of normalized distance from the nanoparticle wall for 5 different fluid domain sizes. As the fluid domain decreased in size, the fluid temperature increased due to the larger thermal boundary overlapping between particles.

A natural question is to compare using nanofluids versus surface absorbers for generating vapor. This thesis chapter has focused on evaporating water at temperatures below 100°C, and is expected to outperform (5-10%) a surface absorber designed for similar applications (see Supplementary section 2.15). Another related application is in solar boiling of water. Here, the nanofluid operates similarly to a surface absorber, since a tuned nanofluid will absorb sunlight at the surface for maximum heat concentration. A nanofluid-based absorber may have comparative advantages in high flux applications, due to its ability to increase critical heat flux[104,136]

2.6. Supplementary Section: Experimental Set-up

The vapor generation efficiency measurements were carried out using the set up shown in Figure 2.7. A solar simulator (ScienceTech, SS-1.6K) generated solar light that was reflected downwards using a mirror (Alanod, Miro Reflective 90), and passed through a Fresnel lens

(Edmund Optics, polymer 6-inch focal length). The solar radiation then passed through an aperture (polished copper, 25.1mm diameter), resulting in nearly all light being incident on the nanofluid. The solar simulator conforms to class A standards, according to ASTM E927-10. The mirror was +85% specularly reflective, with a total reflectance of +90%. The nanofluid was housed in a custom built container made of acrylic and aerogel pieces to limit parasitic side losses. The total weight of the container is less than 170g.

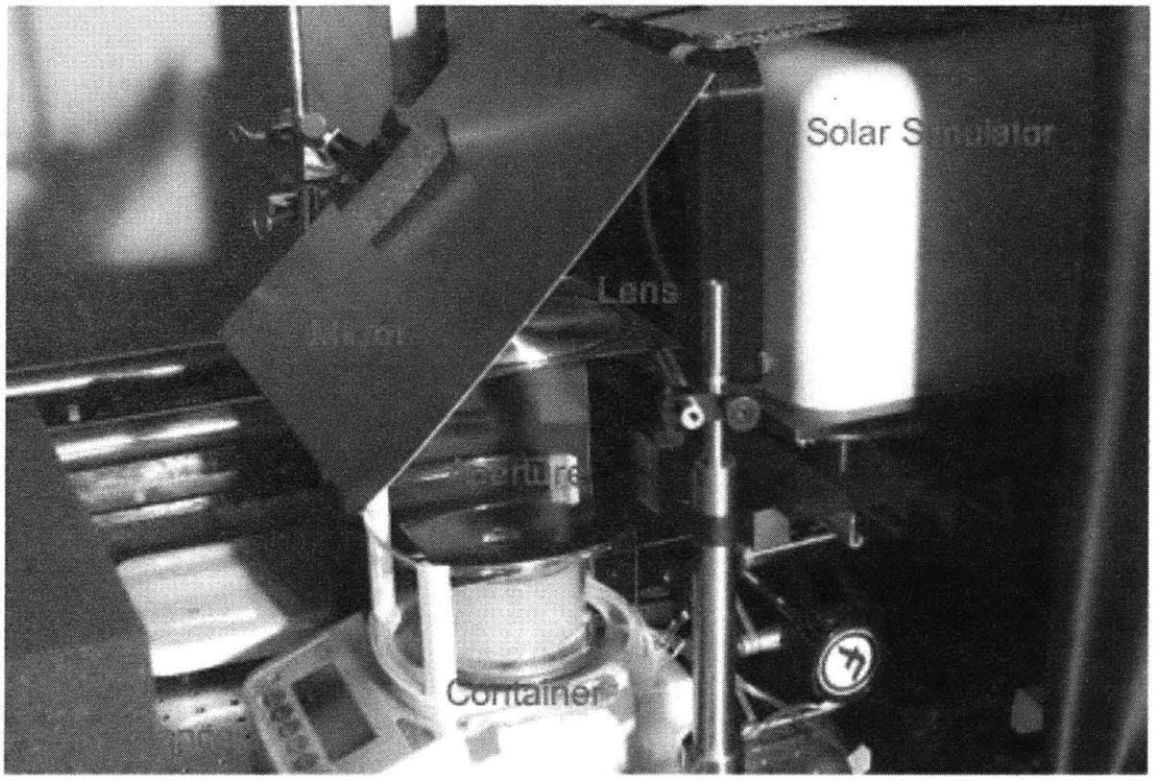

Figure 2.7: Efficiency testing setup for nanofluids-based solar receiver.

The nanofluid container is constructed out of two concentric acrylic tubes, with a layer of aerogel particles (Cabot, Lumira Aerogel Particles) in between to serve as an insulator to minimize radial heat losses. The aerogel particles are sealed from the environment with acrylic discs. The nanofluid is exposed to the ambient, to allow vapor escape. Four E-type thermocouples were inserted into the nanofluid container to measure the fluid temperature at different distances from the nanofluid-air interface. As the nanofluid evaporated, the fluid level dropped below each

thermocouple, allowing measurement of the liquid/vapor interface. The mass loss was measured using balance (A&D, FX300i) with a resolution of 1mg, and calibrated up to 300g.

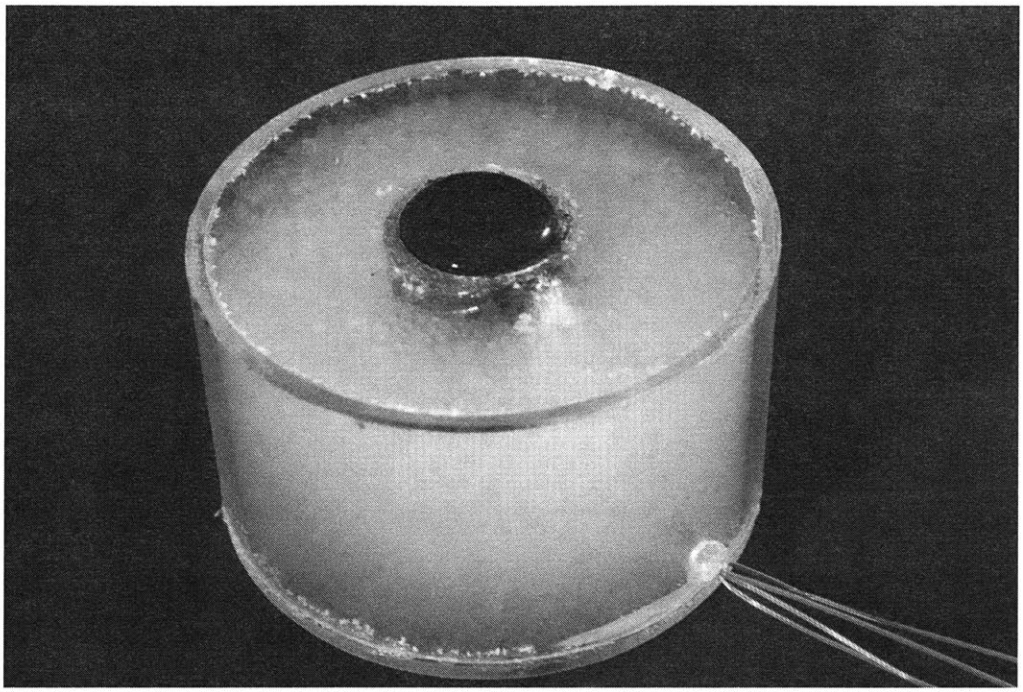

Figure 2.8: Close up picture of the nanofluids-based solar receiver.

The total incoming power at the nanofluid surface was measured using a thermopile (Newport, 818P-040-55, 40W, 55 mm diameter) and power meter (1918-c), and is around 5W. The copper aperture is placed in a fixed location, and not touched during the entire experiment. To capture all the solar radiation passing through the aperture, the thermopile is placed underneath, as close to the aperture as possible. Prior to the experiment, the power was measured at several times over a 10-minute interval, and the power fluctuation was less than 1%. The thermopile is then removed, the aperture covered with a metal foil, and the nanofluids container is placed underneath. The nanofluid container is briefly aligned to capture as much light as possible, and then the temperature is stabilized to ~25°C before the experiment begins. The mass is measured over a 10-minute period to ensure no drifting occurs, other than ambient evaporation of the nanofluid.

SEM images of the three different nanofluids were taken, and are shown in Section 2.9. The graphitized carbon black and carbon black look remarkably similar. In contrast, their transient

efficiency are the best and worst out of the nanofluids tested, respectively. This indicates the importance of surface effects on the performance of nanofluid evaporation.

2.7. Supplementary Section: Lumped Capacitance Model

A different experimental setup is used to compare with the heat transfer model, and is shown in Figure 2.9. This setup consists of direct illumination from the solar simulator (ScienceTech SS-1.6K) to a polymer cuvette holding 3mL of nanofluid. Water is allowed to evaporate to the ambient from the top. To measure the bulk liquid temperature, four E-type thermocouples are placed in the cuvette, entering the sides at different heights. The data is acquired using a DAQ board (NI USB-6210 with cold-junction compensation). A power meter (1918-c) and thermopile (Newport, 818P-040-55, 40W, 55 mm diameter) are used to measure the incoming solar radiation. Experiments are run for over one hour, and solar concentrations of 1, 3, 5, 7, and 10 suns are used.

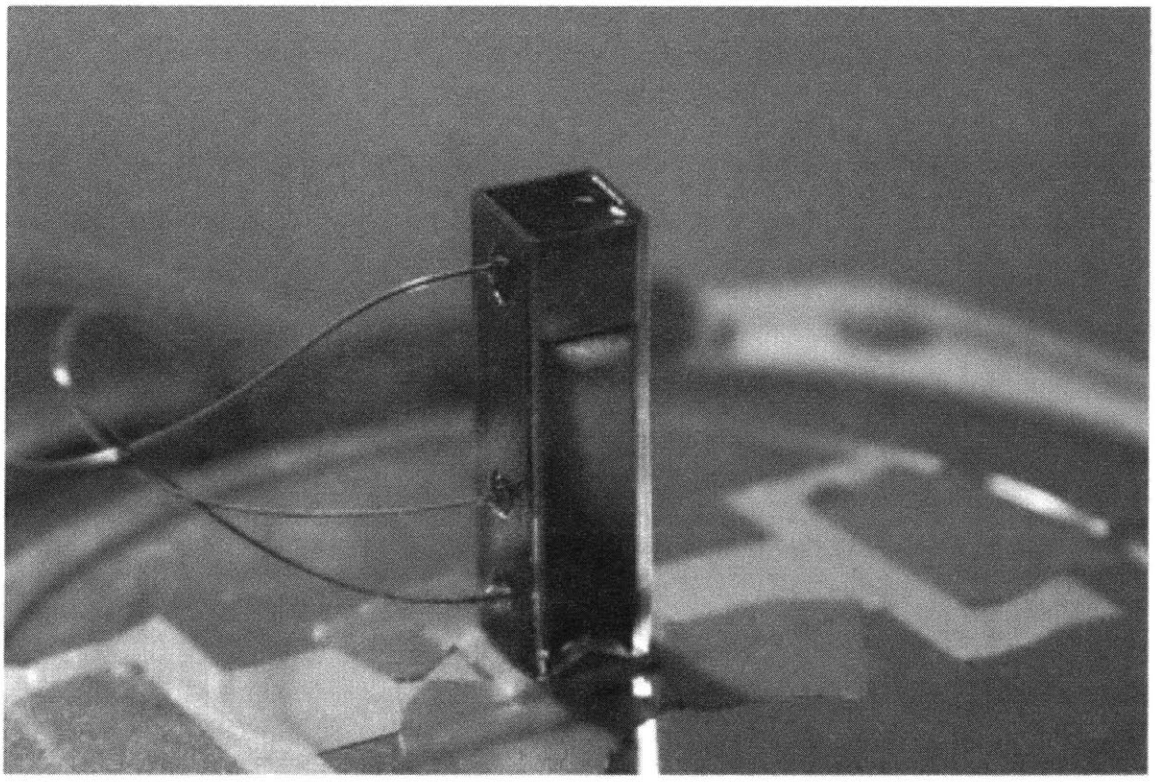

Figure 2.9: Cuvette nanofluids receiver built to compare with the classical heat transfer model.

To simplify the model, the following assumptions were made. All incoming radiation was absorbed in the nanofluid, and all surfaces emit blackbody radiation to the ambient temperature of 25°C. The fluid is isothermal, and the Biot number of 0.02 confirms this. This assumption is further confirmed by the thermocouples in the bulk fluid, where a maximum temperature difference of 4°C was measured. Average heat transfer coefficients are valid over all nanofluid and cuvette surfaces. The thermal resistances in the walls of the cuvette are negligible. A discrete simulation was used to model the transient temperature profile of the heat transfer equation.

To model the cuvette experiments, three heat transfer coefficients were used. The heat transfer values below are given for the case of the 1 sun experiment, with the steady state temperature used to determine the relevant dimension numbers. The Nusselt number for natural convection off a vertical plate[129] was

$$\overline{Nu_L} = 0.68 + \frac{0.387Ra_L^{1/6}}{\left[1 + \left(\frac{0.492}{Pr}\right)^{\frac{9}{16}}\right]^{4/9}} \tag{2.6}$$

and the heat transfer coefficient was 5.58 W/m^{2}K. For natural convection leaving the evaporating surface[129], the correlation was

$$\overline{Nu_L} = 0.54Ra_L^{1/4} \tag{2.7}$$

with a heat heat transfer coefficient of 13.44 W/m^{2}K. Pr is the Prandtl number, Ra the Rayleigh number, and Nu the Nusselt number. The evaporation heat transfer coefficient is 16.5x the natural convection coefficient[130], and was 221.8 W/m^{2}K.

The governing heat equation used is an energy balance accounting for the incoming solar radiation, the outgoing radiation emissions, natural convective losses, and the evaporation of the fluid. The fluid is treated as a lumped capacitance body.

2.8. Supplementary Section: Comsol Model of Experimental Setup

A COMSOL model was constructed to simulate the heat flows through the nanofluids container. The actual experiment involved a constantly lowering evaporation surface from the nanofluid, because water was continually leaving the system. To simplify the model, only a static heat transfer model was considered. To ensure model fidelity to the experiment, four boundary conditions were imposed: 1) evaporation efficiency, 2) incoming solar radiation, 3) evaporation surface temperature, 4) and temperature of the underlying bulk nanofluid at a specified depth. With these constraints matched, the temperature distribution in the COMSOL model matches the experimental conditions.

The following parameters were used in the COMSOL model. A natural convection heat transfer coefficient of 7 W/m^2K was used on all exterior surfaces of the model, as well as the evaporation surface. All surfaces had a surface emissivity of 1 for radiation losses to an ambient temperature of 25°C. The bottom of the container is insulated, due to low thermal contact with the environment. A solar flux of $10kWm^{-2}$ was incident on the evaporating surface. The evaporation heat transfer coefficient of the evaporating surface was fit to satisfy the aforementioned four boundary conditions. Three materials were used in the container: 1) water, to simulate the nanofluids, 2) aerogels with thermal conductivity 0.02 W/m^2K, specific heat 10 J/kgK, and density 100 kg/m^3, and 3) acrylic with thermal conductivity 0.18 W/m^2K, specific heat 1470 J/kgK, and density 1180 kg/m^3.

A temporal study was used to include the effect of heat storage in the temperature distributions. The time used (3000 s) to analyze the losses corresponds roughly to the time used to determine the four boundary conditions. The results of the COMSOL model are shown in Figure 2.10.

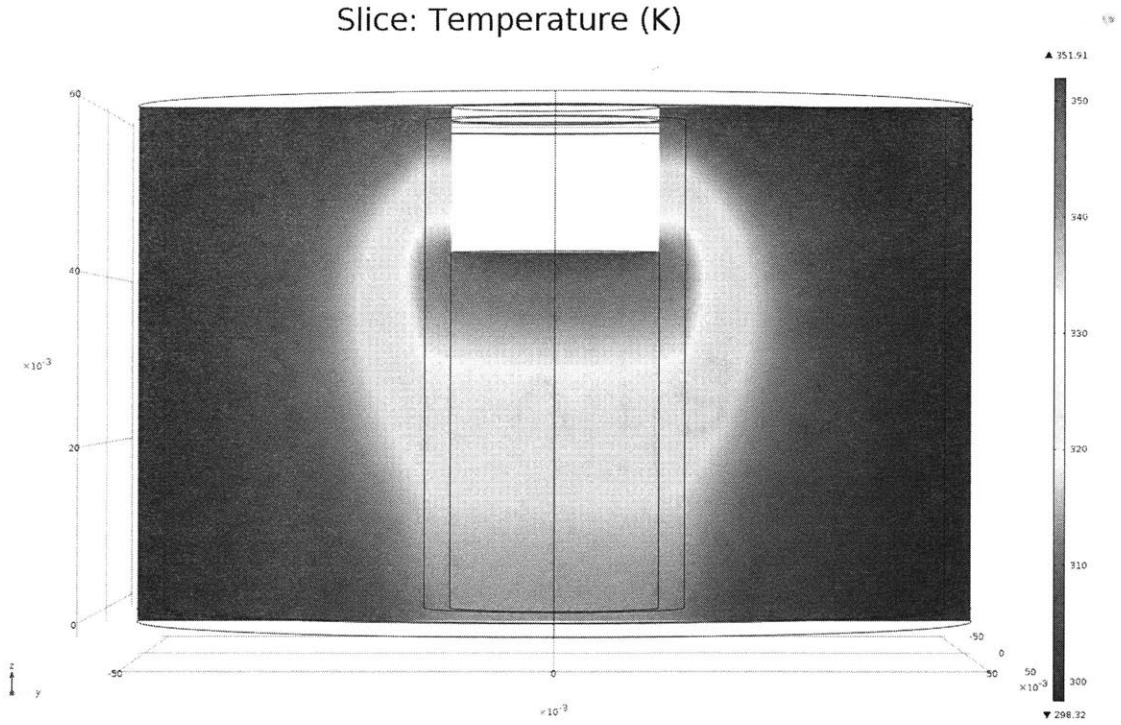

Figure 2.10: COMSOL model of the nanofluids-based solar receiver.

The four boundary conditions are closely matched with the COMSOL model, and the fitted evaporation rate corresponds to the evaporation measured in the experiment (69%). The radiation losses and convection losses from the evaporation surface are 4% and 3%, respectively. In a 1 cm slice of nanofluid directly underneath the evaporation surface, 9% is conducted radially into the container, and 9% are conducted axially into the nanofluid below. Only 12% is convected away from the outer surfaces of the container, which indicates the container is still being heated.

2.9. Supplementary Section: SEM Images

SEM images were taken of the three nanofluids to show their morphology. The morphology of GCB and CB are quite similar, despite the drastic difference in dynamic performance. The graphene nanoflakes are sheet like, as expected.

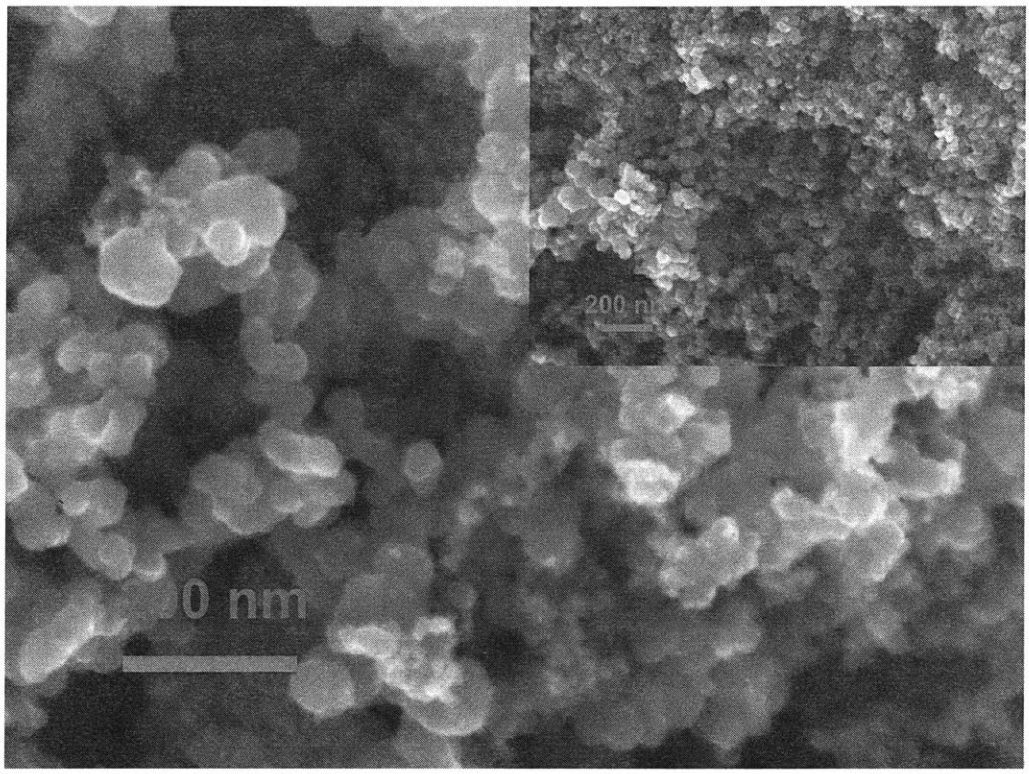

Figure 2.11: Carbon Black SEM image

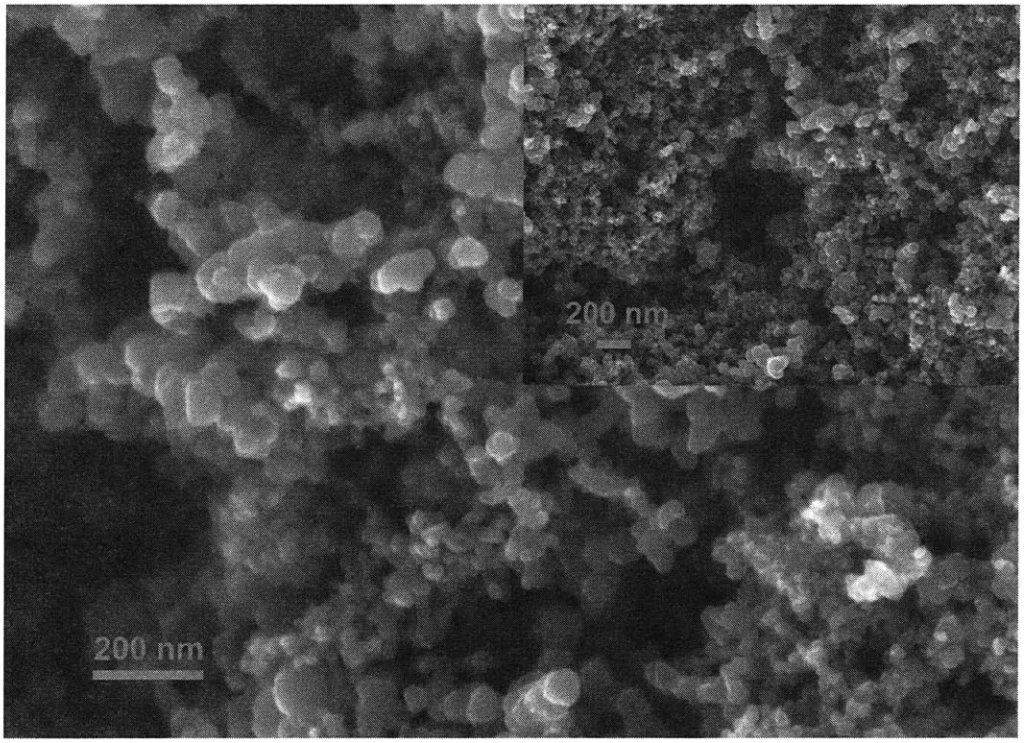

Figure 2.12: Graphitized Carbon Black SEM image

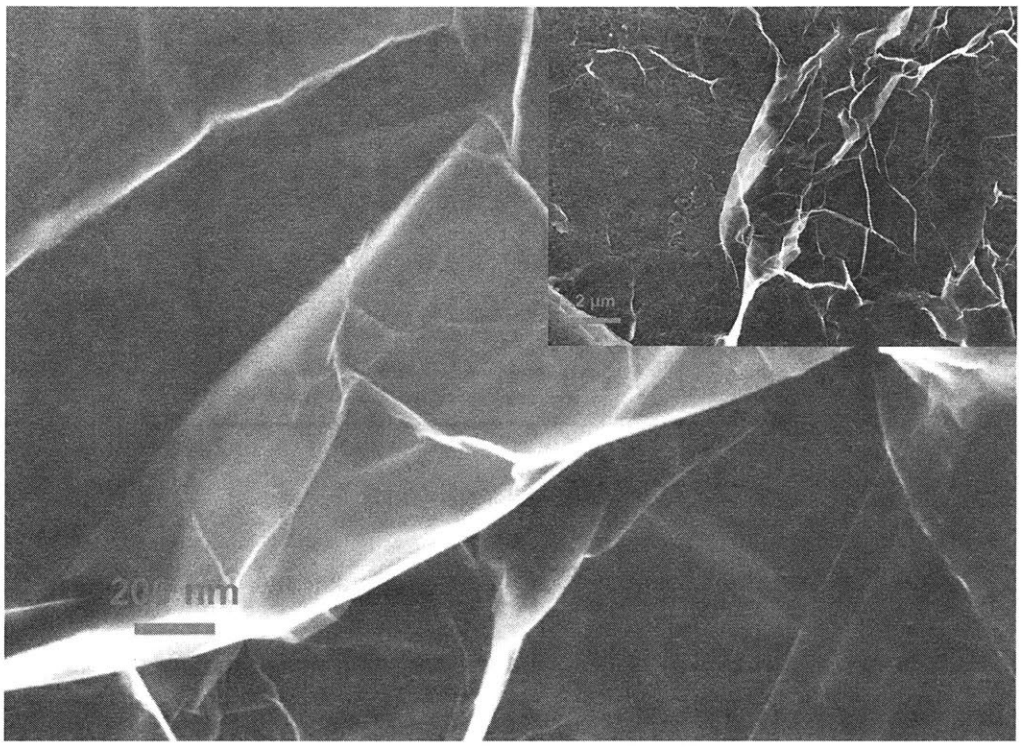

Figure 2.13: Graphene flakes exfoliated from graphite using an electrochemical method.[118]

2.10. Supplementary Section: Optical Properties

Specular reflectivity and direct-direct transmission data were taken for the nanofluids in the optical range of 350nm-1900nm, and is shown in Figure 2.14. A holder was constructed out of two microslide glasses with smooth surfaces to contain the nanofluids for the reflectivity measurement, which was made on a Cary 500i UV-Vis-NIR Dual-Beam Spectrophotometer. The microslide reflectivity were individually measured, and subtracted from the measurement with glass.

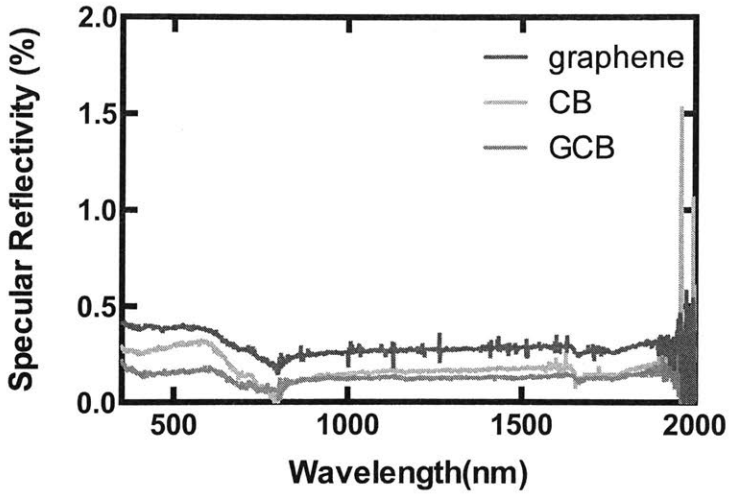

Figure 2.14: Specular reflectivity of GCB, graphene, and CB nanofluids.

A cuvette (Plastibrand, PMMA) was used in the transmission measurements. Transmission was below the detection limits of the UV-Vis spectrophotometer, across the entire spectrum.

2.11. Supplementary Section: Nanofluid Agglomerate Sizes

To estimate the extinction coefficient, the average nanoparticle agglomerate size was measured. The extinction coefficient could not be directly determined via transmission measurements, due to the strongly absorbing properties in the nanofluid. From the nanoparticle agglomerate size, and the volume fraction of nanoparticles, the minimum extinction coefficient can be estimated.

To measure the particle size of GCB, a dynamic light scattering (DLS) measurement (DynaPro NanoStar, Wyatt Technology Corporation) was performed. Peaks of 20nm and 120nm were seen, with 96% of the mass in the 120nm peak. The polydispersity was ~22%. These results indicate the average agglomerate size of the GCB fluid to be 120nm, with some free particles of 20nm. The 20nm peak corresponds with the particle sizes in the SEM images shown in Supplementary Section 2.9.

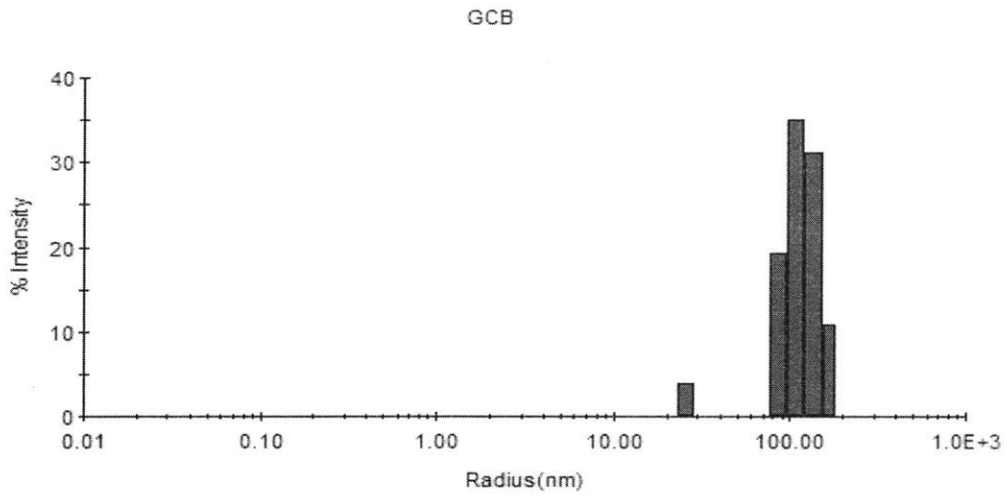

Figure 2.15: Results from a dynamic light scattering measurement of the GCB nanofluid

For determining the CB nanofluid agglomerate size, the dynamic light scattering measurement is not suitable, as the particle sizes were thought to be much larger. The DLS measurement was tried, but suitable data to match the light scattering model could not be obtained. Instead, the particle size was observed optically using an optical microscope. Figure 2.16 below shows the agglomeration structure of the CB nanofluid. The particles form large agglomerates, with diameter on the order of 1-50μm. For the purposes of our extinction coefficient estimation, we can start with a particle diameter of 5μm.

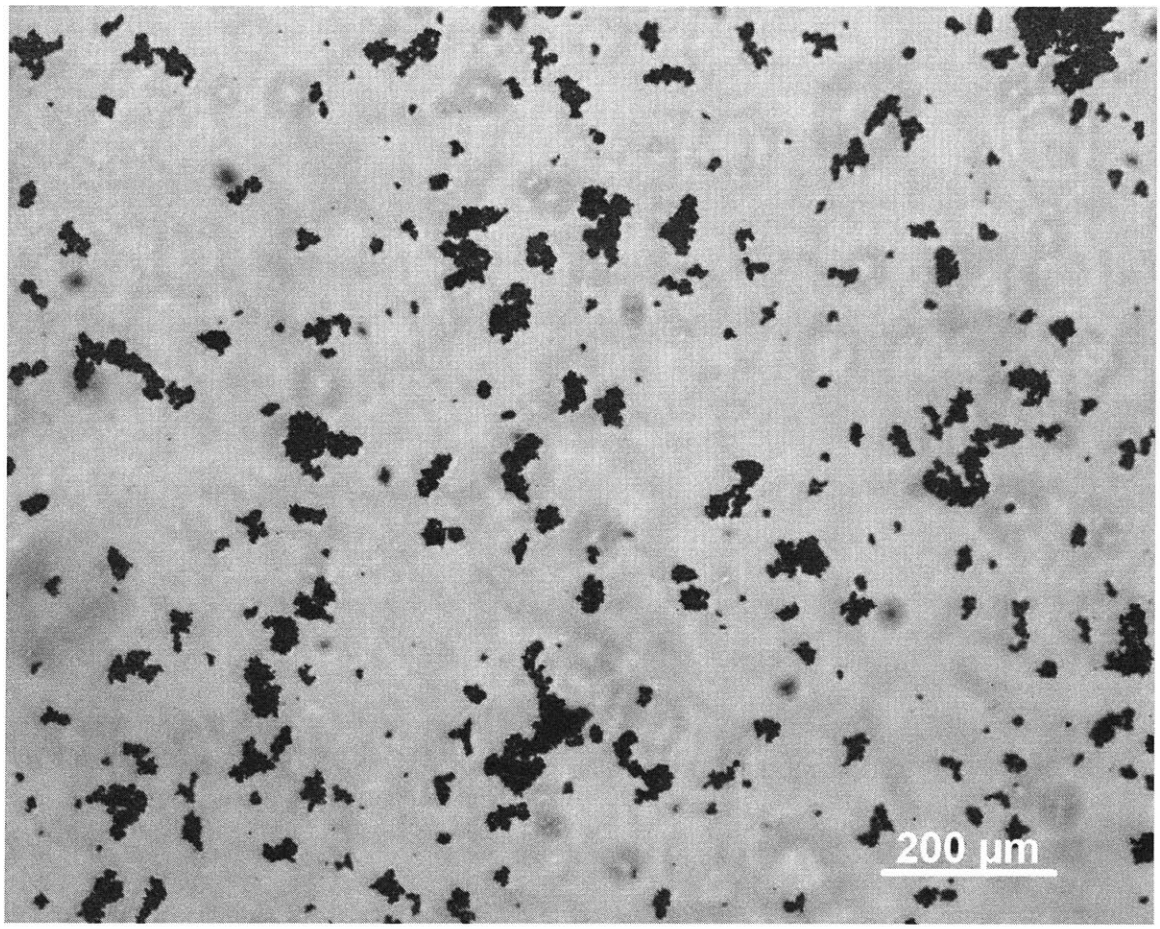

Figure 2.16: Optical image of the CB nanofluid. There is extensive agglomeration.

2.12. Supplementary Section: Nanofluid Absorption Calculation

The extinction coefficient can be calculated from the agglomerate size, using Lorenz-Mie theory for a single spherical particle in the independent scattering regime. We approximated the particle radius in Mie theory as the agglomerate radius in the previously mentioned optical measurements (GCB: 110 nm, CB: 2.5µm). The index of refraction is determined from literature, and the bulk values are assumed valid for the agglomerate.[128] The size of the box surrounding the particle was calculated using the volume fraction of the nanoparticles in the nanofluid. It can be seen that the agglomerate cross section grows with r^2, whereas the agglomerate volume grows with r^3. Intuitively, in the absence of strong resonant scattering effects, the larger particle should have a smaller absorption coefficient.

The efficiency factor Q was used to calculate the extinction coefficient using the following expressions,

$$\beta_{ext} = NQ_{ext}\pi r^2 \tag{2.8}$$

$$\kappa_{abs} = NQ_{abs}\pi r^2 \tag{2.9}$$

$$\sigma_{sca} = NQ_{sca}\pi r^2 \tag{2.10}$$

where N is the particle density, $Q_{ext}, Q_{abs}, Q_{sca}$ are the extinction, absorption, and scattering efficiencies. For the GCB, the interparticle spacing is 1.3 μm, and 30 μm for CB. In the studied nanofluids, the scattering and absorption cross sections are of similar magnitudes, and so a full equation of radiative transfer should be considered for an accurate determination of the heat generation in the nanofluid.[101] As an approximation, we use the extinction coefficient in Beer's law to model the heat generation within the nanofluid. This approximation underestimates the transient efficiency difference. Figure 2.17 shows the results of the Lorenz-Mie theory calculation for the scattering directions. In the case of the CB agglomerate, most of the scattered light is forward directed, and so the absorption coefficient would give a more accurate estimate of the heat generation locations. However, this would also overestimate the difference in transient efficiency. Using our transient efficiency model (see Section 2.13) we determined the sensitivity of transient efficiency to extinction coefficient. If our calculated extinction coefficients are overestimated, the sensitivity plot shows that the GCB transient efficiency is relatively unaffected, whereas the CB transient efficiency rises quickly with extinction coefficient.

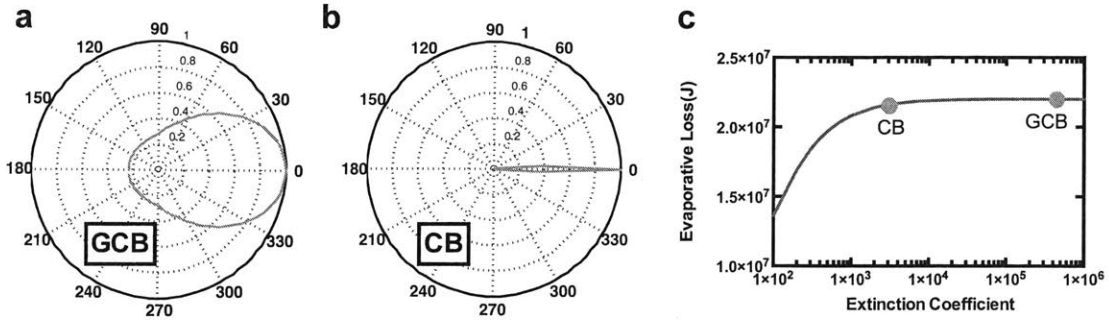

Figure 2.17: Normalized scattering phase functions for a)GCB and b)CB agglomerates using Mie theory. c) shows the sensitivity of transient efficiency to extinction coefficient.

Our calculations showed the GCB to have an extinction coefficient of $5.6\text{x}10^5\ \text{m}^{-1}$, and the CB to have an extinction coefficient of $1.6\text{x}10^3\ \text{m}^{-1}$. From this analysis, we can see that the extinction coefficient varied significantly, more than two orders of magnitude.

2.13. Supplementary Section: Transient Efficiency Model

The variation in extinction coefficient affected the temperature of the nanofluid evaporation surface, especially in transient conditions. The nanofluid surface temperature affected the evaporative flux and the vapor generation efficiency of the device. This effect was particularly strong in transient conditions. For longer absorption depths, the heat generated must diffuse further before reaching the surface. To check the effect of the nanofluid extinction coefficient on the surface temperature, a simple 1D model was constructed which simulated the absorption characteristics of the nanofluid, as well as the heat losses in the system.

The heat transfer model was based on the time-dependent Fourier's law, with an exponential heat generation term that follows Beer's law for light absorption. The governing equation, and boundary and initial conditions are shown below.

$$\frac{\partial \Theta(x,t)}{\partial t} = \alpha_x \frac{\partial^2 \Theta(x,t)}{\partial x^2} + \frac{q_0 \lambda e^{-\lambda x}}{\rho c_p} \tag{2.11}$$

$$\Theta(H,t) = 0 \tag{2.12}$$

$$-k_x \frac{\partial \Theta(0,t)}{\partial x} + h\Theta(0,t) = 0 \tag{2.13}$$

$$\Theta(x,0) = 0 \tag{2.14}$$

θ(x,t) is the temperature difference from ambient, x is the position along the nanofluids receiver, t is the time after illumination, H is the length of the nanofluids receiver, A_c is the cross sectional area for absorption, λ is the extinction coefficient, k is the nanofluid thermal conductivity, h is the evaporation heat transfer coefficient, α is the thermal diffusivity, ρ is the density of the fluid, c_p is the specific heat, and q_0 is the incident solar flux on the receiver. The boundary conditions of the model were a convective term on one side, which represented evaporation, and a temperature boundary condition on the other side. At initial conditions, the entire model was at ambient temperature. Heat is generated closer to the convective side of the model. The model was solved using the Green's functions method. The full transient and steady-state solution is shown in Section 2.13. The results are simulated using MATLAB, and the effect of extinction coefficient on surface heat flux compared.

$$\Theta(x,t) \tag{2.15}$$
$$= \frac{q_0}{k\lambda}\left[-e^{-\lambda x} + \frac{e^{-H\lambda}\left(1+\frac{hH}{k}\frac{x}{H}\right)}{1+\frac{hH}{k}} + \frac{\left(H\lambda+\frac{hH}{k}\right)}{\left(1+\frac{hH}{k}\right)}\left(1-\frac{x}{H}\right)\right]$$
$$-\frac{2q_0\lambda H^2}{k}\sum_{m=1}^{\infty}\frac{(\beta_m H)^2+\left(\frac{hH}{k}\right)^2}{\left((\beta_m H)^2+\left(\frac{hH}{k}\right)^2\right)+\frac{hH}{k}}\frac{\left(H\lambda+\frac{hH}{k}\right)\sin(\beta_m H)+e^{-H\lambda}\beta_m H}{(H\lambda)^2+(\beta_m H)^2}$$
$$\times\sin[\beta_m(H-x)]\frac{e^{-(\beta_m H)^2\frac{\alpha t}{H^2}}}{(\beta_m H)^2}$$

θ(x,t) is the temperature difference from ambient, x is the position along the nanofluids receiver, t is the time after illumination, L is the length of the nanofluids receiver, A_c is the cross sectional

area for absorption, λ is the extinction coefficient, k is the nanofluid thermal conductivity, h is the evaporation heat transfer coefficient, α is the thermal diffusivity, and β_m is the eigenvalue.

2.14. Supplementary Section: Varying Weight Fraction of Nanoparticles

The previous sections described how the different nanoparticles created varying extinction coefficients in the nanofluids, due to the different agglomeration characteristics. Another way to test the effect of extinction coefficient on transient efficiency is to keep the nanoparticle constant, but vary the weight fraction to get varying extinction coefficients. We conducted a comparison by measuring the transient efficiency of a GCB-based nanofluid with lower weight fraction (0.005 wt%), which created a fluid with a calculated extinction coefficient of 5.6×10^3 m^{-1}. We compared this fluid with the previous measurements of GCB (5.6×10^5 m^{-1}) and CB (1.6×10^3 m^{-1}), and found that the diluted GCB did indeed have a transient performance in between the GCB and CB. The results are shown in Figure 2.18. This confirms our hypothesis that the extinction coefficient of a nanofluid can have a strong effect on the transient efficiency in vapor generation.

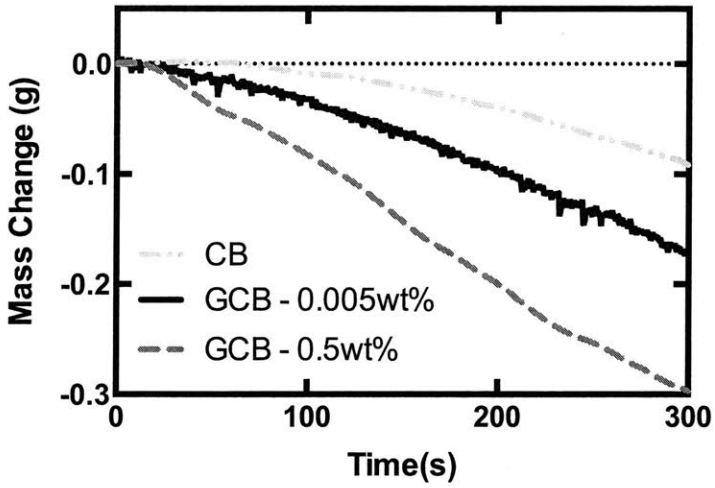

Figure 2.18: Comparing the transient efficiency of GCB nanofluids with varying nanoparticle concentrations to show the dependence on extinction coefficient.

2.15. Comparison with a Surface Absorber

A direct comparison between nanofluid and surface absorbers is difficult, as each approach operates best at different regimes. To attempt an analysis for evaporation efficiency, we must

make an assumption about the configuration of the surface absorber (Figure 2.19).

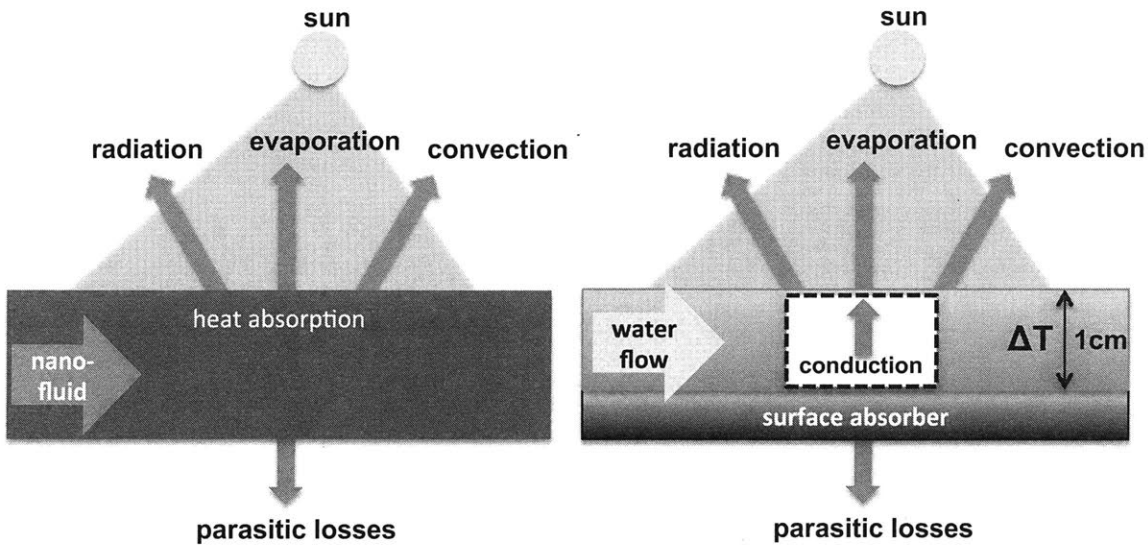

Figure 2.19: Nanofluid and surface absorber based solar evaporation configurations.

In the surface absorber, solar absorption occurs farther from the evaporation surface (~cm), compared to the nanofluid absorber (~ μ m). The larger separation in Figure 2.19 results in additional resistance from absorber to evaporation, and heat is forced towards other pathways (parasitic losses).

The following assumptions were made in this simple calculation: Conduction is assumed to dominate in the thin water layer. The evaporation heat transfer coefficients were determined experimentally in our lab (below), from a previous work.[137] Water is assumed to behave as a blackbody, based on its high optical loss constants in the infrared.[138] Given the thickness of the water layer (1cm) and the optical absorption coefficient of water (10^4-10^5 m^{-1}), it is unlikely for the emittance to be lower than 0.98, with the imperfection emittance due to some IR reflection. The convection heat transfer coefficient above the water is assumed 8 W/m^2K. The combined parasitic losses is determined from the nanofluid received experiments to be ~31 W/m^2K, and is assumed to be identical in the surface absorber case.

In this specific comparison, the nanofluid absorber can produce lower temperature vapor at efficiencies 5-10% higher (Figure 2.20). At higher temperatures, the surface absorber will start to boil at the surface-water interface, and a different comparison is warranted. Briefly, in the case of

generating 100°C steam via boiling, the nanofluid absorber is expected to perform similarly to the surface absorber, since both can generate phase change near the solar absorption location. However, a nanofluid absorber can have versatile and simple geometries, such as in applications for developing countries.[117]

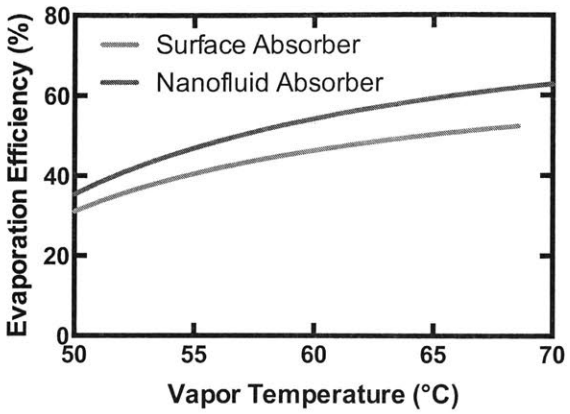

Figure 2.20: Comparison of surface and nanofluid absorber efficiencies for low temperature vapor generation.

2.16. Outlook for Nanofluids-Based Solar Vapor Generation

In the future, it would be interesting to investigate methods to further increase the temperature of the generated vapor *via* vapor flow restriction. By confining the vapor escape from the nanofluid receiver, the evaporation heat transfer and overall heat transfer coefficient of the entire device decreases, increasing the temperature of the fluid within. In addition, the capability of directly generating steam at elevated pressures needs further investigation. Typically, in a power generation cycle, high temperature pressurized steam is required for efficient operation, with steam-based Rankine cycles using steam at temperatures in the range of 300-500°C. Currently, a more suitable power application for our small-scale device is the organic Rankine cycle, which requires working fluid temperatures of only 100-200°C.[139,140] Another potential area for future work is developing approaches for superheating the generated steam using solar energy to high temperatures for power generation applications. In applications requiring turbines, condensing liquid from the working vapor causes erosion on the turbine blades, and increases costs.

Another area for future work is in integrating nanofluids into current cycle designs, such as a solar absorption cooling cycle. Depending on whether a system is closed-loop or open loop, the fluid influx can contain respectively nanoparticles or pure fresh water. In the closed-loop case such as an absorption refrigeration cycle, the nanoparticles are small enough to pass through pumps, and the various concentrations of fluids can be remixed. In an open-loop cycle, when operating at steady state, fresh water is required to feed the receiver and balance the water vapor leaving the system. This ensures a constant nanoparticle concentration. Possibly a mixing element will be needed to evenly disperse the nanoparticle, but pumps in a closed-cycle can accomplish this task. In general, agitation tends to decrease the aggregation of the system, as evidenced by the nanofluid preparation (ultrasonication bath for dispersing). This actually increases the effectiveness of the volumetric receiver, as shown in the Figure 2.3.

2.17. Summary of Nanofluid-Based Solar Vapor Generation

In summary, we demonstrated a high efficiency (69%) nanofluids-based solar receiver for direct vapor generation, using low concentration sunlight (10 suns). At such low solar concentrations, a nanofluid solar receiver may be used in lower cost systems that do not require the use of active sun-tracking devices, although monthly repositioning may be required. Three water-based nanofluids, graphitized carbon black, graphene, and carbon black, were tested in the receiver. We experimentally demonstrated and theoretically verified that in transient situations, such as in solar vapor generation, the graphitized carbon black and graphene nanofluids outperformed the carbon black nanofluid by 7%, after 1.5 hours of illumination. To show global fluid temperature rise as the more accurate vapor generation mechanism for nanofluids at the studies solar concentrations ($1 < C < 10$ suns), we constructed heat transfer models for the receiver at the device and nanoparticle scales. The device scale lumped capacitance model closely predicted the bulk temperature response of the nanoparticle receiver. The particle model showed that at feasible solar concentrations and illumination times, it is highly unlikely to achieve local temperature gradients leading to nanobubble generation around the nanoparticle, as proposed previously.

This research presented in this thesis chapter demonstrates a solar vapor generation platform that promises to be low cost and scalable for a wide-range of solar-based desalination applications.

Chapter 3

3. Solar Steam Generation without Concentrating Optics

Although the previous chapter on nanofluids introduced a technology with potential for easy deployment, and could generate vapor at high solar efficiencies of ~69% efficiency, it relied on expensive optical concentrators to amplify the incoming sun's power. Optical concentrators are often required for solar receivers to reach high operating temperatures (≥100°C) due to the associated high heat losses. However, optical concentrators can be costly and are one of the main impediments to solar thermal technologies being widely adopted. An alternative approach to reach high operating temperatures is by reducing parasitic heat losses. In this chapter, a new, simple solar steam generator is discussed which can generate steam *without* requiring optical concentration. This reduces system costs orders of magnitude, and lowers the technological requirements for solar steam generation.

3.1. Optical Concentration and Solar Thermal Steam Generation

Steam and vapor generation is often desired in many solar thermal applications, but the dilute solar flux (1000 W/m^2) does not provide enough power per unit area of the absorber to reach the required high temperatures and to compensate for the large latent heat of vaporization for water. Optical concentrators such as parabolic troughs, heliostats and lenses can concentrate the ambient solar flux tens or even thousands of times to achieve high temperatures.[8–12] Plasmonic nanoparticles with absorption and scattering cross-sections exceeding their geometrical cross-sections have been recently developed and applied for direct solar steam generation[13–24], but they typically require optical concentration of 10-1000x for steam generation. However, optical concentrators are expensive ($200/m^2)[25], often accounting for a major portion of the capital cost of solar thermal systems.[8,11,26] In addition, they require support structures and access to electrical energy to track the sun. Although optical concentration is currently necessary for applications that require high temperatures such as concentrated solar power generation, solar thermal technologies that reduce or completely eliminate the reliance on optical concentration would

have better market penetration. Worldwide, the use of non-concentrated solar thermal power (~200 GW)[27] outnumbers the use of concentrated solar thermal power (~5GW).

We recently demonstrated solar-steam generation under low (≤ 10x) optical concentration using a floating graphite-based two-layer solar absorber.[28] This structure localized the solar heat generation to the evaporation surface of a body of water, instead of wastefully heating the entire body of water. The structure's top layer absorbed the solar flux, while the bottom layer limited conduction of the generated heat to the underlying body of water. This resulted in very high steam generation efficiencies of up to 85%. However, to reach 100°C for steam generation, a solar flux of 10 kW/m^2, 10 times the normal sun (1000 W/m^2), was needed by optical concentration. Several other groups have looked into the role of surface chemistry in aiding water delivery and thermal insulation of the bottom layer,[20] incorporating plasmonic or carbon-based absorption layers,[29–33] and using other cheap and abundant materials.[34,35] These studies have achieved relatively high evaporation efficiencies, but relied on optical concentration to boost the evaporation temperatures and achieve such efficiencies. For example, Ito *et al.*[29] used a concentration of 9x to achieve steam generation. To achieve boiling point without optical concentration, solar receivers must be designed to suppress parasitic heat losses from the absorber surface.

In this chapter, we demonstrate water boiling and steam generation *under unconcentrated ambient solar flux* in a receiver open to the ambient. The receiver is constructed of a variety of low cost and commercially available materials utilizing a combination of spectral selectivity of the solar absorber, thermal insulation, and in-plane thermal concentration. By varying the thermal concentration, the receiver can generate saturated steam at 100°C, or low temperature vapor at high efficiencies (64%). The ability to boil water under ambient sunlight holds promise for significant cost reduction of existing solar thermal systems while opening up new applications such as desalination, waste water treatment, and sterilization.

3.2. Generating High Temperatures with Low Solar Flux

Achieving steam generation using the ambient solar flux (1000 W/m^2), or one sun, requires significant reduction of the heat losses from the receiver. Figure 3.1a shows the heat transfer processes involved in a floating solar steam generator, including radiative and convective heat

loss to the ambient and conductive and radiative heat loss to the underlying water. The net evaporation rate $\dot{m}$ can be expressed as

$$\dot{m}h_{fg} = A\alpha q_{solar} - A\varepsilon\sigma(T^4 - T_\infty^4) - Ah(T - T_\infty) - Aq_{water} \quad (3.1)$$

where h_{fg} is the latent heat, A the surface area of the absorber facing the sun, α the solar absorptance, q_{solar} the solar flux, ε the emittance of the absorbing surface, σ the Stefan-Boltzmann constant, h the convection heat transfer coefficient, and q_{water} the heat flux to the underlying water including conduction and radiation. Assuming a blackbody absorber with $T =$ 100°C, the minimum temperature needed for boiling water at ambient conditions, and $T_\infty =$ 20°C, the radiative heat loss to the ambient is 680 W/m^2. Taking a natural convection heat transfer coefficient of 10 W/m^{2}K, the convective heat loss is 800 W/m^2. These two loss channels alone exceed the incoming solar flux of 1000 W/m^2, and there is additional heat loss to the underlying water by conduction and radiation.

The large mismatch between water's latent heat of vaporization h_{fg} (2.26 MJ/kg at 100°C) and the ambient solar flux imposes another challenge. Even without any parasitic energy losses, the maximum mass flux generated by the ambient solar flux is $\dot{m}/A = q_{solar}/h_{fg} = 4.4\times10^{-4}$ kg/m^{2}s, according to Eq. (3.1). Our past studies[28] have shown that the mass evaporation rate of water at 100°C can be an order of magnitude higher (up to 4.3×10^{-3} kg/m^{2}s).

3.3. Heat Transfer Strategy for Steam Generation Under One Sun

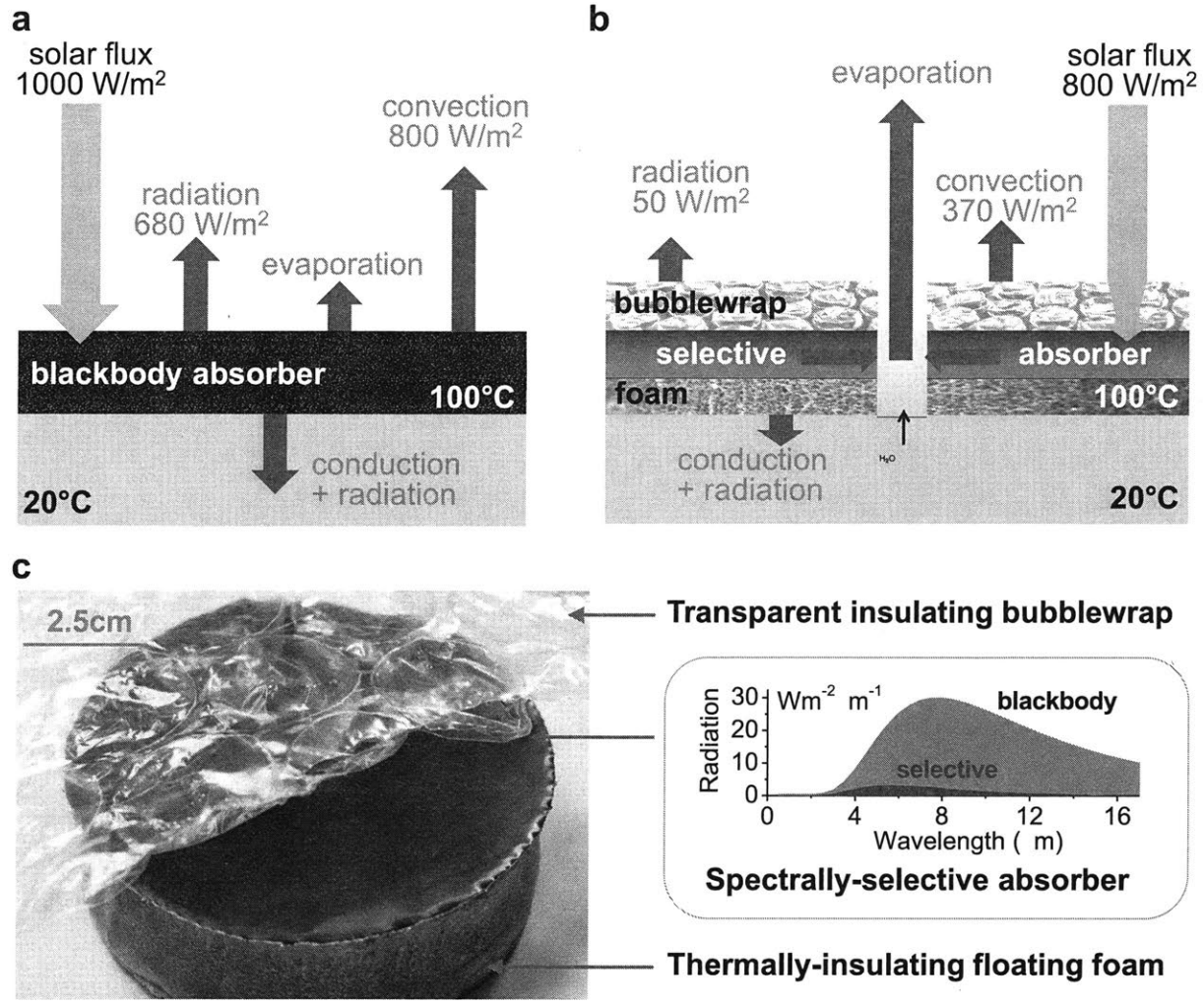

Figure 3.1: Operating principles of steam generation at 1 sun. a, Energy balance and heat transfer diagram for a blackbody solar receiver operating at 100°C. The 1000 W/m^2 delivered by the ambient solar flux is not enough to sustain the heat losses, and a 100°C equilibrium temperature cannot be reached. b, Energy balance and heat transfer in the developed one-sun ambient steam generator (OAS). c, A photograph of the OAS composed of a commercial spectrally selective coating on copper to suppress radiative losses and to thermally concentrate heat to the evaporation region. The bubblewrap cover transmits sunlight, and minimizes convective losses. Slots are cut in the bubblewrap to allow steam to escape. Thermal foam insulates the hot selective absorber from the cool underlying water, and floats the entire structure. The inset

compares thermal radiative losses at 100°C from a blackbody and the spectrally selective absorber.

Figure 3.1b shows several strategies we used to overcome the above challenges to achieve continuous steam generation under one sun, and even lower solar flux as shown later. First, we replace the blackbody absorber with a *spectrally selective absorber,* which has high solar absorptance α and low thermal emittance ε. Spectrally selective absorbers strongly absorb sunlight, but emit very little radiative heat. They are already widely used in domestic solar hot water systems,[36,37] and allow evacuated solar hot water tubes to be heated to over 100°C under stagnation conditions.[38] However, these solar hot water heating systems are not designed for steam generation or evaporation from open bodies of water. Second, we use *thermal insulation* on both top and bottom surfaces of the absorber to reduce convective loss to air as well as conductive and radiative heat losses to the water underneath. Finally, to overcome the mismatch between the latent heat of vaporization and the ambient solar flux, we use *thermal concentration*, by conducting the absorbed heat into the evaporation area, which is smaller than the absorber surface area.

3.4. Lab Prototype of One-sun, Ambient pressure, Steam generator (OAS)

Figure 3.2 A lab-scale One-sun, Ambient Steam-generator (OAS) was developed from three main components. First, a spectrally selective solar absorber is used, consisting of a cermet (BlueTec eta plus) coated on a copper sheet. Second, a thermal insulator was constructed from a polystyrene foam disk. Last, a convective cover was made from a sheet of large transparent bubble wrap. We use a variety of low-cost commercial materials to construct the solar receiver, and we believe even cheaper materials can be substituted for intended applications as discussed later; one example is using alternative selective coatings.

The spectrally selective absorber (Figure 3.2a) solar absorptance ($\alpha = 0.93$) and emittance at 100°C ($\varepsilon = 0.07$) were both measured and are shown in the Section 3.9. The polystyrene foam shown in Figure 3.2b,c serves to float the entire structure on a body of water, and is a thermal insulator ($k = \sim 0.03$ W/m-K). A channel was drilled through the foam, and a hydrophilic cotton wick threaded through. This wick used capillary forces to deliver water to the absorber. A sheet of cotton fabric (Figure 2b) was placed above the wick on the foam to increase the evaporative

area. Figure 3.2d shows an evaporation slot cut into a 10cm diameter selective absorber, to allow for water vapor to escape. The slot was varied in length (1mm width) to control the operating temperature of the receiver. For smaller thermal concentrations, 2-3 slots were made in a concentrated cluster (~5-10mm separation).

A sheet of transparent bubble wrap (Figure 3.2c) placed on top of the selective absorber to minimize the convective losses. The solar transmittance τ_{bubble} of the bubble wrap was measured to be 80%. Though the bubble wrap reduces the solar power transmitted and absorbed by the absorber surface, it also reduces the convective heat losses. The result is a net improvement in the OAS performance.

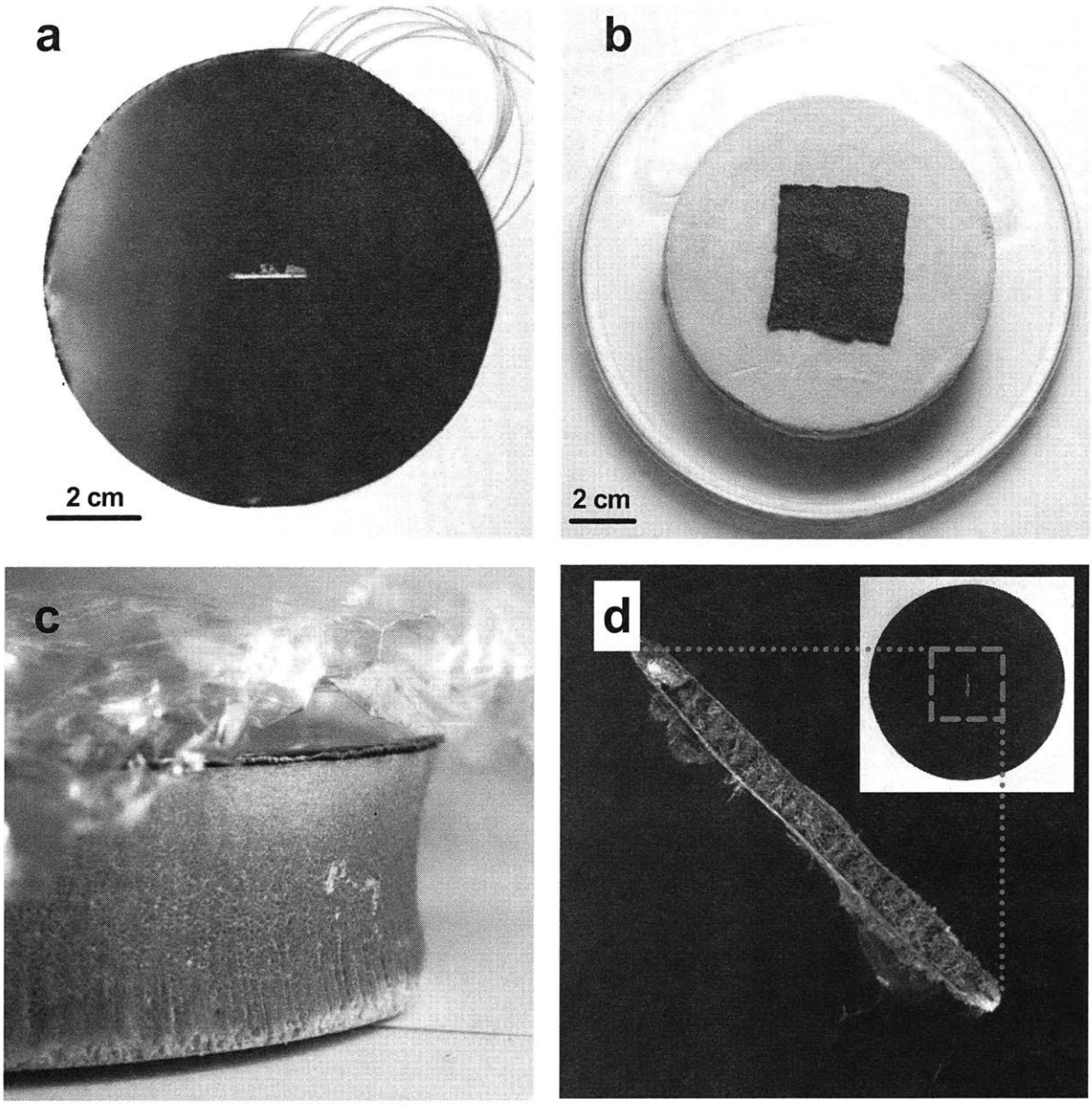

Figure 3.2: A one sun, ambient steam-generator. (a) The selective absorber consists of a commercially available cermet-coated copper substrate. (b) The insulation foam serves to float the entire structure on a body of water, and limits the thermal conduction and radiation to the cool water underneath. The dark fabric in the center hides a fabric wick, which tunnels through the foam to the underlying water. The fabric draws water through the foam. The clear container surrounding the foam holds water, and has a cap to prevent extraneous evaporation. (c) The three layers of the OAS, from top to bottom: bubble wrap, selective absorber, and thermally insulating foam. (d) The evaporation slot, which reveals the dark fabric underneath. The fabric serves to

deliver water, but also increases the evaporation area. The inset shows where the evaporation slot is cut.

3.5. Experimental performance of OAS

The lab-scale OAS performance was first characterized in a laboratory environment (Section 3.9). A solar simulator was used to supply solar flux (1000 W/m^2), and a balance was used to measure the real-time mass loss of the receiver and water supply. The selective absorber temperature and vapor temperature were measured (Figure 3.3a) as a function of the thermal concentration C_{therm}, the ratio of the total illumination area to the evaporation area. The vapor temperature closely tracks the selective absorber temperature. The maximum steam temperature reached was 98°C (Figure 3.3b), achieved when ~0.1% of the surface is devoted to evaporation (C_{therm} = 1300x). The steam temperature was directly measured by the thermocouple in this case, using a small vapor chamber. The kink near $t = 300$ seconds clearly indicates boiling limiting further temperature rise of the solar receiver, despite the measured vapor temperature not exactly reaching 100°C due to the rapid cooling of vapor. Figure 3.3c shows the mass change as a function of time while generating 80°C vapor. These figures show the receiver reached steady-state operation in roughly 5 minutes, clearly demonstrating continuous steam generation under 1 sun illumination.

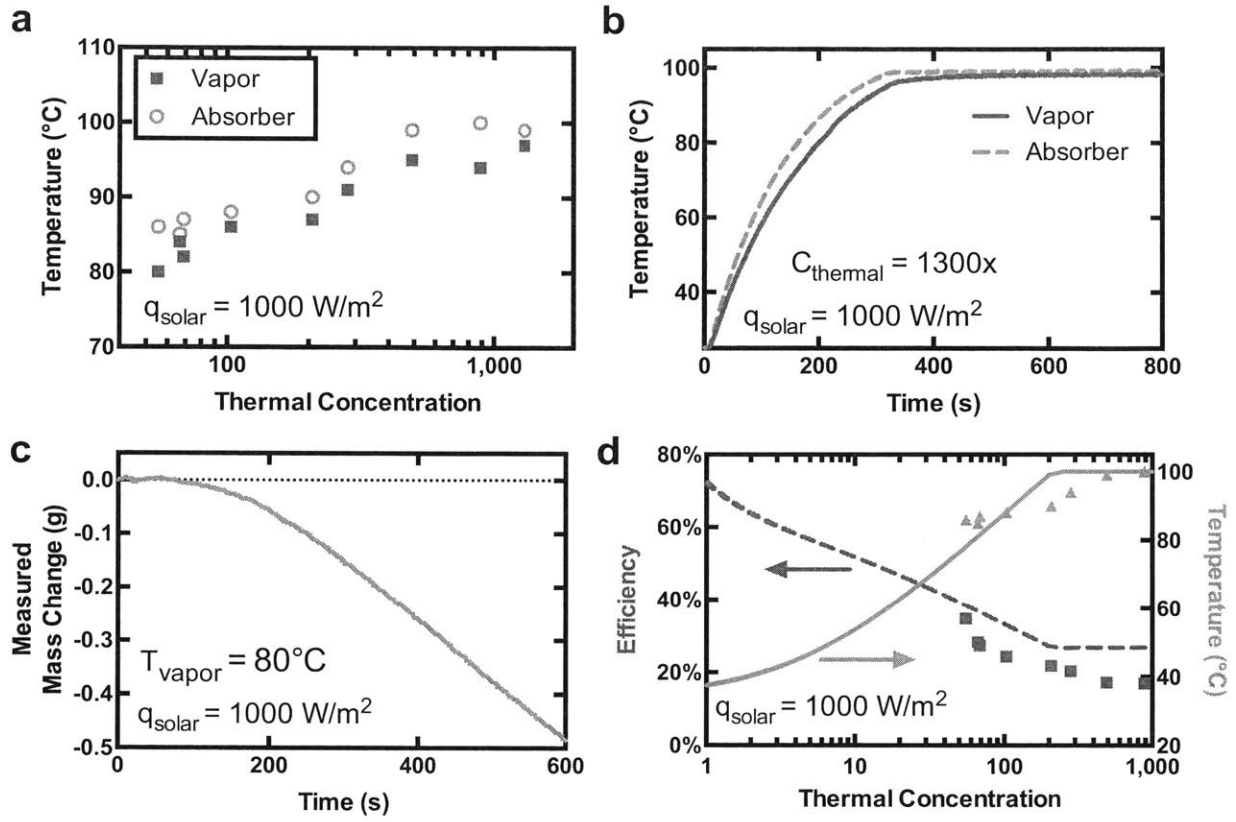

Figure 3.3|Vapor generation measurements. (a) Steady-state vapor and selective absorber temperatures measured as a function of the thermal concentration used. The evaporation slots were varied in size to control the operating temperature. (b) Vapor and selective absorber temperatures vs. time at thermal concentration of 1300x. The vapor temperature was directly measured with a small vapor chamber that was placed over the evaporation area. The kink in temperature rise is due to phase change. (c) Mass change over time, when the produced vapor temperature is 80°C. The OAS quickly reaches steady-state condition. (d) Shows efficiency of the receiver vs. thermal concentration. The dots are measurements, and the lines are computed by using the OAS heat transfer model (Section 3.10).

The solar vapor generation efficiency was defined as a ratio of enthalpy change in the generated vapor divided by the total incoming solar flux:

$$\eta_{thermal} = \frac{\dot{m}h_{fg}}{q_{solar}A}, \tag{3.2}$$

where $\dot{m}$ is the instantaneous mass change due to evaporation, h_{fg} is the enthalpy change of liquid water to vapor, q_{solar} is the solar flux per area, and A is the total area of the receiver. The enthalpy due to specific heating of the generated vapor is not included in the efficiency expression because the experiment is a batch process. Cold fluid is not added to the system to replace lost vapor. Figure 3.3d shows the receiver efficiencies at different operating temperatures. The lines in Figure 3.3d were obtained by using a heat transfer model of the OAS, which is discussed below.

3.6. Outdoor Generation of Steam

An outdoor experiment using natural sunlight validated the ability of the OAS to generate steam in real conditions, where factors such as varying incident solar flux and wind can greatly hinder receiver performance. The OAS was placed on the roof of MIT, at noontime for all experiments. Thermocouples were used to measure the selective absorber temperature, and a thermal pyranometer used to measure the incident solar flux on a horizontal surface, known as the global horizontal irradiance. Figure 3.4 shows the selective absorber temperatures and solar fluxes during the two experimental runs (August 6 and September 17, 2015). Based on the lab data, when the selective absorber reaches 100 °C, steam is generated.

Figure 3.4a shows a measurement on a sunny day with roaming cloud cover, which caused the solar flux to vary dramatically (~200-1000 W/m^2). The temperature measurements show that the selective absorber is capable of recovering its peak operating temperature (>95°C) within minutes. Figure 3.4b shows a situation where the sun is more constant, but at a lower position in the sky due to seasonal variation. This lower sky position reduces the amount of solar flux incident on a horizontal surface (~750 W/m^2). These experiments demonstrate the ability of the solar receiver to rapidly reach 100°C temperatures during periods of low and varying solar flux, such as during non-summer months and cloudy days.

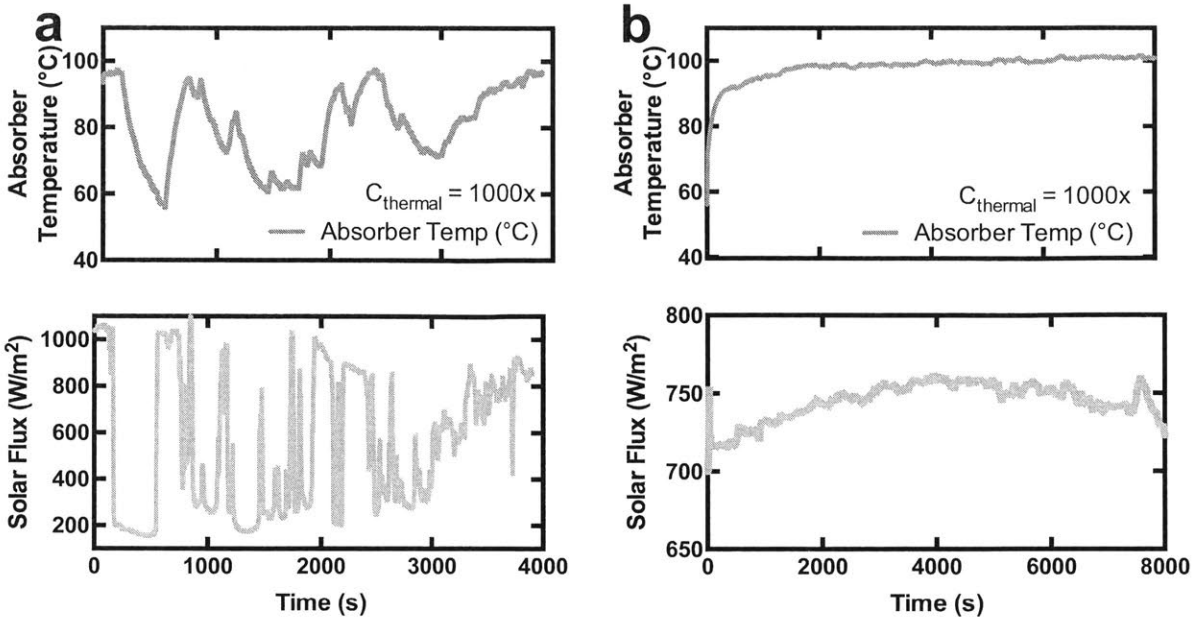

Figure 3.4|Outdoor performance under natural sunlight. Temperature measurements of the OAS in outdoor conditions on two separate dates: (a) August 6th, 2015, and (b) September 17, 2015. a demonstrates the OAS' ability to rapidly reach peak operating temperature on cloudy days, whereas b demonstrates its ability to generate steam during low solar flux days (non-summer seasons).

3.7. Heat Transfer Modeling of a Non-Concentrating Solar Steam Generator

We carried out modeling to gain insights into the current experiment and future performance (Section 3.10). A key requirement for efficient thermal concentration is limiting the temperature drop along the surface of the selective absorber. A large temperature drop reduces efficiency, and indicates significant heat loss compared to the heat conduction to the evaporation region. We used a simple fin model to justify that the temperature throughout the selective absorber is nearly uniform, consistent with our measurements. We incorporate this isothermal assumption into the Isothermal Model. We also carried out COMSOL simulations to determine the sidewall losses in the lab-scale experimental OAS. The results are plotted in Figure 3.3d.

The Isothermal Model is used to predict the achievable performance of a large-scale OAS where the side wall heat loss is negligible. Such a large-scale OAS is expected to have repeating

patterns of evaporation slots, thus maintaining the isothermal absorber. Figure 3.5a shows the achievable vapor temperatures and efficiencies predicted while under 1000 W/m^2 illumination. The maximum temperature reached was 100°C with a thermal concentration around 200x. The thermal concentration required to generate steam is higher than the optical concentration reported in previous experiments,[28,29] but is significantly easier to implement. Higher thermal concentration yielded lower evaporation efficiency, due to reduced evaporation area. However, once the steam generation temperature has been reached (100°C), increasing thermal concentration does not change the efficiency much, due to phase change limiting any further temperature rise. Theoretically, superheating may occur at higher thermal concentrations, leading to increased heat losses and lower efficiency. These scenarios are not included in the model, as they are not observed in the thermal concentrations tested in this study. At low thermal concentration with large evaporation area, the efficiency of the system is higher, but the vapor temperature generated is low due to the higher evaporation rates. Based on the results of our modeling, two useful receiver configurations were identified: one for high-temperature (100°C) vapor generation, and another for high-efficiency evaporation (C_{therm} = 1x).

Figure 3.5b shows the predicted performance of the OAS at different solar fluxes (obtained by using the model in Section 3.10, coefficients in Section 3.11) at C_{therm}=1x and C_{therm}=1000x. This illustrates the ability of the OAS to generate steam throughout the day, when the sun is at different positions in the sky. The temperature plateau indicates phase change limiting the temperature rise of the OAS, consistent with measurements. Figure 3.5c shows a sensitivity analysis of the OAS' maximum operating temperature to the transmittance of the bubblewrap and absorptance of the selective surface ($\tau_{bubble}\alpha$). The thermal concentration was set to 1000x. The receiver can generate steam with $\tau_{bubble}\alpha > \sim 0.4$, with increasing efficiency at higher $\tau_{bubble}\alpha$. At lower $\tau_{bubble}\alpha$ the receiver is generating vapor via evaporation. Figure 3.5d shows sensitivity of the maximum operating temperature to the receiver emittance. It reveals that the OAS can generate steam even if the selective solar absorber has significantly poorer optical properties than the one used in our system. This suggests that the most expensive component, the selective absorber, can be made more cheaply than what was used in this paper.

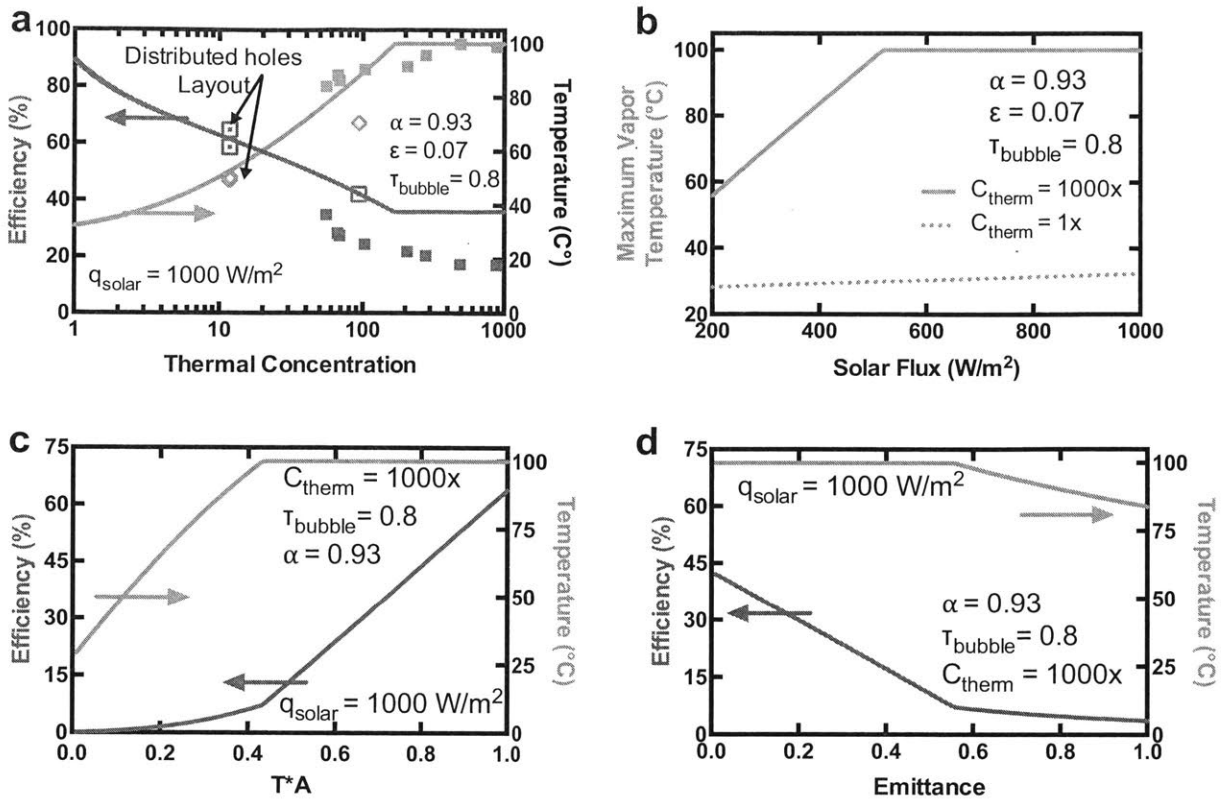

Figure 3.5|Analysis of a large-scale OAS' performance (a) The achievable performance of the receiver using an isothermal absorber approximation (see Supporting Information). The open data points indicate the measured performance of a high-efficiency version of the OAS with distributed holes. The lines represent the predicted achievable performance of a large OAS with negligible side losses. (b) Performance at various solar fluxes for low and high thermal concentrations. (c) Sensitivity of efficiency and maximum temperature to the product of bubble wrap transmittance and selective surface absorptance. Thermal concentration is 1000x. (d) Sensitivity of the receiver to emittance ε, which affects radiative losses. Transmittance and absorptance have a larger effect on efficiency than emittance. Absorbers with significantly poorer optical properties than our selective surface can be used to generate steam, suggesting cheaper material substitutions in future designs.

3.8. Evaporation Slot Design

Another area for optimization of the receiver is the evaporation slot design. Understanding the dominating resistances in the evaporation process can give us key insights into how to improve

the design. Using Schrage's model,[39] an upper limit for evaporative heat transfer coefficient is estimated to be on the order of 10^7 W/m^{2}K (Section 3.11). This is 5 orders of magnitude higher than the coefficients measured in this work (~500 W/m^{2}K, Section 3.16). This suggests that the overall evaporation rate is limited by vapor diffusion through air, not vapor formation at the liquid-air interface. In support of this conclusion, the evaporation heat transfer coefficient increased ~10x over those in a previous work[28], likely due to the difference in the system geometry. The system in Ref. 26 had an evaporation surface with a large planar area, resulting in 1D vapor diffusion away from the liquid. In contrast, OAS evaporation areas are better approximated by lines, enabling 2D vapor diffusion, and resulting in larger evaporation heat transfer coefficients. Additional evaporation experiments were conducted to determine the size effect of evaporation areas. Smaller circular evaporation areas improved the per area evaporation rate dramatically, up to 10x increase for a 36x reduction in area (Section 3.16). Further analysis using COMSOL determined that closely space evaporation areas improved efficiency (Section 3.13).

Even though the current single slot configuration has a higher mass transfer coefficient than Ref. 26, the mass flux is much smaller due to reduced area of evaporation. One way to improve evaporation efficiency is to distribute numerous smaller circular slots for 3D vapor diffusion, while preserving the thermal concentration ratio for the overall area. This strategy maximizes the volume of air for vapor diffusion per distributed circular slot, enhancing the overall evaporation rate. Two additional OAS were created utilizing distributed circular slots, and generated low temperature vapor at much higher efficiencies (Figure 3.5a). The highest efficiency reached was 71% at 12x thermal concentration (64% after subtracting the evaporation under dark conditions). The effective evaporation heat transfer coefficient for the total receiver area was higher than in Ref [137] (29 W/m^{2}K vs 25 W/m^{2}K), and the OAS achieved this with much smaller actual evaporation areas.

3.9. Supplementary Section: Methods

Efficiency Measurement Details

The receiver performance experiments were conducted in the lab using a solar simulator (ScienceTech, SS-1.6K) outputting simulated solar flux at 1000 W/m^2 (1 sun). The solar flux

was measured using a thermopile (Newport, 818P-001-12) connected to a power meter (Newport, 1918-C). Because the solar flux varies across the beamspot, and the thermopile detector is smaller in area than the solar receiver, the maximum-measured solar flux is regarded as the actual constant solar flux for the efficiency measurements. In actuality, the rest of the solar receiver was receiving less than this maximum measured solar flux. This under-reports the vapor generation efficiency by up to 5%, based on the variation observed in solar flux. A 10cm aperture is used to minimize the amount of extraneous solar flux striking the receiver. The mass of the water loss is measured using a lab balance with 1 mg resolution (A&D, FX300i), and calibrated to weights heavier than the total weight of the OAS. Before illuminating the OAS, the evaporation in dark conditions was measured for 10 minutes. The dark condition-evaporation rate was subtracted from the solar-illuminated evaporation rate. Both evaporation rates were measured for 30 minutes at steady-state conditions.

The temperatures of the selective absorbers were measured by attaching thermocouples (Omega Engineering, 5TC-TT-K-40-36) to the copper substrate. Thermocouples were placed at the edge of the selective absorber, and in the center, adjacent to the evaporation slot. The temperature variation observed was <1°C, showing the selective absorber had nearly uniform temperature. The vapor temperature was measured by dipping a thermocouple into the evaporation fabric. The vapor temperature thermocouple was aligned vertically, to minimize errors caused by absorption of the solar flux. These errors were measured to be <1°C.

For the measurement of the 98°C steam in Figure 3b of the main paper, a small vapor chamber was placed around the evaporation slot to trap the vapor. The vapor temperature was directly measured by placing the thermocouple vertically into the vapor chamber, without touching the evaporation cotton. Without the vapor chamber, the vapors dissipated into the cooler surrounding air, and an accurate measurement could not be made without touching the thermocouple to the evaporation cotton.

The rooftop measurements were conducted using a Hukseflux LP-02 thermal pyranometer to measure the intensity of the sun. Thermocouples (Omega Engineering, K-type, 40 gauge insulated) were used to measure the temperature of the selective absorber.

The bubblewrap was placed directly above the selective absorber, with the bubbles facing down. The amount of condensation on the bubblewrap observed was measured as <1% of the total

vapor generated. In the future, the height of the bubbles could be tuned to optimize the thermal resistance, using natural convection correlations for enclosed spaces.[141,142] Using more transparent plastics for the bubblewrap construction can also further increase efficiency.

selective absorber.

Materials Characterization

The optical properties of the receiver materials were measured using an Agilent UV-Vis spectrophotometer (Cary 5000), coupled with an Agilent integrating sphere.

BlueTec provided the selective absorber (cermet-coated copper). The solar absorptance was determined by weighting the wavelength-dependent absorptance with the AM 1.5G solar spectrum. The sample was non-transmitting, so absorptance was calculated as unity minus reflectance. The emittance was determined by weighting the reflectance with the blackbody emission spectrum at 100°C.

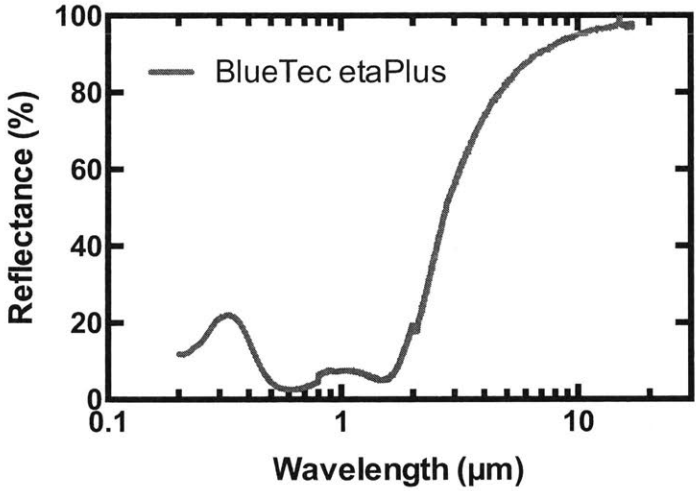

Figure 3.6: BlueTec etaplus solar selective absorber reflectance, measured with an Agilent Cary 5000 UV-vis spectrophotometer and Thermo Nicolet 6700 FTIR. Both devices were equipped with integrating spheres.

The bubblewrap transmittance T was measured using an Agilent Cary 5000 UV-vis spectrophotometer (Figure 3.7). The bubblewrap transmittance T and reflectance R were also measured using an FTIR (Thermo Electron Nicolet 5700), coupled with an integrating sphere

(Pike Technologies Mid-IR IntegratIR). Assuming the absorptance $A = 1 - T - R$, the bubblewrap was found to have negligible absorptance in the mid-IR region, with broadband IR reflectance of ~10%.

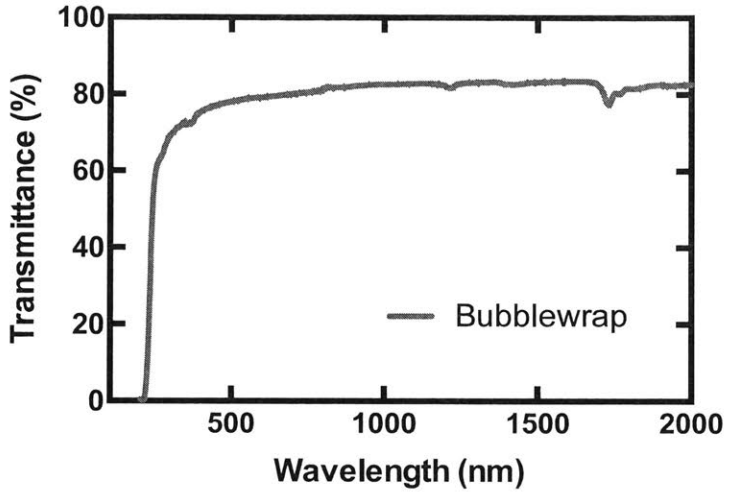

Figure 3.7: Optical transmittance of commercial bubble wrap, measured with an Agilent Cary 5000 UV-vis spectrophotometer.

3.10. Supplementary Section: Isothermal Selective Surface Model

For efficient thermal concentration of solar energy, the temperature drop in the selective absorber should be minimized. Although the OAS has a cylindrical geometry, we can use established theory for heat conduction along a straight fin to estimate the temperature decay along the selective absorber. The temperature decay typically has the form e^{-mx} with the fin parameter m given by

$$m = \sqrt{\frac{h_r + h_{bubble}}{kt}} \tag{3.3}$$

where k is the thermal conductivity along the selective absorber and t the absorber thickness, h_r and h_{bubble} are the radiative and convective/conductive heat transfer coefficients. Using typical values for the experiment, we estimate m is ~3.5m^{-1}, which gives a characteristic length of 0.28m. Since the labscale selective absorber has a radius of 0.05m, we can assume that the selective absorber is of uniform temperature. This assumption is backed up by thermocouple

measurements of the absorber near the evaporation slot and near the edge. The temperature difference is less than 1°C, the accuracy of the thermocouple.

A heat transfer diagram of the isothermal absorber model is shown below in Figure 3.8. This 1D model represents a large-scale receiver where the side-losses are negligible.

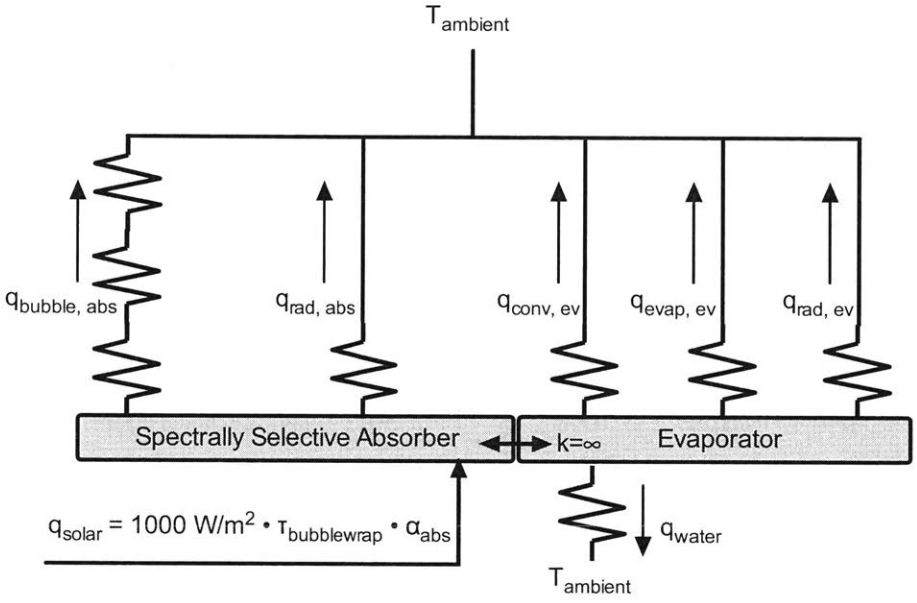

Figure 3.8: Heat transfer diagram of the perfect conduction model. The selective absorber and evaporator are assumed to be isothermal.

q_{conv}, q_{rad}, q_{evap} are the convection, radiation, and evaporation losses, and the subscripts abs and ev refer to the absorber and evaporation slots respectively. q_{water} is the combined conduction and radiative losses to the water underneath. The three resistances in series in the selective absorber region represent the additional resistance caused by the bubblewrap layer, while it is assumed to be transparent for infrared radiation. q_{bubble} is the heat flux through the bubblewrap due to convection and conduction. The energy balance leads to

$$q_{solar}(\tau_{bubble}\alpha_{absorber}f + \alpha_{evap}(1-f)) \tag{3.4}$$
$$= (1-f)(q_{conv,ev} + q_{rad,ev} + q_{evap,ev}) + f(q_{bubble,abs} + q_{rad,abs})$$
$$+ q_{water}$$

where τ_{bubble} is the bubble wrap solar transmittance, f is the fraction of the absorber, $\alpha_{absorber}$ is the solar absorptance of the selective absorber. α_{evap} is the solar absorptance of the evaporation slot, assumed 1. The other heat flux terms in Eq.(3.4) are as follows:

$$q_{conv} = h_{conv}(T - T_{\infty}) \tag{3.5}$$

$$q_{rad,ev} = \varepsilon_{ev}\sigma(T^4 - T_{\infty}^4) \tag{3.6}$$

$$q_{rad,abs} = \varepsilon_{abs}\sigma(T^4 - T_{\infty}^4) \tag{3.7}$$

$$q_{bubble,abs} = [(1 - f_{bubble})h_{conv} + f_{bubble}\left(\frac{1}{h_{conv}} + \frac{1}{h_{conv}} + \frac{1}{h_{conv}}\right)^{-1}](T - T_{\infty}) \tag{3.8}$$

$$q_{water} = \left(\frac{l}{k_{foam}} + h_{r,water}^{-1}\right)^{-1}(T - T_{\infty}) \tag{3.9}$$

h is the heat transfer coefficient, ε is the emittance, σ is the Stefan-Boltzmann constant, T is the temperature of the absorber, and T_{∞} is the ambient temperature. f is the fraction of the receiver surface covered up by the absorber. h_{conv} is assumed to be 10 W/m^{2}K, and $h_{evap}(T)$ was experimentally determined. k_{foam} is the thermal conductivity of the foam (0.03 W/m-K), and l is the thickness of the foam (3cm). h_r is the linearized radiation heat transfer coefficient, which is typically small when emitting into water. f_{bubble} is the fraction of the bubble wrap comprising the individual bubbles (0.9).

The temperature rise of the isothermal absorber model was capped at 100°C, to simulate boiling phase change limiting further temperature rise of the receiver. Negligible superheating of the receiver is assumed, and is confirmed from measurements (Figure 3b of the main paper).

A COMSOL simulation presented in the next section shows that lateral loss accounts for 8% of the total incoming solar energy. This lateral loss was included in the above model in Figure 3.3d.

3.11. Supplementary Section: Evaporation Heat Transfer Coefficient Measurement

The evaporation heat transfer coefficient h_{evap} was determined through a series of experiments using the OAS. The evaporation rate of the solar receiver was measured by measuring the mass loss $\dot{m}$ of the receiver and water supply, while outputting vapor of different temperatures. The vapor temperature was controlled by varying the incident solar simulator flux, and the evaporation area was fixed. Using the evaporation rate (Q_{evap}), evaporation area (A,114 mm^2), and the measured vapor temperature (T_{vapor}), the temperature dependent evaporation heat transfer coefficient (h_{evap}) was measured (Figure 3.9). The laboratory ambient air temperature was 25°C, and h_{fg} is the latent heat of vaporization for water. Equation S7 shows the expression used to determine h_{evap}.

$$h_{evap} = \frac{Q_{evap}}{A(T_{vapor} - T_{\infty})} = \frac{\dot{m}h_{fg}}{A(T_{vapor} - T_{\infty})} \tag{3.10}$$

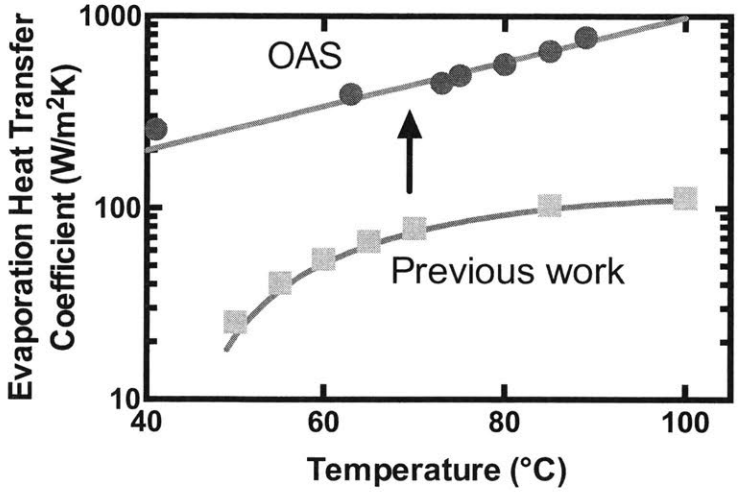

Figure 3.9: Measured and fitted evaporation heat transfer coefficients for both the current device (OAS) and a previous work (Ref. [137]), which is 5-10x lower. In Ref. [137], the evaporation geometry limits diffusion of vapor away more.

The evaporation heat transfer coefficients measured in this chapter's work is compared with those measured in the previous work (Ref [137]). A 5-10x increase is seen in this work's (OAS)

evaporation heat transfer coefficient, likely due to a more favorable evaporation geometry for diffusing the generated vapor away. The evaporation heat transfer coefficients from Ref [137] are determined using the reported solar fluxes and efficiencies.

3.12. Supplementary Section: COMSOL Simulation

A COMSOL model was created to help characterize the sidewall losses of the lab-scale solar receiver. In Figure 3.10, the top cylinder represents the solar receiver, which is floating on the bottom cylinder of water.

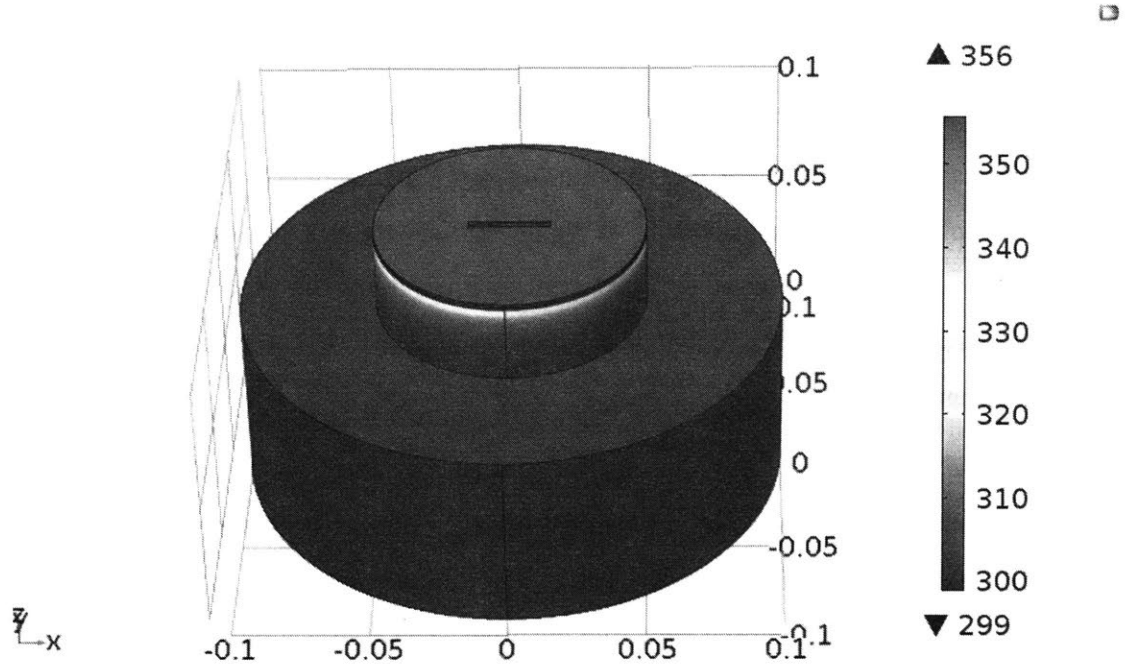

Figure 3.10: COMSOL model of the labscale solar receiver. The side losses of the labscale receiver can be estimated, and allow comparison of the lab experiments with modeling of a large scale receiver.

The solar receiver simulated had an evaporation slot of 90 mm^2, which translated into a thermal concentration of 100x. To calculate the heat losses, we used the same heat transfer coefficients as in the Isothermal Selective Absorber Model described above. A convective and radiative heat flux was applied to the absorber and evaporation slot. The evaporation slot had an additional evaporation heat flux, using the measured evaporation heat transfer coefficients. The solar flux incident on the top absorber is 744 W/m^2, and accounts for the bubblewrap transmittance and

absorber absorptance. A convective heat flux with heat transfer coefficient of 10 W/m^2K was applied over the sides of the receiver. Radiative losses were applied to all surfaces of the model, with the selective absorber emittance = 0.07, and evaporation slot emittance = 1. All other emittances were assumed to be 1.

From the COMSOL model we determined: 1) the side convective losses to be ~8%, 2) the conduction losses to the underlying water to be ~3%, 3) the radiative losses at the top to be ~5%, 4) the convective losses through the bubble wrap to be ~24%, and 4) the evaporation flux to be ~36% of the total incoming solar energy. The remaining amount of incoming solar energy is reflected away due to the bubble wrap and absorber reflectance.

3.13. Supplementary Section: COMSOL Fin Model

In large-scale applications, the receiver may have a repeating arrangement of evaporation slots, separated by multiple selective absorbers. With larger separation distances between the evaporation slots, the selective absorber will lose heat as it conducts the absorbed energy to the evaporation slots. Thus, the separation distance must be optimized to balance manufacturing cost and receiver performance.

An additional COMSOL model was created to understand the effect of finite thermal conductivity on larger absorber areas. In this model, a large receiver with repeating patterns of selective absorbers and evaporation slots was assumed. A single unit of this pattern consisted of an evaporating slot, and the surrounding selective absorber. The analysis occurred in 2D, in the y- and z- directions in Figure 3.11.

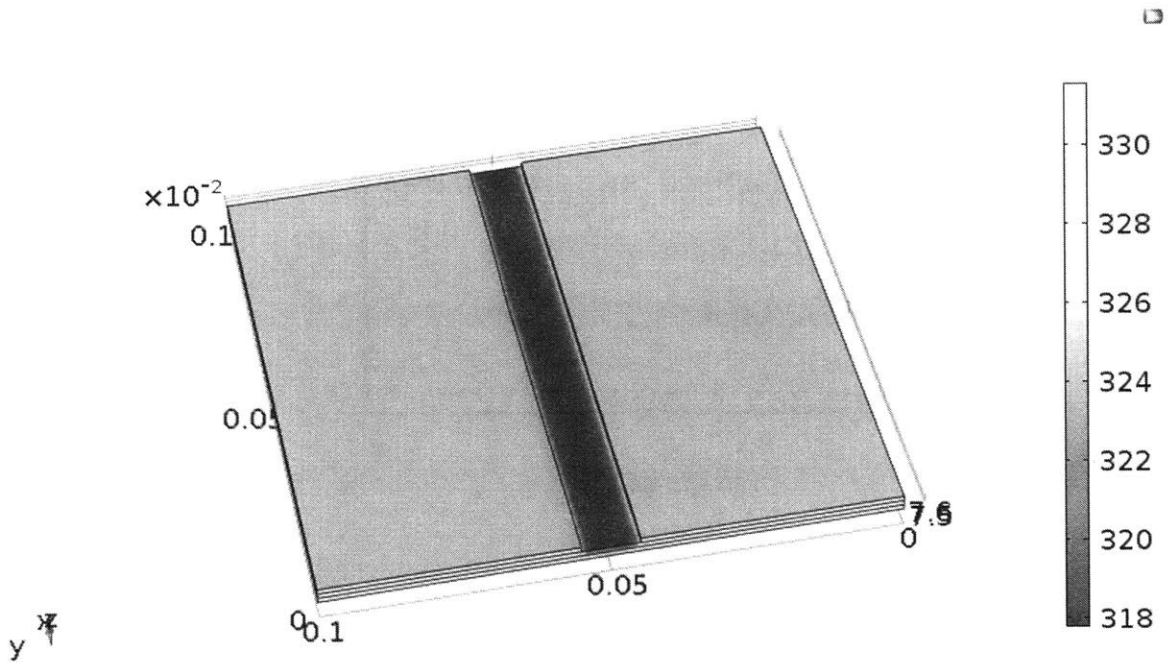

Figure 3.11: COMSOL fin model to analyze the effect of absorber size on evaporation efficiency. The thermal concentration was fixed at 10x.

In this model, the same heat loss mechanisms (bubblewrap heat transfer coefficient = 4.33 W/m^2K, radiative loss from selective absorber with emittance = 0.07) were used as in the Isothermal Absorber model. The conduction to the underlying water was considered negligible, as the foam thickness could be increased. However, we added a finite thermal conductivity for copper (400 W/m-K) and water (0.63 W/m-K) in the y-direction, and then varied the length of the receiver in the y-axis while keeping the thermal concentration constant. In the x-direction, the receiver is considered long with periodic boundaries. The results are plotted below in Figure 3.12.

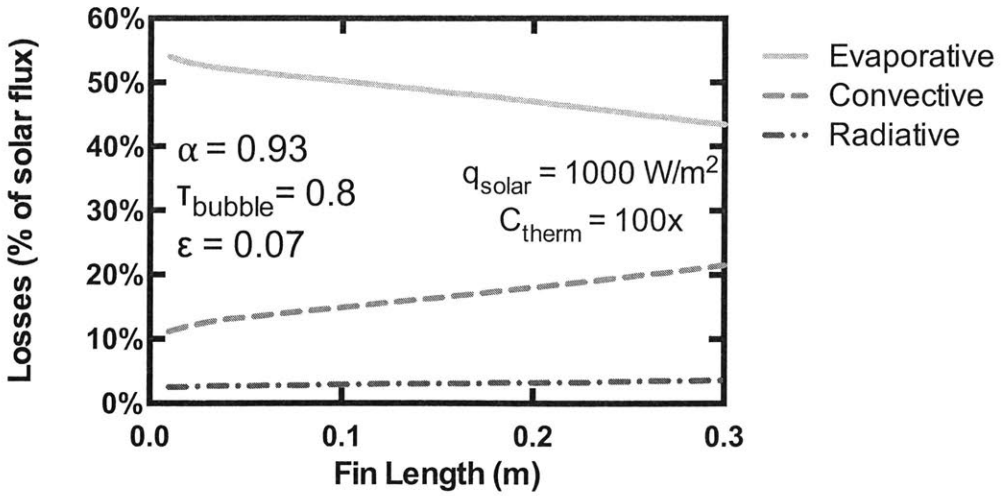

Figure 3.12: Performance of the receiver as a function of the fin length. Longer fins conduct heat to the evaporation slots less efficiently, losing more heat to radiation and convection to the environment.

3.14. Supplementary Section: OAS Cost Analysis

Here, the bill of materials is estimated for a commercialized 1 m^2 OAS receiver using bulk pricing available online. The selective absorber will be composed of a selective coating made by Solec, for approximately \$0.5/m^2, and an aluminum plate (\$5/m^2 at 1mm thick, which is a conservative thickness estimate) to substitute for the copper plate used in this chapter's research. The lower thermal conductivity of aluminum (200 W/m^2) can be countered by distributing the evaporation slots, using the strategy outlined in section S10. We anticipate using methods to bond bubble wrap to the underlying aluminum, such as heat pressing or using simple glue. The thermal foam is approximately \$0.5-\$1/m^2, and the bubblewrap is \$0.05/m^2. This gives a total materials cost of \$6/m^2 for the thermal concentration approach used by the OAS. The manufacturing processes needed are anticipated to be roll-to-roll processes, such as hole punching of the slots as well as heat pressing to seal the bubble wrap and the selective absorber. Many of these processes are already employed in making commercial bubble wrap, which is low cost (~\$0.05/m^2). This indicates the OAS to be relatively cheap to manufacture. Considering a steam generation efficiency of 30%, the thermal concentration approach to steam generation is 20x cheaper than the optical concentration approach. Polymer films and bubblewraps currently

sold in the agricultural industry for use in greenhouses offer high optical transparency and are typically warranted against UV degradation for 3-10 years[4,5].

The optical concentration approach is calculated at $200/m^2 for the cost of the concentrators, and the receiver is neglected in this case. A typical optical concentration efficiency of 70% is applied to the reported values of steam generation (80-87%) to give ~60% total steam generation efficiency using the optical approach.

3.15. Supplementary Section: Solar Absorption Comparison Between Optical and Thermal Concentration

Optical and thermal concentrators have several key differences that affect their usage. Optical concentrators generally require tracking of the sun, and can collect only the direct component of sunlight, also known as the Direct Normal Irradiance (DNI). For thermal concentration, solar tracking and flat panel deployment are both available options. In flat panel deployment, both the direct and diffuse components (Global Horizontal Irradiance, GHI) of sunlight can be captured. However, viewfactor losses are incurred as the sun moves through the sky.

One way to compare total steam generated using either concentration methods is by looking at available sunlight. GHI and DNI can be used to compare respectively the total solar energy incident on a horizontal surface, and the direct component of sunlight captured by a tracking optical concentrator. For many areas in the US, GHI is slightly higher than DNI. In Boston MA, the annual GHI is 3.9 kWh/m^2/day, and the annual DNI with 2-axis tracking is 3.7 kWh/m^2/day (Figure 3.13a). [6] This is due to tracking optical concentrators being unable to collect the diffuse component of the solar flux, despite having less viewfactor losses.

Seasonally, there will be variation in GHI and DNI. In the Winter, tracking optical concentrators will be more effective than a flat panel thermal concentrator, due to the lower position of the sun (Figure 3.13b). However, on cloudy or summer days, the thermal concentrator will be far superior, due to the high diffuse component of the solar flux (Figure 3.13c).

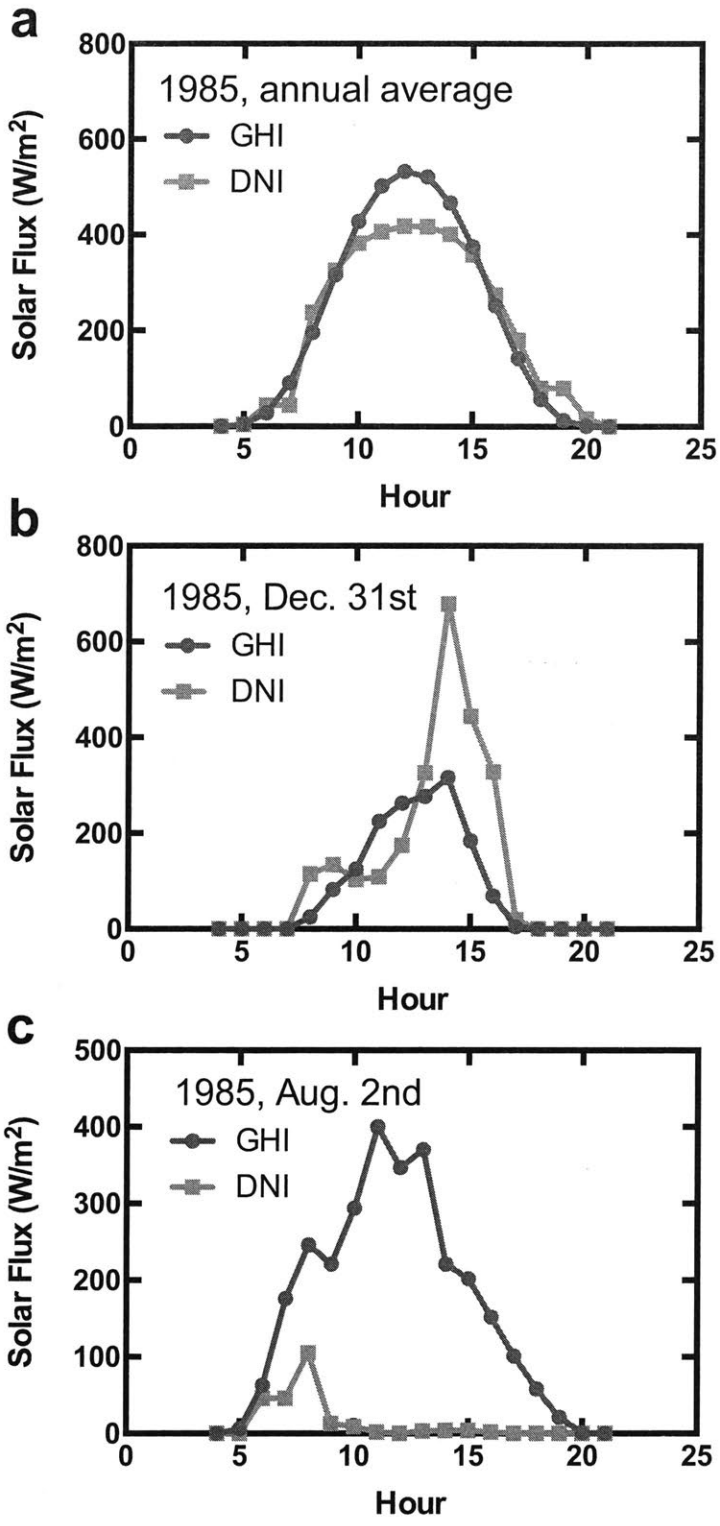
a
1985, annual average
GHI
DNI
Solar Flux (W/m²)
Hour
b
1985, Dec. 31st
GHI
DNI
Solar Flux (W/m²)
Hour
c
1985, Aug. 2nd
GHI
DNI
Solar Flux (W/m²)
Hour

Figure 3.13: Various hourly solar data for the year 1985 (year chosen randomly). a) shows the annually averaged hourly data. b) shows the solar flux on a winter day, where tracking is more useful. c) shows the solar flux on a cloudy day, where optical concentrators are not so useful.

3.16. Supplementary Section: Evaporation Mechanisms

An area for optimization of the receiver is the evaporation slot design. Understanding the dominating resistances in the evaporation process can give us key insights into how to improve the design. In this system, vapor generation occurs first at the liquid-air interface. Then, the vapor must diffuse through the surrounding air to the ambient environment. The interfacial mass flux between pure water and its vapor phase can be calculated using Schrage's mass flux Eq.(3.11):

$$\dot{m} = \frac{2a}{2-a}\sqrt{\frac{M_l}{2\pi R}}\left(\frac{P_{v,li}}{\sqrt{T_{li}}} - \frac{P_{v,vi}}{\sqrt{T_{vi}}}\right) \tag{3.11}$$

where a is the evaporation accommodation coefficient (~1), M_l is the molar weight of water (18 g/mol), R is the universal gas constant, $P_{v,li}$ and $T_{v,li}$ are the saturated vapor and temperature of the liquid at the liquid-air interface, and $P_{v,vi}$ and $T_{v,vi}$ are the saturated vapor and temperatures of the air at the liquid-air interface. The heat transfer coefficient for the interfacial mass flux can be similarly defined:

$$h_{evap} = \frac{q}{\Delta T} = \frac{h_{fg}}{T_{li} - T_{vi}}\frac{2a}{2-a}\sqrt{\frac{M_l}{2\pi R}}\left(\frac{P_{v,li}}{\sqrt{T_{li}}} - \frac{P_{v,vi}}{\sqrt{T_{vi}}}\right) \tag{3.12}$$

where h_{evap} is the evaporation heat transfer coefficient, and h_{fg} is the latent heat of vaporization. For water, with a temperature difference of 1°C at a liquid temperature of 100°C, the heat transfer coefficient is on the order of 10^7 W/m^{2}K. This is 5 orders of magnitude higher than the

evaporation heat transfer coefficients measured in this chapter's work (~500 W/m^2K, see Supporting Information). This suggests that the overall evaporation rate is limited by vapor diffusion through air, not vapor formation at the liquid-air interface. This theory is supported by comparing the measured evaporation heat transfer coefficients in a previous work[137] (20-100 W/m^2K) and those in the current experiment (400-1000 W/m^2K). A ~10 times increase in evaporation heat transfer coefficients of this chapter's work compared to Ref. 26[137] is due to the difference in the system geometry between our previous work and current work. A comparison of the two sets of evaporation heat transfer coefficients is shown in Section 3.11. The system in Ref. 26 had an evaporation surface with a large planar area, resulting in 1D vapor diffusion away from the liquid. In contrast, OAS evaporation areas are better approximated by lines, enabling 2D vapor diffusion, and resulting in larger evaporation heat transfer coefficients.

The dependence of evaporation heat transfer coefficient on the area of evaporation further supports diffusion resistance of vapor away from the liquid-vapor interface as the dominant resistance. Manipulation of this diffusion resistance can potentially allow for higher efficiency vapor generation in applications where vapor temperature is not important. To further understand and quantify this size dependence, the evaporation rate per area was experimentally measured for various evaporation surface areas. These evaporation surfaces were created using the cotton fabric used in the OAS, and shaped as circles with diameters from 4mm to 24mm. The evaporation heat transfer coefficients were measured using the methodology in Section 3.11, and Eq.(3.10). Figure 3.14 shows the results of the study. As expected, smaller evaporation areas have higher per-area evaporation heat transfer coefficients.

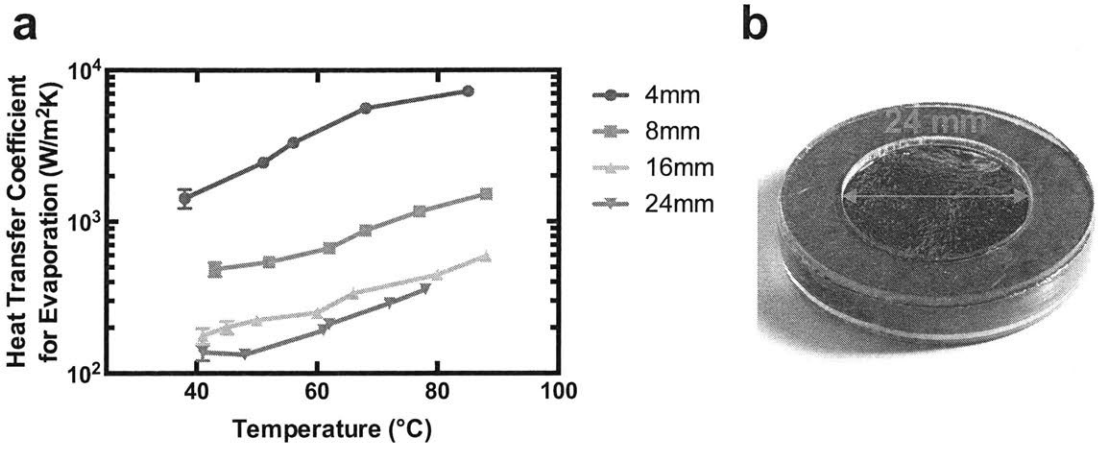

Figure 3.14: Diameter dependence of evaporation heat transfer coefficient for various sized evaporation areas (4-24mm in diameter). Clearly, for smaller areas, the evaporation heat transfer coefficient increases drastically, taking advantage of the better vapor diffusion geometries. b) Evaporation heat transfer coefficient studies were carried out using small containers filled with water. The aperture allowing evaporation was laser-cut, ensuring good precision. A cotton fabric wicked water to ensure good water-air contact for evaporation.

3.17. Outlook and Summary

Demonstration of continuous direct steam generation under the one sun condition opens many potential applications, such as distillation and sterilization in remote locations. By pressurizing the system, one can potentially use the approach to generate superheated steam - for power conversion using water or other organic working fluids. The floating structure also has potential for solar desalination when the generated vapor is collected. Solar stills have been used for thousands of years, but have remained underutilized due to their low-efficiency (30-45%) and relatively high cost.[40–42] The basic design of the solar still uses a black-bottomed water basin to absorb the incoming solar flux. In such a configuration, radiative losses from the hot water are the largest source of losses, and cannot be avoided. Our approach significantly reduces the radiative loss, as well as the convective losses. There are several examples of floating solar stills in the literature,[43,44] but these are simply basic single-effect solar stills made to float on the ocean. Hence, the cost and efficiency are expected to be similar or worse than conventional solar stills. The OAS can achieve higher efficiencies than an uncovered solar still using alternative

receivers.[45] Furthermore, when placed in a solar still, the OAS' efficiency can be higher, due to better insulation from the environment. In addition, the floating structure will enable direct deployment on water surfaces, such as over a bay, hence reducing system complexity and cost.

We have shown that thermal concentration can be a more cost-effective approach to solar steam generation than optical concentration. The OAS is estimated to cost ~\$6/m^2, based on available bulk pricing of materials, and we expect the cost can be reduced down to ~\$2/m^2. The manufacturing processes for final product are expected to be roll-to-roll, and should be of low cost. The cost of tracking optical concentrators can be as high as \$200/m^2, and much of the prior literature on solar vapor generation has not included the optical losses due to inefficient concentration of the full solar flux, both diffuse and direct. Taking these details into account, the OAS can generate steam at ~5% the cost of optically concentrating approaches (Section 3.14).

Further study in fouling of the OAS is needed, though the decoupling of the optical absorber from the phase change surface is an advantage. The cotton wick is a small fraction of the solar absorber, and its fouling will not affect the solar absorption. Accumulated salt may be sufficiently rejected overnight if used in an ocean. The wick is also easy to replace, being a small component. Overall, the OAS' ability to generate high-temperature steam without relying on bulky and costly concentrating optics opens up many new possibilities for solar thermal energy harvesting.

Chapter 4

4. A Vapor Condensation System for Scalable Solar Desalination

In the previous two chapters, approaches for efficient solar evaporation are discussed. Despite the high evaporation efficiencies (~80-90%) achieved by the community through solar heat localization, several unresolved challenges remain. Among these challenges are: (*i*) achieving high operational efficiency in real seawater conditions, (*ii*) maintaining high efficiency in vapor collection, (*iii*) avoiding structure clogging due to salt formation under continuous operation, (*iv*) and reducing the cost of these structures. Downward heat loss from solar evaporation structures was typically underestimated in the literature, since most experiments were performed in beakers in which the convective cooling of waves and currents are not simulated. Therefore, there is an urgent need to study the efficiency of interfacial solar evaporators in real ocean environments. Furthermore, water collection and desalination performance reported for floating evaporation structures remains low (~5%)[143,144], necessitating development of high-performance plastic vapor condensation/collection covers. More importantly, salt build-up remains a significant and poorly studied challenge for floating solar evaporation structures that employ heat localization. Seawater contains 3-3.5 wt% total dissolved solids including NaCl and $CaCO_3$, which are left behind after evaporation. Fundamentally, thermal insulation separates the evaporation interface from saline water sources, and prevents salt from rejecting back into the bulk of the water, leading to clogged structures, ultimately deteriorating structure optical and wicking properties. Hydrophobic surfaces were used to prevent salt from adhering to evaporation structures,[145] however, thermal insulation was sacrificed. Hence, strategies are needed to simultaneously reject salt and thermally insulate the floating structure.

Here, we present a new approach to address fundamental challenges of salt rejection in solar evaporation for desalination. We demonstrate a floating multi-layer solar evaporation structure that rejects excess salts while preserving heat localization. In particular, salt rejection experiments revealed a strong resistance to fouling from NaCl, the most prevalent salt in ocean water. This work has ultimately yielded a low-cost floating solar still, made from commercially

available materials that is capable of producing drinkable water continuously in saline waters, without the need for periodic cleaning. The solar still can produce water at 2.8 $Lm^{-2}day^{-1}$, or a daily-averaged solar-to-water efficiency of 24%, enough to satisfy daily individual drinking needs. In addition, the traditional glass and steel solar still was replaced with a fully polymeric lightweight design expected to cost ~\$3 m^{-2}, and 10-100 times lower than current solar still system. Water collection tests were conducted both in a controlled rooftop setup and in the ocean. A heat transfer model of the solar still was also developed to identify areas for improvement. We believe this improved floating solar still design, capable of simultaneously rejecting salt and localizing heat, has the potential to significantly expand access to affordable clean water for off-grid communities, thus addressing one of the most pressing challenges in the water-energy nexus.

4.1. Solar Evaporation Structure and Design

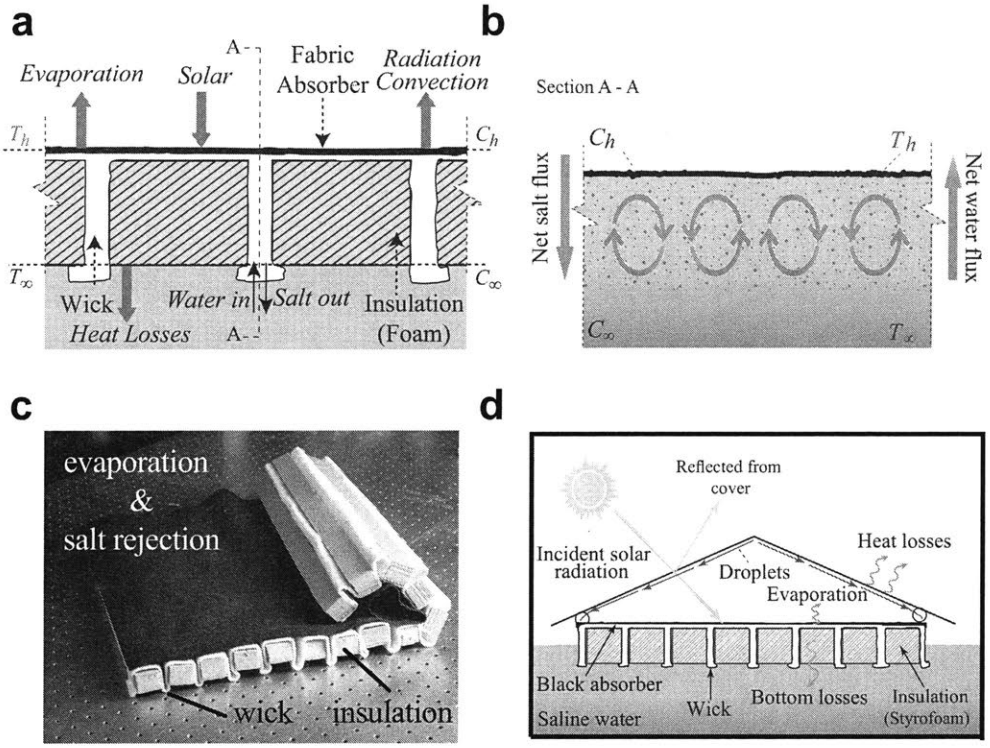

Figure 4.1: An evaporation structure with simultaneous salt rejection and heat localization ability. a) shows the evaporation structure's design, with a black fabric for solar absorption, and a composite white fabric wick and polystyrene foam insulation. The wick both delivers water for evaporation, and rejects excess salt. b) shows the advection flow of salt rejection due to denser, salter water at the evaporation surface. c) Photograph of the evaporation structure. d) Schematic

of the evaporation structure in a fabricated polymer-film based condensation cover operating in an ocean.

Figure 4.1 shows the salt-rejection evaporation structure designed to float on saline bodies of water, absorb and convert incident solar flux (nominally 1 kWm^{-2}, 250-2500 nm) into thermal energy, and transfer this heat to water for vapor generation, while rejecting excess salts to the water underneath. The evaporation structure is composed of multiple layers. The top layer is a solar flux absorbing layer of hydrophilic black cellulose fabric (Zorb®), which also wicks up water. Heating only a restricted layer of water enhances evaporation.

Beneath the black fabric is an insulating structure that serves to simultaneously thermally insulate the evaporation layer and to reject excess salts back to the water below. The insulating structure is made from alternating layers of expanded polystyrene foam and white cellulose fabric (Zorb®). The expanded polystyrene has low thermal conductivity (~0.02 $Wm^{-1}K^{-1}$), and limits thermal conduction of heat down from the evaporation surface above. The white fabric is porous and hydrophilic, allowing it to wick water to the solar-absorbing evaporation structure above, while advecting and diffusing concentrated salt down back into the body of water (Figure 4.1b). The evaporation structure (Figure 4.1c) is designed to operate with a condensation cover to collect the produced vapor (Figure 4.1d).

Material selection is important to balance competing thermal and salt rejecting properties needed. The expanded polystyrene is thermally insulating, but impermeable to water, whereas the fabric wick is permeable to water. However, water itself leaks heat, having thermal conductivity 30x higher than foam (0.58 vs 0.02 $Wm^{-1}K^{-1}$). As such, the fabric wick and expanded polystyrene used in the insulation structure have competing thermal and salt rejecting properties, and the area ratio of fabric wick to expanded polystyrene must be optimized to reject salt while maintaining efficient insulation. In addition, different time-scales for salt rejection and thermal insulation must be accounted for. Salt is rejected over 24 hours, while thermal insulation is only needed during daylight hours.

Salt rejection can occur via two modes, diffusion and advection, down the fabric wick. Each mode of mass transport is coupled with a respective mode of heat loss. For example, when salt diffuses through still water, heat also diffuses. Examples of advection salt rejection include free convection of denser high-concentration salt water at the evaporation surface, or periodic

washing of the evaporation surface with ocean currents. For this chapter, the fabric wick area was chosen to be 20% of the total insulation structure area, leaving 80% remaining area for expanded polystyrene. This area ratio was based on conservative estimates of diffusion-based salt rejection through the wick (Supplementary Section 4.7).

4.2. Laboratory Experiments

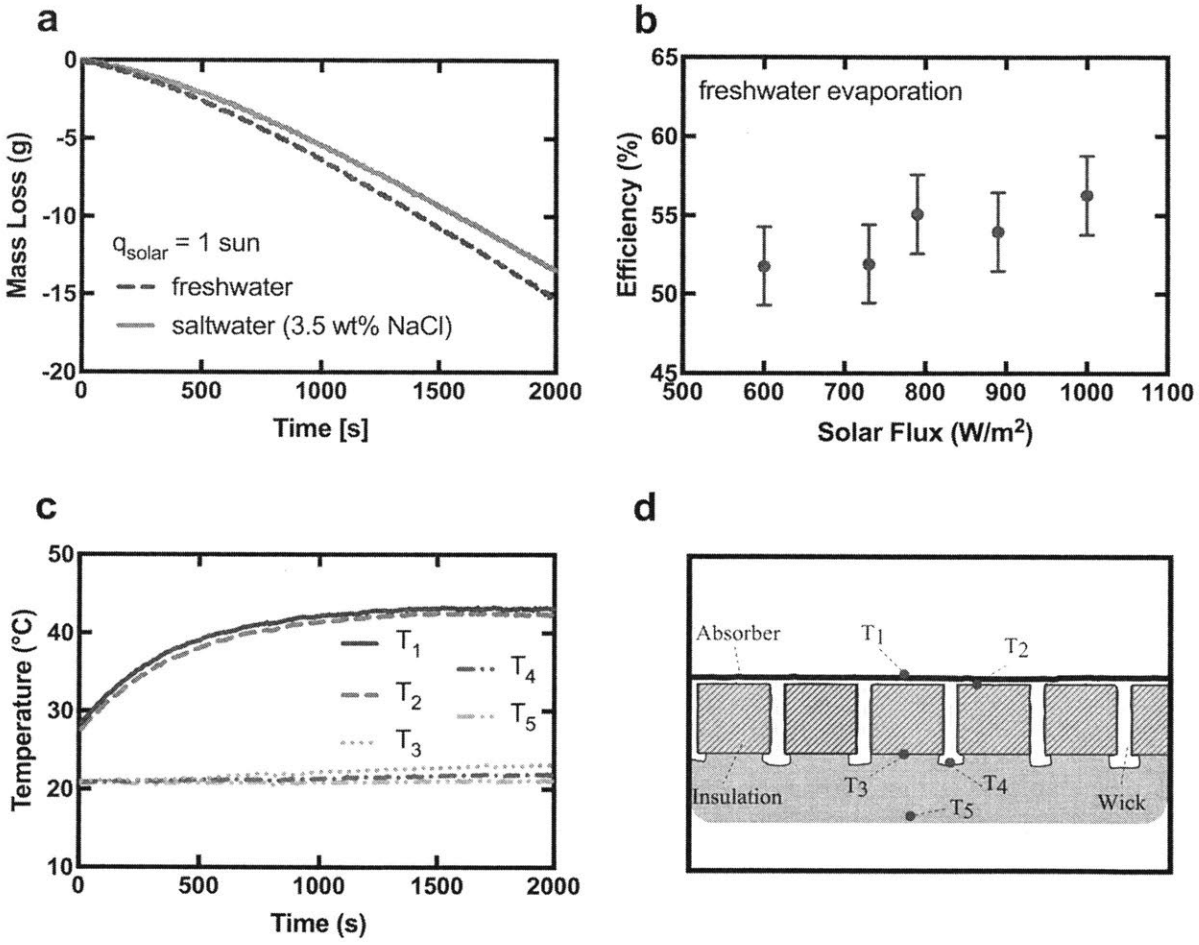

Figure 4.2: Performance of the evaporation structure in solar vapor generation under lab conditions. a) shows the evaporation rate of the evaporation structure in fresh (dashed) and salt water (solid, 3.5 wt% NaCl). b) shows the performance of the evaporation structure in freshwater at different solar fluxes below 1 sun (1kWm^{-2}). There is a slight decrease in efficiency at lower solar fluxes. c) shows the temperatures measured at different locations of the evaporation

structure shown in (d). The large temperature drop from the solar absorbing fabric to the water underneath indicates the insulating ability of the expanded polystyrene.

The solar-vapor performance of a lab-scale evaporation structure (21 cm x 20 cm) was tested in representative laboratory conditions, using both salt and freshwater (details in Supplementary Section 4.6). A solar simulator was used to supply simulated sunlight, and a calibrated power meter to measure incoming radiative flux. The mass of the evaporation structure and water reservoir was continuously monitored using a balance to determine the rate of vapor generation. The efficiency of solar-vapor conversion is defined as:

$$\eta_{vapor} = \frac{\dot{m}_v h_{fg}}{q_{solar}} \tag{4.1}$$

where $\dot{m}_v$ is the mass flux at steady state conditions, h_{fg} is the temperature-dependent latent heat of vaporization of water, q_{solar} is the incoming solar flux, and A_{evap} is the area of the evaporation structure exposed to the incoming solar flux. The sensible heat is neglected because cold water was not piped in to replace generated vapor. To isolate the effects of solar input, the evaporation rate in the dark was subtracted from the measured evaporation rate.

Floating in freshwater and under peak sunlight (1 kWm^{-2}), the evaporation structure can generate vapor at 42°C and 57±4% efficiency. Importantly, when floating in simulated seawater (3.5 wt% NaCl), the evaporation structure generated vapor at comparable efficiencies (56±4%). To understand the evaporation structure performance under variable sunlight conditions, we further measured efficiency at solar intensities ranging from 600 Wm^{-2} to 1000 Wm^{-2} (Fig. 2b). Predictably, the evaporation efficiency reduces slightly (52±4% at 600 Wm^{-2}) with lower sunlight, due to lower evaporation temperatures reached.

Our experiments revealed that the composite wicking-insulation structure succeeded in minimizing heat conduction downward from the liquid-air interface. Figure 2c shows the temperatures recorded at different locations (Fig. 2d) in the evaporation structure. After 4 hours of peak solar illumination (1 kWm^{-2}), the water temperature underneath increased by only 4°C,

due to reduced heat flux through the insulation structure. The heat conduction losses through the insulation structure are calculated to be 110 W m^{-2}, corresponding to an 11% loss relative to the incoming solar energy. Radiative and convective losses from the top of the evaporation structure account for 11% and 9% of peak sunlight, respectively (see Supplementary Section 4.9). The remaining major losses are reflective optical losses of 15% from the wetted black fabric of the evaporation structure (measurement in Supplementary Section 4.11).

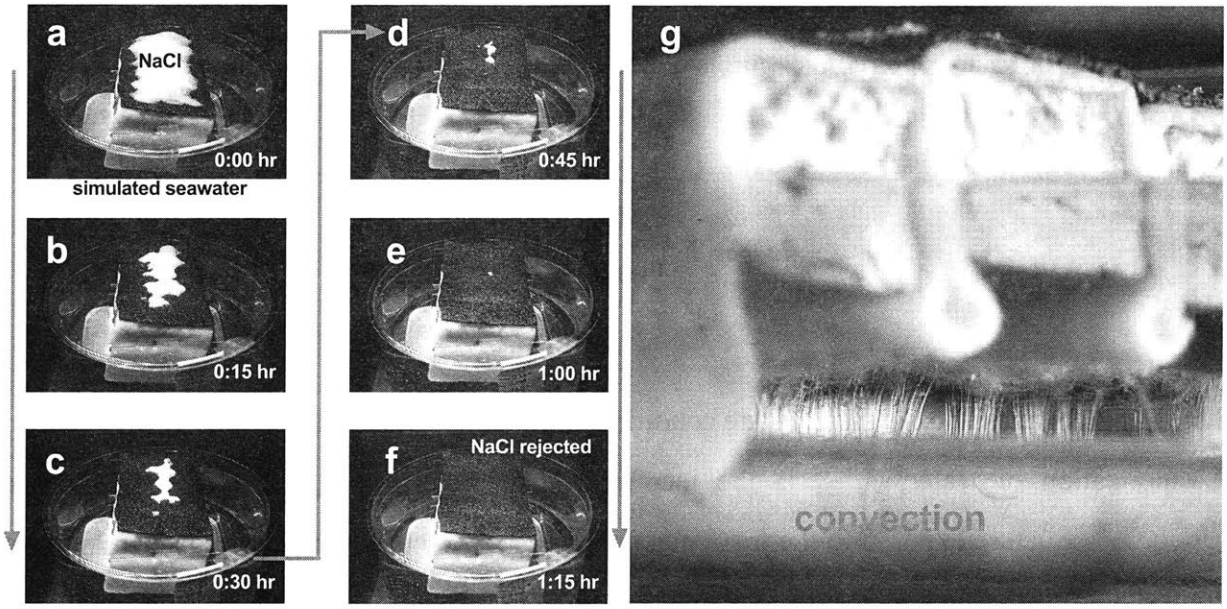

Figure 4.3: a-f) show a progression of salt rejection from the evaporation structure, while under 1 sun illumination. The evaporation structure is placed in a reservoir of 3.5 wt% NaCl, and enough solid NaCl is placed on the evaporation structure to saturate (26 wt%) the structure. This hour-long test displays the ability to reject salt during operation. g) shows a separate test to visualize saltwater rejected by the evaporation structure. Excess salt at the evaporation surface forms a denser solution, which sinks into the water reservoir. Blue dye was added to help visualize the flow, which occurs without the dye as well.

The evaporation structure's salt rejection capability was characterized by several complementary experiments. In the first experiment, we exposed the evaporation structure to simulated sunlight while floating in a 3.5 wt% NaCl simulated seawater reservoir for 7 days (details in Supplementary Section 4.9). Each day, the evaporation structure was exposed to 5 hours of peak sunlight (1 kWm^{-2}), and then allowed to cool and reject salt "overnight". No salt was observed to

form at the end of 7 days, indicating adequate NaCl rejection over extended periods of evaporation. After the seventh day, the structure was illuminated continuously for 30 hours at 1 kWm^{-2} without detectable salt crystal formation.

The second salt rejection experiment demonstrated the evaporation structure's ability to reject salt crystals at steady-state evaporation conditions under 1 sun illumination. The evaporation structure was placed in 3.5 wt% NaCl simulated seawater, and 40 grams of additional solid NaCl, enough to saturate the entire wick structure with 26 wt% NaCl, were placed directly on the evaporation structure. The structure was then illuminated with the solar simulator (1 kWm^{-2}). Despite the extreme amount of salt placed on top, the evaporation structure fully rejected the salt after just ~1 hour (Figure 4.3a-f and supplementary video), while generating vapor. After 20 hours of illumination, the NaCl concentration at the wick was found to be 4.2 wt%, using an optical refractometer, indicating salt was rejected and not merely dissolved in the structure (details in the Supplementary Section 4.9). These two salt rejection experiments indicate 1) the evaporation structure can reject salt for several days of solar evaporation, and 2) the evaporation structure can dissolve and reject salt deposits even under constant sunlight.

Our analysis suggests the advection process is the more effective mass transport mechanism. In the Supplementary Section 4.8, we show that a material parameter α_{water}/D_{salt} determines if diffusion or advection gives less heat loss (α_{water} is the thermal diffusivity of water, and D_{salt} is the mass diffusion coefficient of salt in water). Subsequently, a numerical thermo-fluid simulation code was used to model the fluid flow, salt transport and temperature distribution in a single wick (Supplementary Section 4.13). The simulation results confirm that advection dominates the salt rejection process, and that there are counter-rotating two-dimensional advection currents in the salt rejecting wick (Figure 4.1b).

4.3. Condensation Structure

A large condensation cover (55cm x 55cm) was developed to surround the evaporation structure, and capture and condense the solar-generated vapor (Fig 1e). The condensation structure is transparent in the solar spectrum, allowing solar flux to reach the evaporation structure within. The condensed droplets on the cover coalesce and eventually drip into a catch tube. The water

produced is typically very pure (~50ppm).[15] Maximizing collection of all condensed droplets is a major challenge, as not all condensation surfaces are easily collectable.

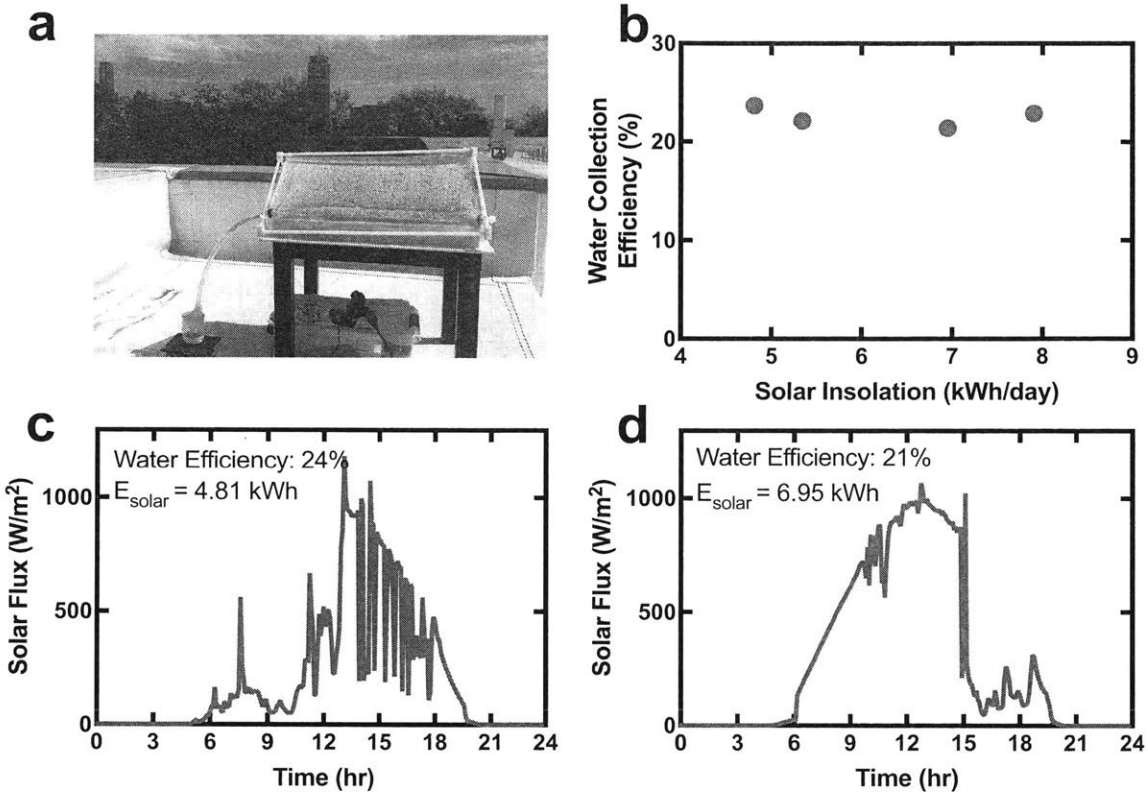

Figure 4.4: Rooftop experiments with the floating solar still under natural sunlight. A shallow basin of freshwater supplied the water. a) Testing location on MIT's roof, in May-June 2017. Liquid water was collected, and the solar flux measured. b) the water collection efficiency of the floating solar still with different solar intensities. The performance of the structure is relatively invariant with solar insolation. c) the solar flux on a partly cloudy day. d) the solar flux on a sunnier day. E_{solar} is the daily solar insolation per m^2.

A large condensation cover (55 cm x 55 cm) was developed to surround the evaporation structure, and capture and condense the solar-generated vapor (Fig. 4a). The condensation structure is transparent in the solar spectrum, allowing solar flux to reach the evaporation structure within. The condensed droplets on the cover coalesce and eventually drip into a catch tube. The water produced is typically very pure (~50 ppm).[146] However, maximizing collection

of all condensed droplets is a major challenge, as not all condensation surfaces are easily collectable.

The large condensation cover (55 cm x 55 cm) was tested in tandem with a large evaporation structure, forming the floating solar still. The floating solar still was deployed in a shallow basin filled with water on the roof of MIT, Cambridge, USA, and water collection was measured over several days during the summer. The condensate was collected in a nearby beaker. The instantaneous vapor temperature, incident sunlight, and ambient wind temperature and humidity were recorded. Here, the collection efficiency is defined as

$$\eta_{water} = \frac{m_{cond} h_{fg}}{A_{still} q_{solar}} \tag{4.2}$$

where η_{water} is the solar-water efficiency, m_{cond} is the mass of condensate collected daily, $q_{solar}(t)$ is the time-dependent solar flux, and the denominator is the total daily solar insolation.

The maximum daily solar-water efficiency measured was 24%, while the maximum condensate collected was 2.81 Lm^{-2} per day. Figure 4.4b shows similar performance between cloudy (Figure 4.4c) and sunny days (Figure 4.4d). The condensate produced from our 0.30 m^2 still is 3.5 times higher compared to a previous work on floating solar stills[144], and is adequate for daily individual drinking needs.

4.4. Ocean Testing

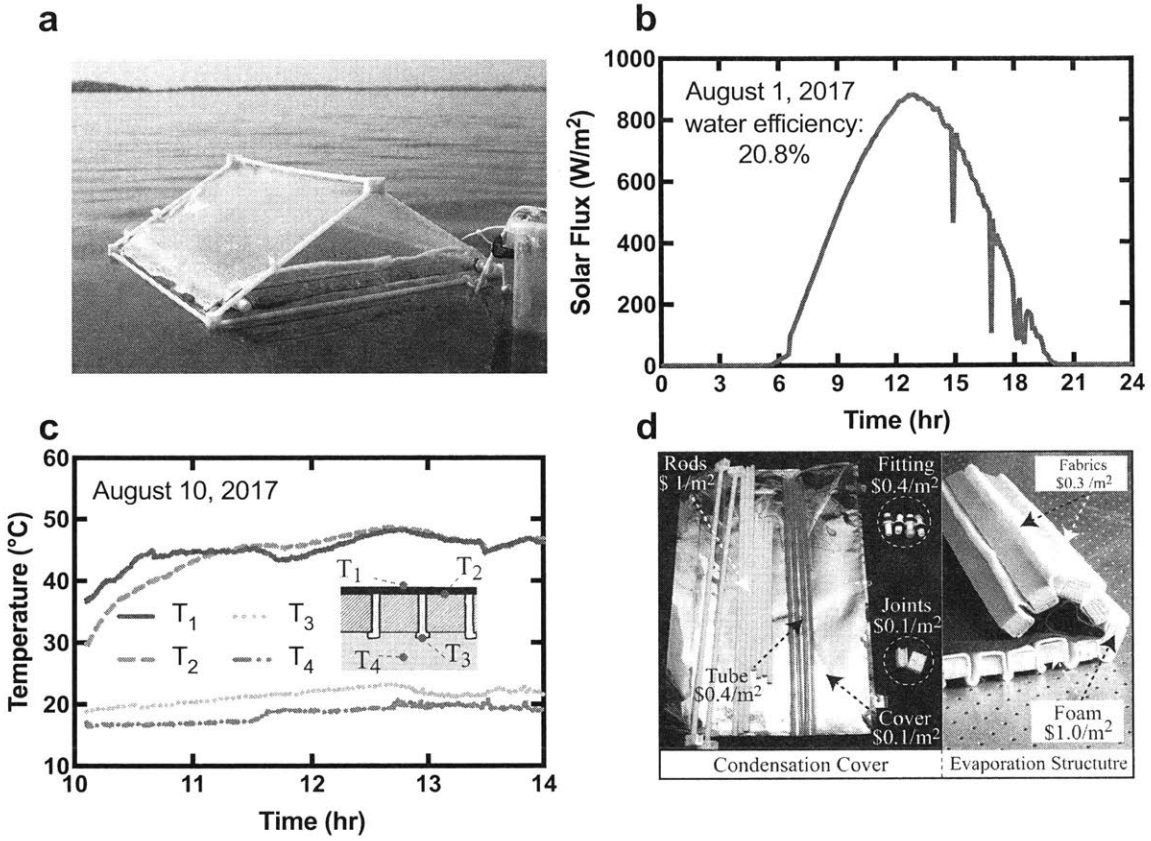

Figure 4.5: Testing the floating solar still in the ocean (3 wt% NaCl) under natural sunlight. a) Photograph of the solar still in operation at the test location Pleasant Bay, MA, on the coast of the Atlantic Ocean. b) The solar flux during measurement. c) The temperature evolution at different locations on the evaporation structure. d) The evaporation structure and condensation cover breakdown of materials. The entire system can be assembled and disassembled by hand, and stored in a compact space.

We also tested the floating solar still in an ocean (Pleasure Bay, Boston, USA) to accurately assess the effect of ocean circulation on heat loss underneath the evaporation structure. The Pleasure Bay test location provides representative conditions of salinity (3 wt% NaCl), tides, and currents. The floating solar still was deployed on the bay from 10:30am to 3:30pm on August 3, 2017 (Figure 4.5a), a representative sunny day (insolation shown in Figure 4.5b). A total of 0.39 L of water was collected, corresponding to a solar-water efficiency of 21%, or 2.5 L m^{-2} day^{-1}. A

system heat transfer model of the entire solar still was developed to analyze sources of heat loss and areas for improvement (details in Supplementary Section 4.9).

Testing in the ocean displayed the floating solar still's effectiveness in limiting heat conduction loss even with cold ocean water underneath. The temperatures of the evaporation structure floating in the ocean (on a different date) are shown in Figure 4.5c. The temperature of the thermal insulation's bottom surface is nearly constant as it exchanges heat with the bulk of the ocean water.

4.5. Discussion

We designed and experimentally demonstrated a new floating solar evaporation structure engineered to simultaneously reject salt while maintaining heat localization for enhanced evaporation. The salt rejection was proven in several lab and ocean experiments. Design guidelines are given to determine whether advection or diffusion should be used in salt rejection, and a thermofluid model was developed to guide future work. A collection cover was developed and paired with the evaporation structure, and freshwater was extracted from various saline waters. Lab-scale and ocean-scale testing was conducted to characterize the performance of the system, resulting in 24% solar-water performance. Coupled with the floating solar still's low cost design (~$\$3 m^{-2}$), and an estimated life-cycle of 2 years, water production cost is $\$1.5\ m^{-3}$. This is 10x lower than conventional solar stills (breakdown in Figure 4.5d and Supplementary Section 4.12). The production cost approaches those of state of the art RO desalination plants, but without requiring high capital expenses and large production capacities.

We believe our evaporation structure and condensation cover have several advantages over conventional solar stills.[147] Although conventional solar stills have annual efficiencies around ~20-40%, they are not widely used due to their high unit cost of production ($15-150 per m^3 water) and the fact they need to be regularly rinsed or cleaned from accumulated salt and other contaminants.[148] Despite a rich history of using heat localization through using porous sponge cubes,[51] floating absorbers,[52,53] isolated evaporation wicks,[54-57] and separate condensation chambers,[58-60] these improvements have increased system complexity and thus water costs. High-efficiency solar stills with evaporation wicks are typically not passively operated, and require use of flow regulators to control the flow rate of water to avoid drying of the wicks

and/or pumps to supply water from the top to cool glass covers and to reuse the latent heat of evaporation.[149] Most importantly, conventional solar stills have not been able to solve the problem of fouling (An extensive review on solar stills can be found in Ref [150]).

There is still ample room for improvement of this technology. Higher collection efficiency can be reached by reducing the optical losses due to droplet formation on the cover. Substituting glass covers with polyester covers in our floating still has resulted in high optical loss (35%), due to the higher contact angle that water makes with hydrophobic polymers. This is in agreement with previous work that revealed that water collection efficiency of solar stills with the glass cover consistently exceeds that of identical stills with plastic covers by over 30%.[151,152] Reduction of the optical transparency due to poor wettability of plastics has also been studied previously in simulations, which show droplet contact angle should be reduced below ~50% to reduce optical losses.[153,154] One strategy may be using hydrophilic transparent polyesters, though the durability of this solution in water must be assessed. Another area for improvement is reduction of the wick area considering the prevalence of advective flow revealed our study. The wick area chosen in this study was based on the conservative assumption of diffusion-based salt rejection, and could be reduced to further minimize backside heat losses. Another area is reducing reflective losses at the fabric absorber (~15%, Supplementary Section 4.11). Other sources of loss include partial collection of all the condensate formed on the cover. In a traditional single-slope solar still, a glass cover tilted at 30° accounts for only 38% of the total condensable surface. In our floating solar still, we collect from 85% of the total condensable area, using a double-sloped design and wicks to collect from the sides. If all of these losses are addressed, our system model predicts 42% solar-water collection efficiency is achievable.

Floating deployment of our system directly on sea, ocean or lake surfaces helps to save agriculturally important land and natural ecosystems from being developed for energy and water production, and eliminates the need for water delivery infrastructure or manual labor. A small individual- or family-size floating still does not require larger community cooperation or external control over fair distribution of distilled water, making it a fast-to-deploy, simple-to-use, and conflict-free technology for disaster relief missions and sparsely-populated areas.

4.6. Supplementary Section: Experimental Details

The floating solar still was designed to be low cost and easily manufactured from widely available materials. The evaporation structure was constructed from cellulose-based fabric (Zorb®), and expanded polystyrene (Owen-Corning Foamular® 150). The condensation structure was constructed from lightweight and cheap polymer films. We evaluated several polymer films, eventually settling on commercial polyester films (McMaster-Carr #8567K32, 0.003" thick). The film was cut into several pieces, and welded together using a heat sealer (McMaster-Carr #2054T35). Droplet collection was facilitated using flaps of polyester film and fabric wicks (Zorb®), as an alternative to typical rubber drip edges and tubes. The polyester film was supported by plastic rods and joints. The wholesale materials cost of the entire floating solar still including evaporation structure and cover is ~ \$3 m^{-2}.

The evaporation structure was tested in the lab using a solar simulator (ScienceTech, SS-1.6K) outputting simulated solar flux at 1000 Wm^{-2} (1 sun). The solar flux was measured using a thermopile (Newport, 818P-040-55) connected to a power meter (Newport, 1918-C). Because the solar flux varies across the beam area, and the thermopile detector is smaller in area than the solar receiver, the solar flux was measured over 5 distributed locations and averaged. The evaporation structure was placed in a polycarbonate basin (21 cm x 22 cm x 3.5 cm), filled with fresh water or saline water. The mass loss of the water was measured using a balance with 0.1 g resolution (A&D, EJ3000). Steady-state evaporation rates were measured for 30 minutes once steady conditions were reached.

The temperatures were measured at five different locations of the evaporation structure shown in Fig. 2d (T_1: at the black absorber, T_2: wick below the absorber, T_3: underneath the thermal insulation, T_4: in the wick bottom of the evaporation structure, and T_5: in the bulk of the liquid) using thermocouples (Omega Engineering, 5TC-TT-K-40-36), and recorded using an Omega Engineering DAQPRO. The absorber temperature was measured by a thermocouple inserted into the evaporation fabric. Thermocouples were placed at the center, to represent the temperature of a sufficiently large absorber where side effects would be negligible. In Fig. 5c, only four different temperatures are measured, with the bottom of the thermal insulation not measured. The temperatures measured are: T_1 at the black absorber, T_2 wick below the absorber, T_3 in the wick bottom of the evaporation structure, and T_4 in the bulk of the liquid

For the day-to-day salt rejection experiments, water with 3.5 wt% NaCl was premixed and placed in the basin, which acted as a salt reservoir. For the week-long salt rejection experiment, the evaporation structure and salt reservoir were exposed to sunlight at 1 kWm^{-2} for 5 hours each day, then allowed to cool and reject salt for 19 hours. The mass of the entire system was monitored to determine the amount of water evaporated. Fresh water was added, as needed to the bottom of the salt reservoir at the beginning of experiment each day, to ensure the reservoir's NaCl concentration remained constant at the start of each day. The evaporation structure surface was photographed daily to monitor the nucleation of NaCl crystals.

The saturation salt rejection experiments were conducted using a glass container with 2.9 L capacity (18 cm in diameter). Water with 3.5 wt% NaCl was premixed and placed in the glass container, which acted as a salt reservoir. A small (14 cm x 7 cm) evaporation structure was used. The small size was chosen to ensure the NaCl rejected to the reservoir wouldn't significantly change the reservoir's NaCl concentration. The area between the structure and the container was covered with a plastic cover. The entire setup was exposed to 1 kWm^{-2} of sunlight, and then 40 g of salt crystals were deposited on top of the evaporation structure. A camera periodically photographed the evaporation structure surface to show salt dissolving and rejecting over the course of a few hours. The salt concentration of the reservoir and evaporation structure top was measured using an optical refractometer with a resolution of 0.1 wt% NaCl (ATC SSA0010). A few drops (3 to 4) of liquid were sucked from the measurement location, and deposited onto the optical window of the refractometer. The final salt concentration in the salt water was 4.6 wt% after the salt rejection experiment.

Rooftop water collection measurements were performed with the large solar still (55 cm x 55 cm). The solar intensity (global horizontal irradiance) was measured using a Hukseflux LP-02 thermal pyranometer. The floating solar still was placed in a shallow basin of water (3 cm deep), placed on a table to avoid conductive heating from the rooftop surface. The floating solar still was oriented with the sloped panels facing south. Water collected from the still was routed via a tube to several sealed beakers. The beakers were emptied 2-3 times throughout the day, and the mass of water collected was recorded. The water collection was recorded through a 24-hour period, starting after sunset when the solar still had equilibrated to ambient temperature.

The ocean experiments were conducted in Pleasure Bay, located in South Boston, MA. The bay is connected to the Atlantic Ocean, and has a salinity of 3 wt%, as measured by the optical refractometer. The temperatures at different locations of the evaporation structure (shown in Fig. 5d of manuscript) and the ocean water were measured using thermocouples (Omega Engineering, 5TC-TT-K-40-36) and the Omega DAQPRO. The solar flux data was provided using a local weather station maintained by the MIT Sustainable Design Lab. The liquid water produced by the floating solar still was collected in submerged water bottles. The collected water was weighed at the end of the experiment to determine amount produced, and the salinity was measure to ensure that no seawater had leaked in.

4.7. Supplementary Section: Wick to Insulation Area Ratio Using Diffusion Assumption

To aid in the choice of the wick-to-insulation ratio for the evaporation structure, we estimate the minimum wicking area needed, by assuming diffusion through the wick. In reality, some advection occurs in the porous fabric, but the diffusion limit serves as a conservative estimate for the required wick area.

We estimate the NaCl rejected in one solar day, given expected evaporation rates, while avoiding NaCl crystallization on the evaporation structure. Fick's law is used to calculate NaCl diffusion flow from the top of the insulation structure, where excess NaCl is "generated", through the narrow wick, and finally to the bottom of the insulation structure, where natural and forced convection from the body of water quickly disperse the rejected salt. The mass flow rate of NaCl through the wick is given by

$$J = D_{NaCl} A_{wick} \rho_w \frac{(C_{evap} - C_\infty)}{l_w}, \tag{4.3}$$

where D_{NaCl} is the diffusion coefficient of NaCl in water, taken to be 1.99×10^{-9} $m^2 s^{-1}$, C_{evap} and C_∞ are the mass fraction of salt to water at the evaporation surface $evap$ and and bottom ∞, and ρ_w is the partial density of water in the solution. l_w is the length of the wick (2 cm). The NaCl concentration at the top of the insulation structure is assumed to be saturated, the maximum allowable concentration before salt nucleation, corresponding to 26 wt% or (~350 NaCl ppt of water). At the bottom of the insulation structure, the NaCl concentration is assumed to be 3 wt%, similar to seawater. The bottom NaCl concentration is considered constant, because the intended operation of this floating solar still is large bodies of saline water.

The required NaCl mass flow is determined by estimating the excess NaCl generated (m_{exc}, kg) by the evaporation structure with area A_{evap} over one full day of operation, assuming 21% solar-to-water energy conversion (η_{evap}), and allowing for NaCl rejection to occur over 24 hours (t_{day}).

$$m_{exc} = A_{evap} \frac{\eta_{evap} E_{solar}}{h_{fg}} \times \frac{3\ wt\%}{97\ wt\%}, \tag{4.4}$$

where E_{solar} is the total solar insolation in one day (kWhm^{-2}). The wick-to-evaporation area ratio (A_{wick}/A_{evap}) needed is then solved using the following expression:

$$\frac{A_{wick}}{A_{evap}} = \frac{\frac{\eta_{evap} E_{solar}}{h_{fg}} \times \frac{3\ wt\%}{97\ wt\%}}{D_{NaCl} \rho_w \frac{(C_{evap} - C_\infty)}{l_w} t_{day}}. \tag{4.5}$$

For an area similar to Boston, USA, which receives roughly 5 kWhr^{-1} of sunlight per day, we determine the maximum wick area needed to avoid salt nucleation is 22% of the total area. The rest of the thermal insulation structure is taken up by the expanded polystyrene. Our experimental results showed that convection plays a significant role in salt rejection, hence evaporation efficiency can be enhanced by reducing the wick area.

4.8. Supplementary Section: Comparison of Diffusion vs. Advection Differences between Thermal and Chemical Transport

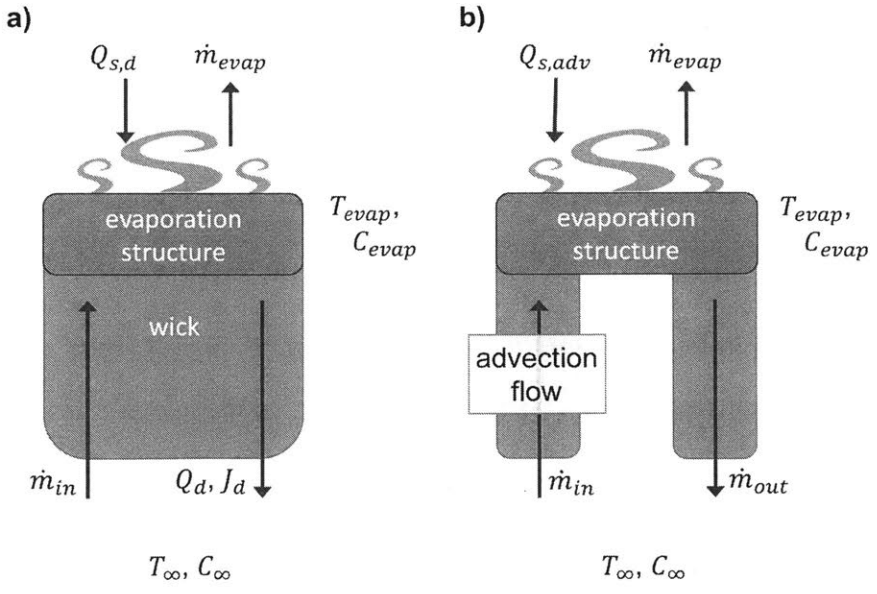

Figure 4.6: Comparison of salt rejection systems based on A) diffusion and B) advection for floating solar evaporation structures. In this comparison, T_{evap} is a controllable parameter, T_∞

and C_∞ are ambient conditions. The heat loss of the two systems are calculated, and a material parameter α_{water}/D_{NaCl} is found to determine whether a diffusion or advection system can best reject salt while minimizing heat losses. This material parameter represents the ratio of solvent thermal diffusivity to solute mass diffusivity.

Salt needs to be removed from the evaporation surface, which can be achieved either by diffusing salt away to the ocean (diffusion) or by washing the evaporation surface with additional ocean water (advection). At first look, advection appears to be a poor choice, given that advection implies higher heat losses, reducing the performance of the system. Diffusion occurs in still waters, and intuitively, still water leads to less heat loss since conduction is less effective than convection.

However, the important consideration is the amount of heat loss per salt molecule rejected. Although water advection leads to high heat losses, it also leads to a high salt rejection rate. If we reduce the overall flow of water, then advection heat losses are reduced as well. We argue here that the use of diffusion or advection is dependent on material properties of the salt and solvent pair, NaCl and water in this case.

We start with a diffusion based system, as shown in Figure 4.6a. The evaporation temperature T_{evap} is fixed, and we assume the salt concentration of the reservoir (ocean) C_∞ and the ambient temperature T_∞ are known. The steady-state energy balance at the evaporation surface is:

$$Q_{s,d} = \dot{m}_{evap}(h_{fg} + c_p T_{evap}) - \dot{m}_{in} c_p T_\infty + \frac{k_w}{l_w} A_{wick}(T_{evap} - T_\infty) + Q_{loss}, \tag{4.6}$$

where $Q_{s,d}$ is the total input heat required to sustain the system, $\dot{m}_{evap}$ is the water evaporation rate (kg/s), h_{fg} is the latent heat of vaporization of water, c_p is the specific heat of water, A_{wick} is the area of the wick, k_w is the thermal conductivity of water, l_w is the length of the wick, and $\dot{m}_{in}$ is the rate of water wicking up in the wick to the absorber surface (kg/s). The first term is the enthalpy leaving through vapor, the second term is the enthalpy wicked up by liquid water, and the third term is the conduction heat losses through the wick. The contribution of NaCl to the

heat capacity is neglected, due to a much lower specific heat and lower mass fraction than water. In addition, parasitic losses such as radiative and convective losses are lumped into a Q_{loss} term.

Since mass is conserved, $\dot{m}_{in} = \dot{m}_{evap}$, and

$$Q_{s,d} = \dot{m}_{evap}\left(h_{fg} + c_p(T_{evap} - T_\infty)\right) + \frac{k_w}{l_w}A_{wick}\left(T_{evap} - T_\infty\right) + Q_{loss}$$

$$= h_{evap}A_{evap}\left(T_{evap} - T_\infty\right) + \frac{k_w}{l_w}A_{wick}\left(T_{evap} - T_\infty\right) + Q_{loss}, \quad (4.7)$$

where h_{evap} is an effective evaporation heat transfer coefficient between the evaporation surface (area A_{evap}) and ambient air:

$$h_{evap} = \frac{\dot{m}_{evap}}{A_{evap}}\left(\frac{h_{fg}}{T_{evap} - T_\infty} + c_p\right)$$

In the steady state condition, for the diffusive system, the salt conservation equation is:

$$\dot{m}_{evap}C_\infty = \frac{D_{NaCl}A_{wick}\rho_w}{l_w}(C_{evap} - C_\infty), \quad (4.8)$$

where D_{NaCl} is the diffusion coefficient (m^2/s) of NaCl in water and ρ_w is the average partial density of water in the wick, C is the local mass fraction of salt to water, and the subscripts $evap$ and ∞ denote evaporation surface and reservoir. The left hand side is the salt accumulation rate on the absorber and the right hand side is the diffusion rate downward.

For the wick length one can write

$$l_w = \frac{D_{NaCl}\rho_w A_{wick}}{\dot{m}_{evap}C_\infty}(C_{evap} - C_\infty), \quad (4.9)$$

l_w is determined and maximized by setting $C_{evap} = C_{sat}$ ($\frac{\dot{m}_{evap}}{A_{wick}}$ is constant), which minimizes the heat conduction loss

$$Q_d = \frac{k_w}{l_w} A_{wick}(T_{evap} - T_\infty). \tag{4.10}$$

The salt rejected via diffusion is then

$$J_d = \frac{D_{NaCl}\rho_w A_{wick}}{l_w}(C_{sat} - C_\infty). \tag{4.11}$$

Q_d is the heat flow through the wick via diffusion, J_d is the salt flow diffused through the wick. The ratio of diffusion heat loss to salt diffusion is

$$\frac{Q_d}{J_d} = \frac{\frac{k_w}{l_w} A_{wick}(T_{evap} - T_\infty)}{\frac{D_{NaCl}\rho_w A_{wick}}{l_w}(C_{sat} - C_\infty)} = \frac{k_w(T_{evap} - T_\infty)}{D_{NaCl}\rho_w(C_{sat} - C_\infty)}. \tag{4.12}$$

This ratio should then be compared with a similar ratio for an advection system, $\frac{Q_{adv}}{J_{adv}}$, the ratio of advective heat flux to advective salt flux.

For the advection system, the heat and salt flows are calculated using the same conditions, i.e., T_{evap} and T_∞ are fixed, $\dot{m}_{evap}$ is fixed, C_∞ is fixed, and $C_{evap} \leq C_{sat}$. Again, the NaCl contribution to heat capacity is neglected. Figure 4.6b describes the energy and mass transport circuit. The energy balance on the advection system is

$$Q_{s,adv} = \dot{m}_{evap}(h_{fg} + c_p T_{evap}) + \dot{m}_{out} c_p T_{evap} - \dot{m}_{in} c_p T_\infty + Q_{loss}. \tag{4.13}$$

Since mass is conserved, $\dot{m}_{in} = \dot{m}_{out} + \dot{m}_{evap}$ and

$$Q_{s,adv} = \dot{m}_{evap}\left(h_{fg} + c_p(T_{evap} - T_\infty)\right) + \dot{m}_{out}c_p\left(T_{evap} - T_\infty\right) + Q_{loss}. \quad (4.14)$$

Again, the heat loss from evaporation can be modeled with an effective evaporation heat transfer coefficient h_{evap}

$$Q_{s,adv} = h_{evap}A_{evap}\left(T_{evap} - T_\infty\right) + \dot{m}_{out}c_p\left(T_{evap} - T_\infty\right) + Q_{loss}, \quad (4.15)$$

where $h_{evap} = \frac{\dot{m}_{evap}}{A_{evap}}\left(\frac{h_{fg}}{T_{evap}-T_\infty} + c_p\right)$. The second term is the advective heat loss, Q_{adv},

$$Q_{adv} = \dot{m}_{out}c_p(T_{evap} - T_\infty). \quad (4.16)$$

$\dot{m}_{out}$ needs to reject the excess salt left by the evaporation process. In steady-state condition, one can write the mass balance for the salt flux

$$\dot{m}_{in}C_\infty = \dot{m}_{out}C_{evap}. \quad (4.17)$$

Using mass conservation, $\dot{m}_{in} = \dot{m}_{out} + \dot{m}_{evap}$, one finds

$$\dot{m}_{out}C_\infty + \dot{m}_{evap}C_\infty = \dot{m}_{out}C_{evap}, \quad (4.18)$$

and

$$\dot{m}_{out} = \frac{\dot{m}_{evap} C_\infty}{(C_{evap} - C_\infty)}. \tag{4.19}$$

$\dot{m}_{out}$ should be minimized to minimize advective heat loss, while ensuring C_{evap} does not exceed the saturation concentration C_{sat}

$$\dot{m}_{out} = \frac{\dot{m}_{evap} C_\infty}{(C_{sat} - C_\infty)}. \tag{4.20}$$

With $\dot{m}_{out}$ determined, the advective heat loss is fully determined

$$Q_{adv} = \frac{\dot{m}_{evap} C_\infty}{(C_{sat} - C_\infty)} c_p (T_{evap} - T_\infty). \tag{4.21}$$

To determine the salt rejected by advection, we consider again $\dot{m}_{out}$,

$$\dot{m}_{out} = \frac{\dot{m}_{evap} C_\infty}{(C_{sat} - C_\infty)}, \tag{4.22}$$

and

$$J_{adv} = \dot{m}_{out} (C_{sat} - C_\infty), \tag{4.23}$$

where J_{adv} is the salt rejection needed to sustain evaporation rate, $\dot{m}_{evap}$. If we compare the ratio of heat and salt advected away,

$$\frac{Q_{adv}}{J_{adv}} = \frac{\dot{m}_{out} c_p (T_{evap} - T_\infty)}{\dot{m}_{out} (C_{evap} - C_\infty)},$$

$$= \frac{c_p (T_{evap} - T_\infty)}{(C_{sat} - C_\infty)}. \tag{4.24}$$

If we compare this ratio to the similar ratio for diffusion,

$$\frac{Q_d}{J_d} \Big/ \frac{Q_{conv}}{J_{conv}} = \frac{\frac{k_w (T_{evap} - T_\infty)}{D_{NaCl} \rho_w (C_{sat} - C_\infty)}}{\frac{c_p (T_{evap} - T_\infty)}{(C_{sat} - C_\infty)}} = \frac{\alpha_w}{D_{NaCl}}, \tag{4.25}$$

where α_w is the thermal diffusivity of water. This figure of merit states that for any given vapor generation $\dot{m}_{evap}$ at T_{evap}, the ratio of heat loss by advection vs. diffusion is determined purely by the material properties. In the diffusive case, we compare thermal conductivity and salt diffusion coefficient, while for the advective case we compare the volumetric heat capacity. For water, $\alpha_w = 1.43 \times 10^{-7}$ m^2/s, and $D_{NaCl} = 1.99 \times 10^{-9}$ m^2/s and the figure of merit is 0.01, suggesting that the better approach to salt rejection in solar evaporation is advection. It is worth pointing out that our analysis is based on saturation salt concentration at the solar absorption surface, but this analysis is also valid for smaller concentrations.

4.9. Supplementary Section: System Heat Transfer Model

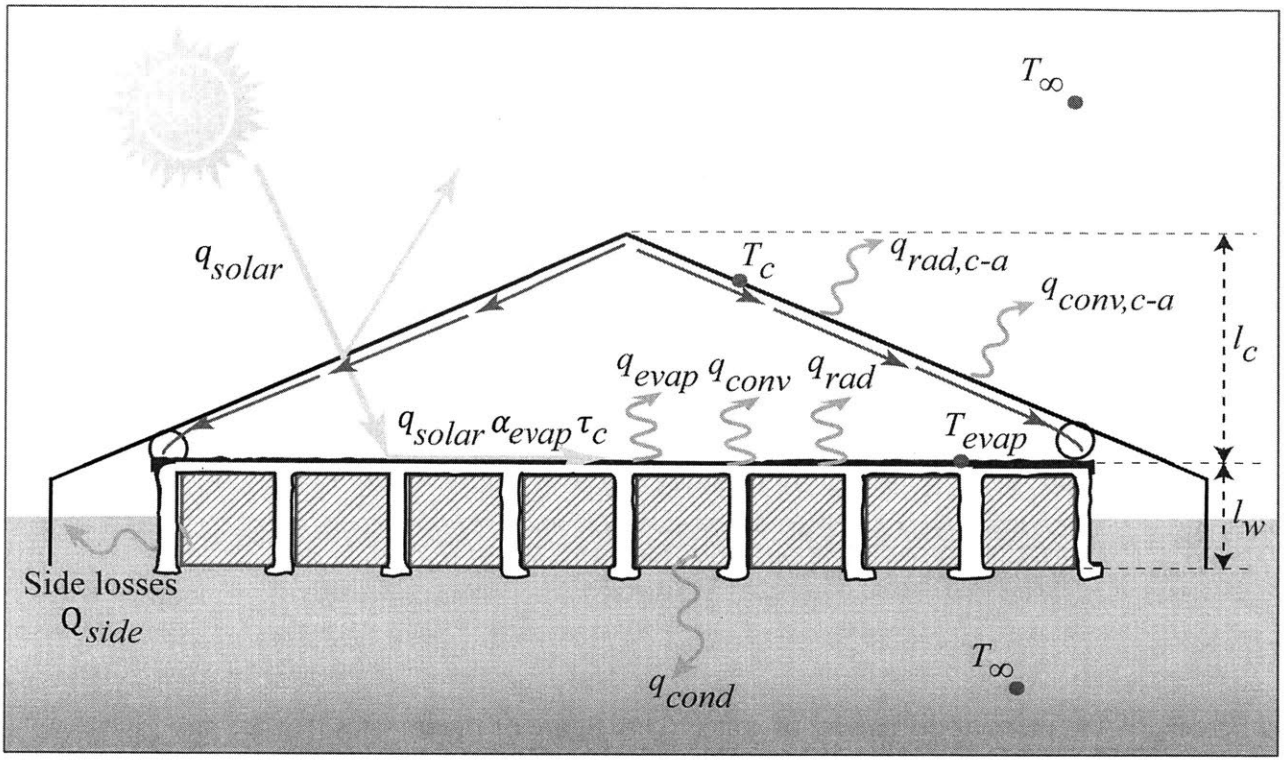

Figure S.7. Schematic diagram of the solar still.

A heat transfer model was developed for the entire floating solar still, including the condensation cover and evaporation structure. The model is based on energy balance at two points, the evaporation structure and the condensation cover. T_{evap} represents the top of the evaporation structure (absorber), T_c represents the cover temperature, and T_∞ the ambient temperature. The steady-state energy balance equation for the evaporation structure is:

$$q_{solar}\alpha_{evap}\tau_c A_{evap} = Q_{side} + A_{evap}q_{cond} + A_{evap}q_{rad} + A_{evap}q_{evap} + A_{evap}q_{conv}, \quad (4.26)$$

and energy balance for the still cover is:

$$(q_{conv} + q_{rad} + q_{evap})A_{evap} = (q_{rad,c-a} + q_{conv,c-a})A_c, \quad (4.27)$$

where q_{solar} is the incident solar flux, α_{evap} is the solar absorptance of the evaporation structure; τ_c is the transmittance of the floating solar still cover; q_{rad}, q_{conv}, and q_{evap} are the radiation, convection and evaporation heat fluxes between the evaporation structure and the cover; q_{cond} is the conduction heat flux from the evaporation structure to the underneath water; Q_{side} is the total heat loss from the side of the evaporation structure; $q_{rad,c-a}$ and $q_{conv,c-a}$ are the radiation and convection heat fluxes between the cover and the ambient; and A_{evap} and A_c are the area of evaporation structure (absorber) and the cover, respectively.

The left-hand side of Eq. (4.26) represents solar heat generation to the evaporation structure considering the cover transmission loss and fabric absorptance. The reflection losses from the wet cover (polyester cover covered with condensed droplets) were chosen based on the experimentally measured values (τ_c=65%). Optical absorptance of the evaporation structure (absorber) was taken as (α_{evap} =85%), but absorption in the polyester film cover for incident solar energy was neglected. Multiple reflection of the solar radiation inside the still is neglected.

Convection through the air inside the still was estimated using a correlation for natural convection in enclosed horizontal spaces[155]

$$Nu = \frac{h_{conv}k_{air}}{l_c} = 0.069Ra^{\frac{1}{3}}Pr^{0.075}, \tag{4.28}$$

where Nu is the Nusselt number, h_{conv} is the heat transfer coefficient (~3 $Wm^{-2}K^{-1}$), k_{air} is the thermal conductivity of air (0.02 $Wm^{-1}K^{-1}$), l_c is the vertical distance of the enclosed volume, Ra is the Rayleigh number, and Pr is the Prandtl number. The convection heat flux inside the still becomes:

$$q_{conv} = h_{conv}(T_{evap} - T_c). \tag{4.29}$$

Radiation heat loss from the evaporator, q_{rad}, is calculated using Stefan-Boltzmann law,

$$q_{rad} = \sigma F_{evap-c}(T_{evap}^4 - T_c^4)\,, \tag{4.30}$$

where σ is the Stefan-Boltzmann constant. The emittances of T_{evap} and T_c are assumed to be 1 (blackbodies), due to the fact that both cover and evaporation structure being covered with water, which is highly absorbing/emitting in the infrared regime. F_{evap-c} is the viewfactor between evaporation structure and cover, which is assumed 1 because the evaporation structure's surface does not see itself.

Evaporation and condensation between the evaporation structure and cover is assumed to be dominated by convection flow of water vapor, and not limited by interfacial transport between the liquid and vapor phases. The following correlation is used for the evaporation heat transfer coefficient:[156]

$$q_{evap} = h_{fg} C \rho_{wa} (\rho_{ca} - \rho_{wa})^{\frac{1}{3}} (W_w - W_c), \tag{4.31}$$

where h_{fg} is the latent heat of vaporization fo water, C is an empirical constant (35 m^2 hr^{-1} $kg^{-1/3}$), ρ_{wa} is the density of air at the evaporation surface, ρ_{ca} is the density of air at the cover surface, W_w is the specific humidity at the evaporation surface, and W_c is the specific humidity at the cover surface.

Heat conduction through the evaporation structure is calculated using Fourier law. The evaporation structure that includes composite insulation (wick, polystyrene) is modeled using parallel resistances. Although we later show advection of water occurs due to salt rejection, we assume thermal conduction here as a conservative estimate of heat loss.

$$q_{cond} = \frac{k_{ef}}{l_w}(T_{evap} - T_\infty), \tag{4.32}$$

$$k_{ef} = \frac{k_w A_w + k_{ins} A_{ins}}{A_w + A_{ins}} \quad . \tag{4.33}$$

The wick is modeled as water (k_w, 0.58 $Wm^{-1}K^{-1}$), and k_{ins} is the thermal conductivity of polystyrene foam (k_{ins}, 0.02 $Wm^{-1}K^{-1}$). The heat conduction flows to the water underneath, which is modeled as ambient temperature, T_∞. This assumes the water flow in real situations imposes a negligible thermal resistance of convection in water (the heat transfer coefficient for forced convection in water is typically hundreds of $Wm^{-2}K^{-1}$). The wick's height is l_w.

The heat losses to the side of the floating still, Q_{side}, were determined using the COMSOL model (section S.5). For a 55 cm x 55 cm floating solar still, the side losses are conservatively estimated to be 10% of the losses from the top of the evaporation structure. This is reflected by using an effective side area, A_{side}, ($A_{side} = 0.1A_{evap}$).

$$Q_{side} = A_{side}(q_{conv} + q_{rad}). \tag{4.34}$$

For the convective heat flux between the cover and ambient one can write

$$q_{conv,c-a} = h_c(T_c - T_\infty), \tag{4.35}$$

where h_c is the external heat transfer coefficient. Here, forced convection due to wind (h_c) is modeled using a heat transfer coefficient of 30 W m^{-2} K^{-1}.

The radiation heat flux between the cover and ambient is

$$q_{rad,c-a} = \sigma F_{c-a}(T_c^4 - T_\infty^4), \tag{4.36}$$

assuming the cover can be modeled as a blackbody due to being covered with water droplets that are opaque in the infrared (optical depth ~0.1mm), and the droplets being thin enough (~1mm) that it is isothermal with the cover and is not a limiting thermal conductance in the heat flux path. The view factor F_{c-a} is assumed 1 due to the cover not viewing itself.

Equations (4.26) and (4.27) form a close system of equations that can be solved iteratively for T_c and T_{evap}. Once T_c and T_{evap} are known, q_{evap} can be determined.

The water collection efficiency η_{water} of the floating solar still is determined by

$$\eta_{water} = \frac{\gamma_{coll} q_{evap}}{q_{solar}}, \tag{4.37}$$

where γ_{coll} is the area ratio of collectable area to condensable area in the cover (not all condensed droplets can be collected). Note that in the mathematical formulation vapor leakage was neglected.

Using this steady–state system model, comparisons with the ocean water collection experiments were made vis-à-vis the solar-weighted, daily-average intensity and ambient air temperature. In the summer, the average solar intensity was typically 750 Wm^{-2}. The daily water collection predicted by the model was within a few percent of the actual collection (24% predicted vs 21-24% measured). The calculated absorber (T_{evap}) and the cover temperature (T_c) using instantaneous solar flux were in agreement with the measured peak temperatures (47°C predicted vs 46±2°C measured). The model inputs are: $q_{solar} = 1000$ W/m^{2}K, $\alpha_{evap} = 0.85$, $\tau_c = 0.65$, $A_{abs} = 1$ m^2, $A_c = 1.44$ m^2, $\gamma_{coll} = 0.847$, $h_{fg} = 2403000$ J/kg, $T_\infty = 302$ K, $h_c = 30$ W/m^{2}K, and $h_{conv} = 3$ W/m^{2}K.

4.10. Supplementary Section: COMSOL Side Losses

A COMSOL model (Figure 4.8)was developed to understand the heat flow through the composite insulation structure, made of wick and expanded polystyrene. The simulation mimicked ocean operation conditions. From the simulation, we determined the heat losses from the sides of the evaporation structure are approximately 6% of the heat losses from the top. In the solar still system heat transfer model, we used 10% to conservatively estimate the side heat losses (A_{side}).

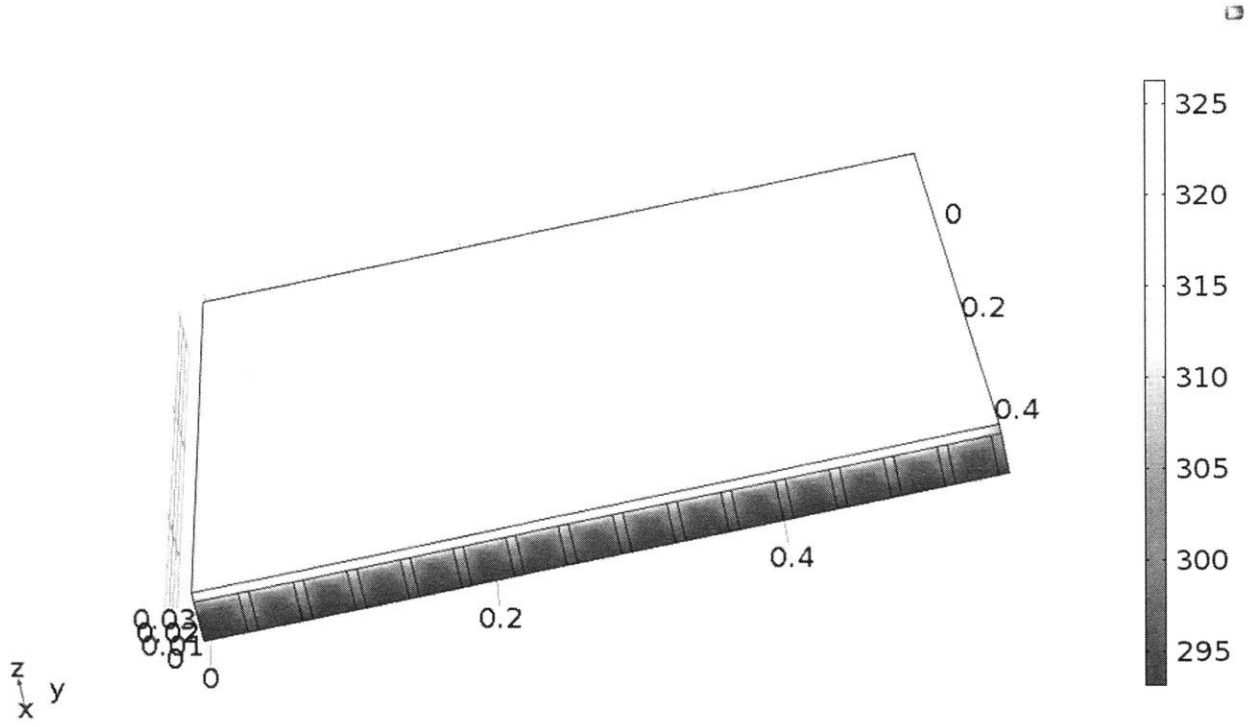

Figure 4.8: COMSOL model of the evaporation structure, to understand heat flow through the alternating wick and insulation structure. Heat flows faster in the water-filled wick, hence the higher temperatures.

The parameters of the COMSOL simulation: The top surface absorbed 1000 Wm^{-2} of incident solar flux, while emitting blackbody radiation (emittance $\varepsilon = 1$), convective losses ($h = 10 Wm^{-2}K$), and evaporation loss ($h = 20 Wm^{-2}K$). The sides also emitted the same convective and radiative losses. The bottom temperature was set at ambient temperature (293K), due to forced water convection rapidly cooling the bottom. The wick (thin) and insulation (thick) layers were

modeled with the thermal properties of water and air. The geometric dimensions of the structure were measured from the evaporation structure prototype.

4.11. Supplementary Section: Optical Properties

Below is the optical reflectance data for the dyed cellulose fabrics (Zorb) used as a solar absorber in the evaporation structure, and the dry polyester film used in the floating solar still cover. The polyester film with droplets was not measured in the spectrophotometer due to the vertical orientation of the sample aperture, which would cause the droplets to shed off. The wet polyester film transmission used in the system heat transfer model was measured using a calibrated thermopile (Newport, 818P-040-55) and a solar simulator (ScienceTech, SS-1.6K).

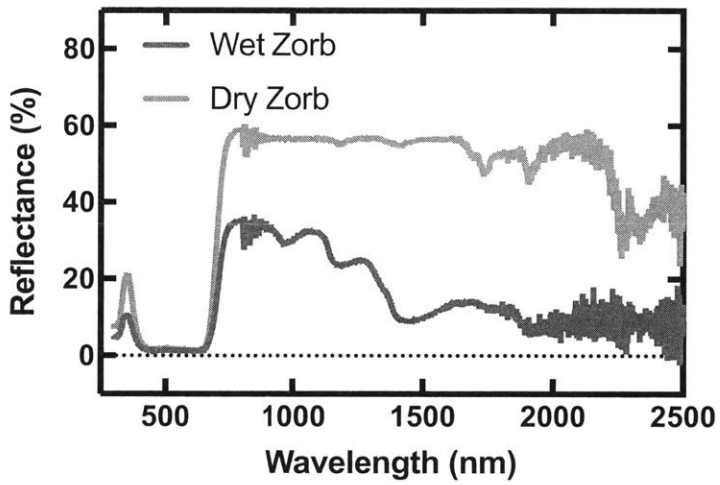

Figure 4.9: The total reflectance (diffuse + specular) of wet and dry Zorb, which is used in the evaporation structure to absorb sunlight.

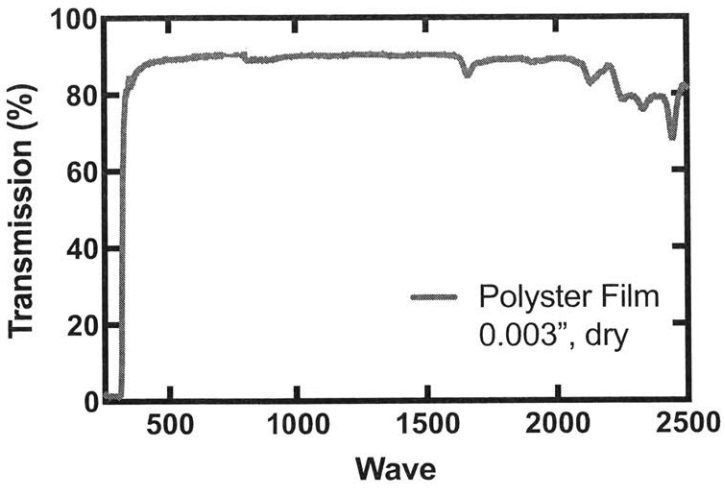

Figure 4.10: The total transmission (diffuse + specular) of the dry polyester film used in the floating solar still.

4.12. Supplementary Section: Cost Analysis

The floating solar still was designed with low system cost in mind. The design is entirely polymer and fabric based. The materials list include 3/8-inch polypropylene rods (McMaster-Carr, #8658K52), custom-machined acetal connectors, 0.003-inch thick clear polyester film (McMaster-Carr, #8567K32), cellulose fabric (Zorb®, Wazoodle Fabrics), and expanded polystyrene (Owens Corning, Foamular 250). The cost of each part is summarized below using prices of similar items found on Alibaba.com, a wholesale market:

- Polypropylene rods: \$1/m^2 of solar still (\$1.5/kg), ~8m of rod used.
- Acetal joints: \$0.10/m^2 of solar still (\$1.5/kg), but cost is probably dominated by manufacturing
- Polyester film: \$0.10/m^2 of solar still (\$2/kg), 1.4 m^2 of film used
- Expanded polystyrene: \$1.5/m^2 of solar still (\$60/m^3), 2.5cm thick boards used
- Cellulose fabric: \$0.30/m^2 of solar still (\$2/kg), 150g used
- Plastic tube fittings: \$0.40/m^2 of solar still (\$0.10/fitting), 4 used
- PVC tubing: \$0.10/m^2 of solar still (\$0.05/meter)

From this quick estimate, the materials cost of the floating solar still is around $3 per square meter of solar still, to produce 2 L per day. The cost is extraordinarily low. Additional tubing may be needed to connect multiple systems together.

The floating solar still has two advantages: low cost per m^3 of water produced, and ability for distributed desalination. The floating solar still has an estimated water production cost of about \$1-2/m^3. This is based on a two-year lifetime for the system. The cost is on par with reverse osmosis (\$0.5-\$5/m^3 based on scale and salinity) and multi-stage flash (\$1-3/m^3). Our cost is even an order of magnitude lower than traditional single-basin solar stills (\$15/m^3). The second advantage is that we are able to produce water at the same price, at small capacities, whereas reverse osmosis costs go up dramatically at smaller scales (up to \$10/m^3). The floating solar still cost is based on area, and scales linearly with production capacity.

4.13. Supplementary Section: Salt Rejection Diffusion Assumption

In constructing the wick-to-insulation ratio for the evaporation structure, we estimate the minimum wicking area needed, by assuming diffusion through the wick. In reality, there is some advection occurring in the porous fabric, as indicated by the measured salt concentrations, but this serves as a good conservative estimate.

We estimate the NaCl rejected in one solar day, given expected evaporation rates, while avoiding NaCl crystallization on the evaporation structure. Fick's law is used to calculate NaCl diffusion flow from the top of the insulation structure, where excess NaCl is "generated," through the narrow wick to the bottom of the insulation structure, where natural and forced convection from the body of water quickly disperse the rejected salt.

$$J = -D_{NaCl,H_2O} A_{wick} \frac{\Delta C_{NaCl}}{x} \tag{4.38}$$

The diffusion coefficient of NaCl molecules in water, D_{NaCl,H_2O}, is taken to be $1.99 \times 10^{-9} m^2 s^{-1}$. J is the mass flux of NaCl, A_{wick} is the area of the wick, ΔC_{NaCl} is the concentration difference of NaCl between top and bottom, and x is the height of the wick (2 cm). The NaCl concentration at

the top of the insulation structure is assumed to be saturated, which is 26 wt%. At the bottom of the insulation structure, the NaCl concentration is assumed 3 wt%, similar to seawater. The bottom NaCl concentration is considered constant, because the intended operation of this floating solar still is large bodies of saline water.

The required NaCl mass flux is determined by estimating the excess NaCl generated by the evaporation structure (m_{exc}) in one full day of operation, assuming 50% solar-to-vapor energy conversion (η_{evap}), and allowing for NaCl rejection to occur over 24 hours (t_{day}). E_{solar} is the total solar insolation in one day.

$$m_{exc} = \frac{\eta_{evap} E_{solar}}{h_{fg}} \times \frac{3\ wt\%}{97\ wt\%} \tag{4.39}$$

The area of wick needed is then solved using the following expression:

$$A_{wick} = \frac{\frac{m_{exc}}{t_{day}}}{-D_{NaCl,H_2O} \frac{\Delta C_{NaCl}}{x}} \tag{4.40}$$

For an area similar to Boston, USA, which receives roughly 5 $kWhr^{-1}$ of sunlight per day, we determine the maximum wick area needed to avoid salt nucleation is 22% of the total area. The rest of the thermal insulation structure is taken up by the expanded polystyrene.

Chapter 5

5. The Maldives, a Case Study

This chapter deals with techno-economic analysis of the Maldives as a potential market for deployment of chapter 4's floating solar still. Some of the information in this chapter is obtained by the helpful work of Matt F. Rosen and David Bierman on a market research trip to the Maldives.

5.1. The Maldives Overview

The Maldives is an island nation consisting of nearly 2,000 small islands, grouped in 26 atolls that are spread out over almost 100,000 km^2. The population is 393,000, and inhabit 200 of the islands. The total land area is only around 300 km^2, and the capital Malé is one of the densest cities in the world. The country is situated in the Indian Ocean, about 500km from India, and is thus very isolated. The main drivers of economy are tourism and fishing. The Maldives represents a typical tropical island with features that suit deployment of floating solar stills: abundant solar resources, access to the ocean, a lack of competing freshwater sources, a lack of competing energy sources, and relatively undeveloped infrastructure. Land area is at an extreme premium, with many smaller island only several hundred feet wide. Thus, land-based solar technologies are poor competitors. This combination of shortcomings and resources on typical tropical islands appears well-suited for the solar evaporation technology in this thesis.

5.2. Water Resources

The Maldives resides in a tropical climate, with average temperatures of 28°C, average relative humidity of 80%, and average rainfall of 1980mm. The abundant rainfall is the primary source of drinking water for much of the population living outside of the capital (Malé). Pumped groundwater supplements water usage. In the capital, a desalination plant with 5,800 m^3 per day capacity is currently installed, and provides water. Outside of Malé, desalination plants have been installed in some other islands, including Kadholhudhoo, and Gulhi.[157] A total of 57 small

desalination plants were shipped to the country after the 2004 tsunami, although most of them are non-operational. The reasons varied, from lack of training, lack of replacement parts, to some of the plants being for temporary use during the tsunami recovery. Both reverse osmosis and membrane distillation utilizing waste heat have been installed. The cost of desalination is higher than in developed nations like the US, due to the need to ship in fuel (diesel or other). Consumer cost is charged on a tiered pricing structure, from \$2-8 per m^3 of water consumed.[158]

Due to the high cost of desalinated water, most Maldivans typically rely on rainwater and groundwater resources to satisfy their water needs. Rainwater is collected in different types of storage tanks, and used throughout the years. Most households in the Maldives have a rainwater tank attached to the home, and the roofs are often used to collect and funnel the rain water into the storage tanks. Rainwater is available 8-10 months out of the year, during the wet season. However, during the dry season, January-April, rainfall sharply drops and storage tanks may run dry. Locals report anecdotally the dry season have become harsher, perhaps due to climate change.[159]

Groundwater represent an alternate water source, though one that is becoming less reliable. The average height of the Maldives is only 1.5 m above sea level, and thus groundwater is mostly contaminated with salts from the surrounding ocean. To compound the problem, increasing population density in the Maldives has caused the groundwater to be contaminated due to poor sanitation from households. The soils in the Maldives are formed from crushed coral deposits, and are highly permeable. This allows pollutants to spread quickly in each islands.

Most islands contain a small portion of freshwater, also termed a freshwater "lens".[160,161] This freshwater lens is created from rain soaking through the soil, and the thickness of the freshwater lens depends on a number of factors, including soil permeability, rain recharge rate, and size of island. The freshwater lens thickness is rarely more than 12m. [158,160,162] Hence, on the Maldives, natural freshwater resources are precarious and heavily dependent on the climate, and desalination technologies are needed to ensure water security.

A distinction should be made between small resort islands operated by foreign hospitality organizations, and islands populated by the native people. The resort islands are typically self-sufficient and have their own desalination plants. Tourism revenue is enough to cover the high costs of small self-contained desalination plants.

5.3. Spending on Water by Maldivans

The average household in Malé spends between $40-60 per month on water, which represents 5% of the household expenditure. Drinking water costs average around $5 per person, per month.[159] Given that the Maldives has a population of 393,000, the total addressable market for drinking water in the Maldives is around $18 million, which is a prime size for a beachhead market, and initial small market for a startup company to target.[163]

"Significant" amounts of drinking water is obtained from buying bottled water at stores, which cost on the order of $0.25/L, or $250/$m^3$.[159] According to one café owner, in many of the smaller islands, residents receive free water shipped in by the government to supplement rainwater usage. This suggests that a better market would be the larger islands.[159]

5.4. Key Stakeholders and Potential Partners

The research trip yielded some interest by local town councils in setting up a pilot study for a floating solar still desalination unit. In addition, international organizations such as the UNDP, UNOPS, and UNICEF expressed interest in funding a pilot study. Government organizations such as the Ministry of Energy and Environment will want to approve any pilot studies. Locals also mentioned that political vandalism was a common problem, so care must be taken to determine which political parties to align with. Ideally, a neutral party such as UN-affiliated groups should back the project.

5.5. Miscellaneous Information

Additional information was gained after discussing with the Malé Waste and Sewage Company (MWSC), the local water utility in Malé. They claimed households would be willing to spend 10,000-20,000 rf, or $700-1300 in capital expenditures, and an annual operating expenditure of 2,500 rf, or $150, for a system with a 3-year lifetime. These numbers are approximate, and more market studies should be done to refine. In the same conversation, MWSC claimed average annual household expenditures on electricity and water totaled 1,200-2,000 rf, with water

comprising the majority. MWSC also cautioned about designing for operation with tides, as the sea level can change ±1 m.[159]

5.6. Conclusions

From the market research trip, it appears that the Maldives has good potential as an initial market for a floating solar still. Residents are paying $7-10 per m^3 of water produced from the utilities, and are even willing to spend $1000's on a new water solution. The trip identified several parties who were interested in helping with a desalination pilot project, including non-governmental organizations and local town councils. Most importantly, contacts were made with local United Nations organizations (UNDP, UNOPS), which showed willingness to consider future pilot studies with the technology. Allying with a neutral international party would allow a potential startup to get above the political infighting currently in place, and avoid upsetting important parties. Additional useful information was gained when the local sewage company mentioned that residents would be interested in a rooftop solution as well.

The biggest problems identified was how to site a potential floating solar still installation. Waves present a challenge in the open ocean, even with protective reefs near the islands. Inland lagoons are limited. At the same time, changing ocean depths due to tides need to be managed. Different solutions to be explored include sinking pylons into the ocean floor, or using smaller sand anchors to retain the floating solar still system. Also, a system for bringing the condensed water to land needs to be designed. On the business side, business models need to be developed. It should be decided whether a business will be based on selling water, or selling water-producing units. A comprehensive study of individual islands should be conducted to understand whether initial markets should focus on the many competition-less small islands or the few big islands with competing municipal water companies.

Chapter 6

6. Summary and Future Directions

Water and energy are two of the defining technological problems of our time. Though technologies exist to desalinate water and harness renewable solar energy, there is a lack of solutions for distributed and small-scale desalination technologies, especially those operating on solar energy. This thesis worked towards developing technologies utilizing solar energy for low-intensity vapor generation in applications such as desalination and wastewater management.

Several characteristics define applications utilizing of low solar fluxes. Upon lowering optical concentration requirements, system cost and complexity is greatly reduced, and technology accessibility is increased, especially in regions with poor infrastructure. However, because of the low solar flux, vapor generation is less efficient because of the reduced operating temperature. The main challenges are to reduce the amount of parasitic heat losses to the environment, such as radiation, convection, and conduction. This reduction in heat loss is termed "heat localization".

Heat localization is possible through several approaches, including 1) localizing solar absorption to near the evaporation surface, and 2) minimizing wasteful heat loss from the evaporation surface. The first topical chapter of this thesis focused on using carbon-based nanofluids to absorb and convert solar energy into heat energy for vapor generation. The second topical chapter of this thesis details development of a solar steam generator that operated at 100°C without any optical concentration. The last topical chapter developed an evaporation structure designed for desalination, and was capable of rejecting salt for continuous operation. A collection cover was also built to condense the generated vapors into drinkable water.

In the study on nanofluids for solar vapor generation, three carbon-based nanofluids were subjected to 10x solar concentration, and their vapor performance characterized. It was determined that at steady-state operation the performance was similar. However, under transient conditions, it was determined that vapor generation performance is dependent on nanoparticle surface properties. Nanoparticles with better wettability and dispersion into the fluid absorbed solar energy closer to the fluid-air interface, thus allowing evaporation temperatures to rise faster. This led to faster evaporation response. Nanofluid evaporation rates were also well predicted by

classical evaporation heat transfer coefficients, which suggests that nanofluids evaporate using classical evaporation phenomena, and not a recently touted nano-bubble formation theory. The nano-bubble formation theory requires the bulk fluid to remain at cold temperatures, which is difficult to achieve under solar illumination. This was confirmed by COMSOL simulations of individual nanoparticles, which showed heat to transport rapidly to the bulk fluid, which causes the fluid to evaporate. The study on nanofluids showed both experimental studies of nanofluid evaporation performance, and fundamental insight into nanofluid evaporation mechanisms.

The chapter on the solar steam generator developed a small affordable device made of common materials, that could reach high temperatures (100°C) with only the power of the ambient sun. Generating 100°C steam with the meager power of ambient sunlight ($1kWm^{-2}$) required significant heat localization, while keeping materials simple and available. Materials such as styrofoam, bubblewrap, and spectrally selective coatings were used to reduce conduction, convection, and radiation thermal losses. The performance of the solar steam generator was characterized at different vapor generation rates and operating temperatures, with higher vapor generation corresponding to lower temperature. A system heat transfer model was developed to predict device performance. Furthermore, the evaporation rate dependence on geometry was studied, which suggested smaller evaporation areas to have higher evaporation rates. This study's results imply that by combining smaller evaporation areas with radiation suppression from spectrally selective absorbers, it may be possible to create more efficient evaporation surfaces than water itself (due to water's inherent thermal emission).

Finally, the chapter on a salt-rejecting evaporation structure advances the field of solar vapor generation towards real applications such as desalination. In this chapter, an evaporation structure was developed that could simultaneously provide salt rejection while maintaining thermal insulation. Thus far, this has been poorly studied in the literature, and is a key bottleneck preventing floating solar vapor generating structures from being deployed. The simultaneous salt rejection and thermal insulation was achieved by using a composite structure of fabric wicks for water uptake and salt rejection, and expanded polystyrene for thermal insulation. The ratio of fabric to polystyrene is tuned to maximize thermal insulation. The salt rejection ability of the evaporation structure is demonstrated in several on-sun experiments, after which salt accumulation was not observed. Design guidelines are given for whether advection or diffusion is preferred in the wick, to minimize heat loss. A condensation cover was designed out of low

cost materials. The entire evaporation structure plus condensation cover system was tested on MIT's roof and in an actual ocean, and 2.5 $Lm^{-2}day^{-2}$ water production was demonstrated. This amount is the recommended daily water consumption for individuals.

This work was motivated by the desire to provide affordable and accessible fresh water to all populations, especially those in developing regions without access to good infrastructure nor the ability to maintain advanced equipment. This thesis has shed fundamental insight into solar vapor generation and salt rejection processes, as well as demonstrate several prototypes for steam and vapor generation, and water collection. Ultimately, a device was created that can produce enough water for individuals, at an affordable cost of $\$3m^{-2}$.

Future Directions

In recent years, research has exploded in the area of floating structures and materials for low-cost solar vapor generation. From nanofluids, to plasmonic materials, to nanostructured materials such as carbon nanotubes, intense focus has been placed on generating vapor efficiently. However, comparatively little focus has been placed on developing comprehensive approaches to solve real problems, and on evaluating the evaporation and heat transfer mechanics of such systems. Generating vapor is only one component of a full solution to desalination, or wastewater treatment. In a wastewater evaporation pond, it has been suggested numerous times to deploy solar absorbing structures floating at the surface, to harness solar energy for water evaporation. Many technical challenges remain undemonstrated, however. How does solar-driven evaporation interact with advection-drive evaporation from winds? How do environmental factors affect the performance of these floating solar absorbers? In addition, operational realities such as replacement of material structures due to fouling need to be addressed. Some recent publications have addressed these issues flippantly, assuming solutions to be trivial when in practice and in commercial settings, they often determine an approach's viability.

On the fundamental side, many exciting challenges exist in surface interactions between the various materials used in solar vapor generation, and the liquids they interact with. For example,

in the condensation structure in chapter 4, a major source of loss is optical loss due to beading of droplets. Proper surface engineering, whether through higher hydrophilicity or nano/micro structuring can ensure better wettability, leading to lower optical loss. In turn, fluid dynamics modeling must be done to ensure film-wise condensation does not impede the ability of condensed water to flow and be collected. Another area of interest may be in nanoparticle wettability in brines with high salinity and total dissolved solids. Nanoparticles are an attractive approach to evaporating evaporation ponds because of their consumable nature, which reduces fouling concerns. However, in high salinity brines approaching saturation, nanoparticles interact with salt ions nearly as much as water molecules. Nanoparticles which are easily dispersed in water can aggregate and precipitate out in concentrated brines. Surfactants may be needed to successfully suspend nanoparticles. Careful selection of surfactants is needed, as ionic-based surfactants will compete with the salt ions to dissolve in water.

There is also significant thermal engineering left in floating solar evaporation structures. A major performance increase could be attained if we can recycle the latent heat lost through vapor condensation. This process, sometimes known as multi-effect, is commonly used in traditional thermal-based desalination technologies, such as multi-effect distillation (MED), multi-stage flash (MSF), multi-stage membrane distillation (MD), and more. However, this has thus far not been implemented in floating solar evaporation structures due to cost reasons, an lack of scale or infrastructure. For example, existing technologies often require active processes, to pump feedwater through the desalination process. In floating solar evaporation structures, the target cost is much lower, and passive systems are often required to deliver water for evaporation.

A specific subset of nanoparticles, known as micro-nanomachines, have potential in disrupting boundary layers in thermal, chemical, and other processes. These nanomachines are able to to actively propel themselves through the liquids, typically by relying on an external energy source, such as light, electric fields, magnetic fields, or chemical sources. The ultimate effect is to enhance mixing at the micro to millimeter scale. The nanomachines could be utilized in solar applications to benefit existing membrane-based desalination technologies, where thermal and saline boundary layers often dominate system performance. For example, in reverse osmosis, a heightened salt concentration near the membrane (concentration polarization) can increase the pressures needed to drive reverse osmosis, as well as increase the likelihood for fouling at the

membrane. Solar-excited nanomachines could be used to disrupt the concentration polarization by mixing the boundary layer with the bulk feedwater.

There are also many questions to be answered regarding evaporation rates in real conditions for floating structures for solar evaporation. Current work has largely focused on evaporation experiments under laboratory conditions, whereas real conditions include factors such as wind and large volumes of air above the evaporation surface. These factors all affect the mass flux of the water vapor away from the evaporation surface, and thus affect the evaporation rate. The role of solar heating in enhancing evaporation rate is not clear, and current definitions for evaporation efficiency are unsatisfactory. For example, different regimes may occur depending on the windspeed above the evaporation surface, compared with solar heating. If the windspeed is much higher than the amount of incoming sunlight, the evaporation surface may remain cooler than the ambient temperature, thus allowing 100% of the converted solar thermal energy towards evaporating water. This would occur regardless of the thermal design of the floating structure. Conversely, if the windspeed is much lower than the incoming sunlight, then conventional heat losses such as convection and radiation may play a role. The mass flux in floating solar evaporation systems needs to be better understood.

Preventing salt nucleation is another challenging area of research for floating structures for solar evaporation. This ability is useful in high salinity environments, such as those found in wastewater ponds or in zero-liquid discharge applications. In these environments, the salt concentration is typically saturated, and even super saturated near the evaporation surface, and salt nucleation is inevitable. The goal is to then retard nucleation on the useful evaporation equipment, and force nucleation to occur on other surfaces, such as the walls and floors of wastewater ponds. The key parameters are nucleation activation energy and density of nucleation sites on the floating structures. Higher super saturation levels are needed near the floating structures, and nucleation should be encouraged at other surfaces in the evaporation ponds at lower super saturation levels. This can be achieved by using a variety of hydrophobic and low energy surface materials for the floating structure. One type of material is fluorinated polymers such as PTFE, which are widely available. Another approach is to use liquid-infused materials that combine the stability of a solid for a substrate, with the surface properties of a coating liquid. The coating liquid is very smooth and has a low density of nucleation sites, and with proper selection, can have very high activation energies for nucleation. The liquids must also be chosen

such that they adhere to the solid substrate, even when submerged in saline water. Careful selection depends on the surface energies of the liquid-solid, liquid-water, and solid-water interfaces. Examples of potential liquids include different fluorinated oils and silicone oils, such as Krytox family of oils. If successful, floating structures that are impervious to fouling could be used to enhance evaporation in wastewater ponds, leading to 1) reduced land use for these ponds, and 2) reduced risk of overflow from rain and waste management, which lead to costly environmental fines.

Appendix

Notes from UNDP meeting, 2017-1-12

Participants:

- Aishath Azfa, Project Manager, Low Emission Climate Resilient Development Program, UNDP
- Abdulla Waheed, Small Grants Officer, Low Emission Climate Resilient Development Program, UNDP
- Shelton (sp?) _____, UNDP
- Matthew Rosen, MIT

Notes:

- On islands, people are mainly using rainwater catchment (drinking), bottled water (drinking), and where it is available, groundwater (for washing, agriculture, etc., but not drinking).
- Groundwater lens is vulnerable to pollution, waste seepage (mostly granular soil)
    - Generally, groundwater is not safe for drinking on islands
    - Lens is ~5 cm from surface
    - Seepage takes ~1 hr to reach lens
    - Bad use of fertilizer
    - Also, poor sanitation systems
    - No quality testing mechanisms in place
    - Perceptions on groundwater have changed over time (no longer viewed as suitable to drink)
- Most houses have 1200 L rainwater tanks
    - But this is regardless of household size
- Generally speaking, there haven't been recent instances of community rainwater tanks,
    - EXCEPT, there are a number of new community systems that were just installed
    - Success is unclear as of yet (haven't gone through a full season)
    - In one atoll, community tanks have been installed on every island
    - Community systems are a collection of 1200 L tanks, connected via piping, inside a building.
        - One system Azfa showed me had a roof for catchment, but no walls
            - She was worried about vandalism at this facility
        - Another was enclosed with walls ("H2O project")
            - She thought this system was appreciably better than the other one because of the increased security the building walls provided.

                - Had a youth recreation room with a TV that would play soccer matches, etc. intermixed with informational materials on water security, system upkeep, etc.
                - Maintained by community council
                - In heavy rain, the tanks would be filled in 20 minutes and last 6 months (combined capacity = 100,000 L)
                - Maintained by island council
    - Another challenge with rainwater systems is that rains are becoming more short and erratic
        - Typically, people would run up to the roof and clean out gutters, tank, etc. when it started raining, and let the first rain flow out of the system through an overflow valve.
            - Relatively easy, and even considered fun
        - Now, the rain event may be over by the time they finish cleaning the roof.
        - Additionally, some challenges with roof cleaning:
            - Men are often at work (sometimes another island at a resort) and often aren't there to clean the roof when it starts to rain
            - Women, while generally at home, often have a lot of other responsibilities.
            - While some women will clean roofs, it is a challenge, and is somewhat less culturally acceptable than men doing it.
            - Elderly people may have much more difficulty (or can't do it at all)
        - Azfa personally feels that rainwater collection is the best solution for the Maldives.
            - Doesn't think desalination on every island is practical
    - Pre-tsunami, there were community tanks at mosques, but due to growing populations, etc. no longer there
- Dry period (historically, Jan – March) is extending (climate change)
    - Demand isn't being met in many places
    - Some islands are requesting "emergency" water every year
        - *Disaster management department was* responsible for transporting water out to islands when this happened, though they otherwise had little to do with water sector. No mandate.
            - There are only a few vessels in the Maldives suited for transporting large quantities of water long distances
            - Might take 2 days to reach islands, and by that time, the water is often contaminated
                - Tested before it left, was OK quality.
            - Very expensive and wasteful, not sustainable
            - *Fenaka is now* managing the transport of water in these cases
            - [Azfa said she will provide lists of islands that have needed emergency water over last 3 years, as well as costs associated with transportation, etc. (transportation is more expensive than production)]

        - Ministry of Environment and Energy, Water Dept. is responsible for Policy surrounding water
        - EPA is responsible for [governance?]

- Some larger islands have piped water systems
- UNDP supported projects:
    - IWRM (integrated water, rainwater management)?
        - Rainwater
        - Groundwater
        - Desalination
    - Main barrier with desalination is energy requirements, so some plants use solar PV to run plants
- UNDP will be providing:
    - 45 community rainwater collections systems
    - 4 IWRM systems
- After the Tsunami, 51 desalination plants were installed on various islands
    - 28 were still operating in 2011
    - Only a handful operating today
        - Sometimes procurement issues
        - Maintenance issues, etc.
    - All resorts have desalination systems, and are required to have 3 days backup supply.
        - But they are not required by the government to provide assistance to homes nearby in the event of drought. (boats will come from Male instead of water of resort on the same island)
- Potential for pilot testing:
    - UNDP has an innovation arm that may be interested in WISPS (no one was in office today, may be able to talk with them this trip)
        - Potential for cost sharing
    - UNDP Grants program could be another route
    - Important groups to engage if running a pilot study
        - EPA [political?]
        - Water Department & UNDP [technical]
    - Generally speaking, UNDP was relatively positive about potential partnerships for a pilot test.
        - However, I wouldn't say this sentiment necessarily reflected a perception that this would work (i.e. they maintained legitimate concerns and had good questions, but seemed willing and interested to try new technologies)
    - Thought WISPS was more likely to work in larger islands that were less congested/dense than smaller ones (sometimes land for a structure is extremely hard to come by)
        - Bigger lagoons on bigger islands
        - Some concern with jetty's already being overcrowded, so would want to implement away from them.

        - Not entirely clear to me why they were concerned with smaller islands in an off-shore implementation scheme, but best I could gather was that even very small on-land infrastructure was hard to find space for.
            - Possible to potentially locate system on nearby uninhabited islands, but concerns about transportation of water in that case.
        - Better bet, they thought, was to locate it on a bigger island, somewhat away from people, and then pump water to town.
    - Suggested Maalhos could be a good place to pilot.
        - Strong council
        - History of implementation projects
- SWIMSOL (doing floating solar PV) is another company we should contact
    - Did a pilot in Maldives
    - Challenges that came up:
        - Birds pooping on installations
        - Concerns with bait fisheries
        - Issues with anchoring
            - Disturbance in sediment
            - Worries about reef

Weather

- Not all islands are sheltered
- Many atolls aren't protected
- Some have lagoons, others do not
- All three thought that WISPS type of system could only work on atoll (protected) side of islands
- Questions over what the effects of weather would be on this type of system
- Concerns with wave protection and size of system
- During SW monsoon, waves are bigger
    - 2-3 feet? (waves I observed this morning might have been 2-3 feet, so this might be a conservative estimate)
- During other monsoon, strong current
    - A sort of "ripple effect" happens where water is very rough, couldn't really surf
- Local knowledge based on moon, etc. calls out "micro-seasons" that last 2 weeks.
    - Both claimed this was pretty accurate at predicting weather, agriculture info., etc.
    - There's an app for it called Nakaiy Nevi (can download it)
- Recognition amongst elders that weather is becoming harder to predict (climate change)
- Rains are now shorter and more erratic

Who would might ultimately maintain a WISPS system?

- Fenaka?
- An NGO?

- Local council?

Main Questions from Shelton

- What effects do weather have?
  - Lack of protection, waves
- Security of the system (vandalism, etc.)?
- How much does it cost?
- Where does the investment come from?
- Who maintains it?
- Space required?

- Vandalism is a significant concern/issue
  - Two main political groups (Ruling party vs. coalition of challenging groups)
  - Often, new projects may get caught in the middle of political conflict. People may vandalize projects for this reason.
  - People may also attack or object through more official channels to such projects for political reasons (i.e. proposed or implemented by other group)
  - Who implements the project is important
  - Council elections are coming up this year, national election next year
  - School environment is typically them most impartial place, and is a good option for pilot studies as they can additionally provide management and security.
    - UNDP may be more likely to partner with a pilot at a school
      - They recently did a PV installation on a school
- Economics
  - Azfa to provide some data on emergency rainwater costs
  - Communities don't pay for rainwater collection systems (sometimes community systems are fundraised in part by local council, but this sounded like the exception)
  - Communities also don't pay for emergency water deliveries
  - People do pay for desalinated water
    - HOWEVER, many people on Male don't actually drink the desalinated water, but instead use it for washing, etc.
    - Similar on other islands with desalination plants.
  - Bottled water is pretty cheap (Azfa thinks too cheap), 5 L = 10 rufiyaa (~$0.75 USD)

Places to visit/people to talk to:

- Maalhos
    - Contact: Mujuthaba a.k.a. Mujey – 9907875
- Ulkahos – Azfa to send contact info
- Mahibadoo – Azfa to send contact info
- Thoddu?
- Water Care (NGO) – Azfa to send contact info
- Ministry of Energy and Environment → Shahida (head of dept.)

Conversation Notes, 2017-1-14

Hey George,

The sense that I got is that the decline of some of the desalination systems seems to be the classic case of lack of maintenance, spare parts, technical expertise etc. related in part to a lack of ownership and sustainability. That's in reference to a large portion of the 51 plants that were installed after the tsunami by (I believe) international organizations. It's unfortunately an extremely common occurrence to see sexy implementation projects fail in short order because of a lack of ownership, maintenance plans, or sustainable funding structures (donors rarely want to fund upkeep, and alternate sustainable maintenance structures aren't always put in place). That said, for something so overtly technical and industrial, it's definitely at least a bit surprising to see this failure mode (it sort of makes more sense for lower tech. projects where it might not be quite as glaringly obvious that technical expertise and maintenance will be critical to long-term sustainability).

The lack of people drinking desalinated water was surprising to me as well – I think this is both a perception issue combined with the fact that bottled water is considered cheap (nearly everyone I've talked to, including residents, hold this view. That said, a few people I've talked to do have in-home filtration systems to save money/hassle compared to bottled water). The other factor is that it seems some people think that bottled water is actually mineral water, and therefore higher value.

Had a long chat with an entrepreneurial café owner today who had some interesting insights.

· Thought that smaller islands wouldn't really need or value WISPS as they're generally self-sufficient with rainwater collection and in some cases, emergency water boated in. In both cases, they don't pay for water. Slightly different reasoning, but backs up what UNDP said on this.

· Thought there may be a use-case in some of the larger islands where it might supplant or augment a more expensive desalination system.

o On those islands, people would typically buy desal water if their rainwater ran out.

I want to double check whether people also don't drink desalinated water on islands, or just in Malé.

o He suggested two models that might work:

Bottle water on the island and sell that (if it can be done cheaper than current option).

Have a truck that drives around the island and fills up rainwater collection tanks.

To your question, he said water is bottled in Malé and then shipped out to islands. Will confirm this with WHO tomorrow.

Also learned a lot more about the political situation yesterday. Some other interesting insights:

· It was one woman's overall view (she was once CFO of the State Trade Organization, i.e. a high up position, before being forced out) that the ruling party has somewhat of a vested interest in keeping the islanders in poverty so that the administration can continue to buy their votes (at a cost of ~500 rufiya per vote).

o Not sure quite how much weight she put behind this statement, but the overall picture she painted was pretty bleak.

· The first democratically elected president, who was very popular and implemeted a lot of "positive" programs, was forced out after two years in a coup by the previous ruling party.

o The above woman was also forced out of her position at the same time.

· The ruling party, back in power now, immediately repealed many of these programs.

o One of which involved kicking out a company making improvements to the airport

o This resulted in an arbitration case that the Maldivian government lost, meaning they now owe the company $250 million

o The government finances are now very bad, to the point there is talk (rumors?) of them selling off whole atolls

o Practically, this also impacts residents directly: energy used to be subsidized by ~40%, until this year (I'm assuming these things are connected, though no one explicitly said that)

· Overall, the political situation sounds pretty rough, and very much a "who you know" environment. Coming in and trying to straight up outcompete one of the bottled water companies seems unlikely to work for this (and probably other) reasons. Seems like any implementation scheme would need to be very carefully thought out (politically) and implemented with the right partners.

o On the plus side, UNDP is one of those critical partners.

Best,
Matt

WHO Meeting Notes 2017-1-15

Participants

Dr. Shushil Dev Pant, Medical Officer – Public Health

Ms. Aishath Thimna Latheef, National Professional Officer (Health and Environment)

Matthew Rosen, MIT

Notes

- Sea-waste management close to groundwater is an issue
- There is some uncertainty about bottled water quality, WHO thinks perhaps poor at times
- Some cement tanks remain on islands (not the norm though)

- Broadly speaking, households have a tank(s)
- Schools, government offices, etc. have rainwater collection
- Community systems also exist in some places which might constitute 4-5 tanks connecting with piping (under a structure to collect rainwater)
    - For drinking purposes
- A few places use bottle water
- LECReD program on Laamu
    - UNOPS installed rainwater system
    - Has a quality control component integrated
- Councils are similar throughout the country (i.e. generally speaking, can assume conditions will be similar on islands with similar resource levels. For example: two islands without RO systems can be expected to have roughly similar issues)
- Public/community tanks are often used for non-drinking purposes (e.g. cooking, agriculture, washing)
    - NOTE: other groups (including local councils) have said many people will drink water from community systems. This seems to be somewhat island dependent, and is likely impacted by local need, how well maintained the system is, etc.)
    - Schools, government offices, health center systems ARE generally well-maintained and people drink from them.
    - NOTE: we later learned that IWRM systems actually pump water from these public facilities back to the water plant, treat it with UV, and then combine with RO water.
    - Fishermen/boats use water from community systems and have a lower bar for quality then local population.
- WHO's main focus related to water is how quality and safety are assured
- Local councils may be interested in WISPS
- Households may be interested in WISPS
- ~5 L per day for drinking may be sufficient
    - NOTE: not entirely clear if they said 5 L for drinking or 2 L for dinking + 3 L for other uses
- Would need to position a system away from septic outflow
- Most households have individual septic tanks
- Larger islands may have centralized septic areas/facilities
- The ground depth is very thin (surface to freshwater lens)
- Household waste systems empty directly to ground (and are typically not well maintained)
- In Malé, waste goes to sea
- Groundwater on islands may be used for cooking
- Rain water shortage (during dry period) is huge problem
- ~6 months rain, 6 months sun
- "Tanks are 500 – 1000 L"
    - NOTE: they didn't seem too sure about this number, and in fact most tanks we saw were 2500 L
- 186 inhabited islands in Malives
    - 500-3000 people per island
    - generally, 1000-1500 is average size

    - very few islands doing agriculture, but might be interested in WISPS
        - watering crops is huge challenge
        - famers typically dig well(s) for this purpose
- Generally, thinks WISPS could be a good buy
- Community tanks are often neglected (cats, rats, etc. present)
- Household level:
    - Raingwater for drinking
    - Well water for cooking, washing (2-3 wells per house)
        - Most houses have pumps
        - Otherwise, they'll use a cup on a stick
        - Households spending a lot of money on electricity for pumps (use 1 pump for 2-3 wells)
        - Sulfur dioxide builds up in wells and they smell, so often the wells are covered
- Each island has a generator
    - Household have meters
    - Prices for electricity are high
        - Prices higher than on Hulhumale (which starts at ~3.5 mvr/Kwh)
- When personal rainwater collection system runs out, people may buy bottled water.
    - More for kids, elderly, events
- In schools, they use rainwater collection
- Bottled water costs ~2.5 mvr/L
    - Increases in price the further away you go from Malé
- Bottled water plant is on Thlusdhoo (sp?)
- Shops on islands will sell bottled water
- With bad weather, transport becomes an issue
- If it rains heavily, islands flood and people will use bottled water as they worry about septic overflow to the ground.
    - WHO shares fear that groundwater is indeed being contaminated during flooding
- National defense force will deliver bottles with helicopters and boats
- Thinks it's a good idea to do a pilot test for WISPS
    - Need to convince Ministry of Environment and Ministry of Health
        - But mainly, need Ministry of Environment's sign off for the pilot
    - Safety is key
    - Needs to be environmentally friendly
    - Other groups of importance for pilot sign off:
        - EPA (they're under Ministry of Environment)
        - Local Government Authority (oversees island councils)
    - Thinks the councils should maintain systems
    - Costs should cover maintenance
- Government has plans to provide desalinated water to big islands and will likely charge a lot
    - Will take a long time to reach smaller islands
- Even on Hulhumale, water runs low during peak usage (Friday prayer time)
    - Bridge to Male will increase the population in Hulhumale and increase the shortage problem.

- In Male and Hulhumale, people don't drink the desalinated water due to bad perception (concern about quality of pipes). Water from plant is safe though.
- Ministry of Environment and Energy
    - Knows about desalination systems that are no longer on line
        - But generally, reasons for failure:
            - No ownership
            - No maintainence
            - Some islands now deserted

Key Stakeholders:

- MWSC, (public/private)
- Fenaka, (mostly private)
- UNOPS, (implementation organization)
- Ministry of Environment

Secondary Stakeholders:

- Maldives Food and Drug Authority
    - Regulatory, mainly to do with bottled water
    - Has water lab
- Ministry of Health
    - Preventative health activities
- National Disaster Management Center (was the one delivering boats of water when islands ran out)

Ministry of Environment and Energy, Water Department Notes 2017-1-17

Participants

Sobah, Ministry of Environment and Energy, Water Department

Mohamed Mustafa, Ministry of Environment and Energy, Water Department

Matthew Rosen, MIT

Notes

- General issues with groundwater:
    - High salinity
    - Contamination
- Land area on islands is at a premium
    - Shallows area or further offshore would be preferable (necessary?) for a system

- Questions over the distribution method for WISPS
- Generally interested in a pilot study
- Distribution systems
    - A piping system was installed in Male in the 90's
    - ~30 islands currently have piped systems
    - IWRM systems are piped
- Rainwater collection is minimal in IWRM systems, desalination high
- Consumption based fee for IWRM systems
    - Tiered tariff systems
    - 0-100 L is first tier
    - Quoted prices:
        - 22 rufiyaa/m^3 in Male
        - Up to 30 rufiyaa/m^3 in islands
            - Considered too high by islanders
                - some communities demand free water
            - Considered too low by service providers
        - **Why is 30 rufiyaa/m^3 considered expensive if bottled water is considered cheap?
- Fenaka came online as a service provider in 2008
- Stelco (State Electric Company) and MWSC are also island service providers (each of the three maintain different regions)
- There were ~57 desalination plants donated after the tsunami, and many are not functional now, but this number is a little deceiving.
    - Systems ranged in size from 4-250 m^3
    - Some were temporary in nature (disaster response)
    - Some were idle (never installed)
        - some systems were not appropriate for conditions (i.e. brackish water systems donated by Israel)
    - Other reasons systems went offline
        - No spare parts were available
        - Fenaka (and other service providers) were not there to maintain them
        - There was no operational capacity on the island level
        - No human resources
        - Government carried out some training
- ~30 islands now with desalination systems (local islands, not including resorts)
- Suggestion that we go to a new island if doing a pilot test
- Each island shares human resources for maintaining infrastructure systems
    - The same person managing the generator would also be trained on desalination system
- All islands have diesel power plants
- Current RO systems may occupy 25-30 m x 25-30 m square
- Some islands have STP waste management system for waste water
    - Waste has some incubation time

WISPS system

- Concerns
  - Blocking currents (depending on supporting infrastructure requirements)
  - Biodiversity issues
  - Outside of reef, the water gets very rough (crashing waves)
    - Even the inside of reefs can sometimes get rough
- There are some inland water bodies on some islands that might be possible to explore

Maalhos Council, Meeting Notes 2017-1-19

Participants

Meethen, Maalhos Council member

Suja, Maalhos Council President

Mujey, Maalhos Council member

Matthew Rosen, MIT

David Beirman, MIT

Notes

- Maalhos has a new 10 ton RO plant (installed last year)
- Typically, they run out of rainwater around April
- Rain begins in June
- Every year, water was brought from Male (until RO system was installed)
  - 25-30 tons (delivered by Disaster Management)
  - Maalhos residents would drink this water (but some other islands they know of would not due to contamination fears, etc.)
- Received a grant for tourism adaptation program and new RO plant will provide water to guesthouses on the island
  - Sonewafushi, a nearby Eco-resort has donated a 2nd pass RO system, UV-filter, and glass bottle cleaning equipment to Maalhos. Joint Venture, where Sonewafushi will maintain the bottling system
    - [Sonewafushi was one of the first resorts to bottle their own water (nearly every resort now does this), and they're viewing the Maalhos bottling system as a potentially replicable model on other islands, though this would have been less feasible if Maalhos didn't already have a grant for the first stage RO system]

    - Maalhos will be provide guest houses with glass bottled water, instead of normal plastic bottles at a fee (thought is that this fee will sustain maintenance, etc.)
    - Will fill smaller bottles (1 pint) and larger (~20 L) plastic drums.
    - Public are not charged for non-bottled water, but they'll be able to charge for the glass-bottled water
- Electricity for desalination plant provided by diesel plant on island
- Also received a grant to install solar on the RO house from UNDP (being installed now)
    - 15 kW panels
    - 10 kW battery bank
    - All pumps/equipment total usage is 12 kW, but they're not all in use at once
    - MARS, a local NGO (a few of the same people on the council run the NGO) operate the RO and power plant
- MARS = Maalhos Awareness and Recreation Society (group that applied for the grant)
- UNDP grant was $65,000 USD / 1.3 million MVR
    - Includes: RO plant, batteries, solar PV
- Living population on Maalhos = 550-600 people
- Registered population = 700 people
- During rainy season, RO plant is run once a month, and produces 10,000 L (10,000 L/day plant)
- During dry season, they may run the plant every day.
- When use is low, they may turn it on as a maintenance precaution
- Currently, producing water at ~230-235 ppm
- 4 community taps around the island that are piped to RO plant
    - Water is free for residents
    - Plan to charge guesthouses for use when that goes online
- There's been a lot of change here in the last 3 years
- Received a grant from Biowaste Reserve
    - Composting facility
    - Recycling solid waste (that they sell)
    - Hope to recycle glass next (with support from Sonewafushi who has glass making facilities, etc.)
- Bottled water costs on Maalhos:
    - 3 mvr / pint
    - 6 mvr / 1.5 liter
- Money spent on water?
    - 100 mvr/week during dry season
    - 1 case of bottles = 65 rufiyaa
- "Maldivians don't have a habit of drinking a lot of water"
- Dharavandhoo has RO plant, but it's not working
    - RO plant was from Red Cross, post tsunami
- Eydhafushi also has an RO plant that's not working
- Dharavandhoo and Eydhafushi have community rainwater tanks
- Hithadoo has a working RO plant
    - Production cost is high
    - No storage

    - Most houses have tank
- In general, Maalhos (and others') well water is used for bathing, but is contaminated
    - People will use an aeration pump to minimize the smell
    - Estimate that 70% of well water is contaminated
    - Every house has septic tanks that drains to the land
- Every house has wells and a pump [generally, seems like most houses in Maldives have this]
- Power Plant on Maalhos has 4 generators (only two used at once):
    - 128 kW
    - 150 kW
    - 89 kW
    - 100 kW
- Electricity costs
    - 3.5 mvr/kWh for 0-100 units (residential)
    - 4.5 mvr/kWh for 100-200 units, etc. up to 7 mvr/kWh (residential)
    - 500 units and above has additional fee
    - 7 mvr/kWh for businesses
- Roughly 100 houses on Maalhos
- Some mechanics on Eydhafushi (nearby)
- Some blackouts occur (2 hrs last week), but not with very high frequency
- Gov. plans to implement 30% solar throughout the country
- 1 person operates RO plant
- Gas is used for cooking, before it was firewood
    - 13 kg = 265 mvr [not sure if this was for a canister or what exactly]
- Local economy
    - Most men work in nearby resorts
    - Some work in gov. offices, schools, health center, fenaka, etc.
    - Women do thatch weaving of palm leaves (for roofs) and sell them to resorts
        - 4 pieces of 5 ft. length sold for 85 mvr
        - 1 piece takes 1 hour to make
        - So -> 21.25 mvr/hour
    - Some fishing, but not a lot anymore
- Maalhos has a strong relationship with nearby Sonewafushi resort, but it sounds like this is atypical
- There's a ferry that runs to Sonewafushi in the morning and evening, so residents can commute each day
- In May, tides begin to rise, peak 2 month later, then retreat for 2 months
- Weather apps:
    - Windguru.cz
    - Tides app
- Groundwater used for bathing is smelly, so they use aerators
- "rainwater is not as clean as RO water"
- Water sent from Male Disaster Management Center is heavy water
- Space is a concern for a WISPS system

- Production of WISPS (4-5 L/m^3) seen as too low for overall use on Maalhos, but maybe possible just for drinking water
- Goidhoo was recommended to check out because of inland/protected lagoons, and more overall area
- Also, Maalhendhoo recommended (north province)
- Fonodoo Bainfon [sp?]
    - ~100 people
- When Maalhos did a survey for new RO system, they used the following numbers:
    - 400 L/house/day (for all purposes)
    - ~6-7 people/house (some have more)
    - 550-600 people living on island
    - 700 people registered on island
    - <50 L/house/day
- For rainwater,
    - When drinking RW, people don't want to think about quality and don't want to test it
        - Acknowledgement from Suja (president) that the roofs are rusty and the water may not be particularly safe to drink
    - But because there is not much alternative, they don't test it
- Suja did a training at Koika (Korea International Asssociation....?) where someone presented data on RW quality from roofs on Maalhos in Alif Alif atoll [different island with same name] and found copper, zinc, iron contaminants
- Household level, RW is only filtered with a cloth
- Long term health implications
    - Kidney and heart problems are very common recently
- A couple households (2-3) only drink bottled water (but this is expensive)
- RW also used for cooking
- Coating on tin roofs comes off and gets into RW
- Some filters are available
    - In-line electric filters can be found in use on Eydhafushi, but not Maalhos
- RW tanks typically not raised above ground very much
- Maalhos is selling off a section of land for a resort at cost of 9.6 million mvr
- Government gives Maalhos 350,000 mvr for electricity bill, but now that they've installed meters on public lights, etc. they only actually use 120,000 mvr for electricity.
    - The rest of the funds they use for development projects (otherwise, the funding they get directly for development projects is 1500 mvr (i.e. negligible))
    - Typically, they request 500,000 mvr (and get 350,000 allocated)

Goidhoo Council, Meeting Notes 2017-1-21

Participants

Meethen, Maalhos Council member (travelled with us)

Mohamed Amir, Goidhoo Council president

Matthew Rosen, MIT

David Beirman, MIT

Notes

- Rainwater used for drinking
- Groundwater use for other (washing, (cooking?))
- Short of rain from Feb-April
- RO plant is spec'd at 10 tons/day capacity, but practically can only produce 5 tons/day
    - Provided free of charge
    - Council incomes pay for RO plant diesel
    - Plant is currently non-functional
        - Requested repairs from the Ministry of Environment, but hasn't happened
    - Plant was donated after tsumani
    - Typically, they'll use it 2-3 month/year
        - but it's been broken for a year (they haven't quite hit the point where they would turn it on)
    - No solution in place for upcoming drought (assumption that island will run out of water in Feb/March)
    - Gov. sends boat from Male with 30,000 L water at a "higher overall cost" than it would be to fix the RO system (i.e. other dynamics at play other than just lowest cost solution)
        - People on Goidhoo do not use this delivered water (though this was last year when the plant was online and they had an alternative option)
        - Estimated >25,000 mvr/boat to deliver water
    - They run a separate generator for the RO system
    - 1 ton water produced takes 2.2 hours to produce
- A lot of people are using bottled water, despite it being expensive
    - More among families with members working at resorts (more income)
    - Estimated intake: 6 x 1.5 L bottles/day (cost of 42 mvr)
    - Salaried people (gov. employees, etc.) are also buying
    - Non-salaried people are not buying as much water
- Community rainwater system was installed by the council (12,700 L capacity (7 tanks))
- 30,000 L -> drinking and cooking [Note: not clear from notes what this number is exactly referring to, may be overall community RW capacity]
- ~100 houses on island
- 793 people
- Fehandhoo ~300 people
- Filhado ~400-500 people

- Goidhoo provides RO water to these nearby islands during dry period
- Goidhoo has solar for 50% of community demand, but it's not fully installed yet (gov. implemented a large solar farm, but hasn't connected to battery bank yet.
    - Assumption that this is for political reasons (i.e. they'll connect it just before the next election)
        - Battery house was also built very far away from solar panels, making connection line more expensive than necessary
    - 130 kW plant
    - Very little coordination between implementing ministries and local councils
    - General procedure for new projects: a Parlimentary Member will advocate for a project, and if approved, the Ministry of Environment will allocate land, they'll show up and claim it.
        - Very poor communication between gov. and local councils
    - Local workers still haven't been paid for work on solar installation
- With new government (after Nashid), prices have basically doubled for electricity and other basic food staples
    - Fenaka's household fee starts at 3.5 rf/kWh
    - Business fee is 7.5 rf/kWh
    - An average business may use ~400 kWh/month [this was some specific example, not sure what] at rate of 5.5 -7.5 mvr/kWh
    - [A fair amount of solar installation was donated by UNDP and ADB under Nashid's government, but Fenaka comes in to manage and maintain system afterwards, and little savings is passed onto residents]
    - Nashid had subsidies
        - For food
        - Electricity for businesses was 3.5 rf/kWh
- RO plant uses 20 L/day diesel to produce 5000 L water
- ~10-11 mvr/L diesel
    - So water cost (only including fuel) is ~$2.6 – 2.9 /m^3
- RO maintenance:
    - Last fix they had to do was 37,000 mvr
    - Current fix needed is somewhat major (membranes, meters, pipes, sandfilter) and is projected to cost 200,000 mvr (which the council doesn't have funds for)
    - Mechanic would need to come from Male to repair system
- Water use per household:
    - Approximately 50 L for drinking and cooking
- Groundwater has changed in smell and color in the last 4-5 years
- Some houses have 2 rainwater tanks (2500 L each)
- Council could maintain a WISPS system
- Fenaka could as well but would charge
- Would need 5000 L/day (what their RO system was doing)
- "Spend 6000 mvr/year on diesel for RO"
- Dry Nov – May (starts to rain in June)
    - Need for RO water starts in April
- There are some inland protected lagoon type areas on Goidhoo that could be ideal for WISPS deployment

- However some are protected by biosphere reserve (or similar group), so not sure whether or not it would be allowed
- Generally open to doing a pilot
- If water is coming from those sources, some work would need to be done to convince public it was safe (not a good reputation currently)
- Lagoon areas are saltwater and move with tides, but protected
- Some areas have tanks nearby, otherwise would need to install or run piping to existing RO tanks for storage
- Would need solar panel and pump to run in those locations

References

1. Pollard, D. & DeConto, R. M. Contribution of Antarctica to past and future sea-level rise. *Nature* **531,** 591–597 (2016).
2. Hartmann, D. L. & Tank, A. K. Climate Change 2013 the Physical Science Basis: Working Group I Contribution to the Fifth Assessment Report of the Intergovernmental Panel on Climate Change. *Cambridge ...* (2013).
3. Hauer, M. E., Evans, J. M. & Mishra, D. R. Millions projected to be at risk from sea-level rise in the continental United States. *Nature Climate change* **6,** 691–695 (2016).
4. Mekonnen, M. M. & Hoekstra, A. Y. Four billion people facing severe water scarcity. *Science Advances* **2,** e1500323–e1500323 (2016).
5. Energy, U. R. *Water Desalination Using Renewable Energy*. (IRENA, 2012).
6. Administration, U. S. E. I. International Energy Outlook 2016. 1–290 (2016).
7. Michael Ratner, C. G. U.S. Energy: Overview and Key Statistics. 1–40 (2014).
8. Weiss, W. & Mauthner, F. Solar Heat Worldwide. 1–63 (2012).
9. Weinstein, L. A. *et al.* Concentrating Solar Power. *Chem. Rev.* acs.chemrev.5b00397 (2015). doi:10.1021/acs.chemrev.5b00397
10. William, M., Thomas, E. & Franke, O. *Sustainability of ground-water resources*. (US Geological Survey Circular, 1999).
11. OsmanoÄŸlu, B., Dixon, T. H., Wdowinski, S., Cabral-Cano, E. & Jiang, Y. International Journal of Applied Earth Observation and Geoinformation. *International Journal of Applied Earth Observations and Geoinformation* **13,** 1–12 (2011).
12. Pérez-González, A., Urtiaga, A. M., Ibáñez, R. & Ortiz, I. State of the art and review on the treatment technologies of water reverse osmosis concentrates. *Water Research* **46,** 267–283 (2012).
13. Malaeb, L. & Ayoub, G. M. Reverse osmosis technology for water treatment: state of the art review. *Desalination* **267,** 1–8 (2011).
14. PAUL, D. Reformulation of the solution-diffusion theory of reverse osmosis. *Journal of Membrane Science* **241,** 371–386 (2004).
15. Research on Corrosion Factors and Corrosion Prevention Measure of Carbon Steel in Produce Water of Reverse Osmosis in Power Plant. in
16. Fritzmann, C., Löwenberg, J., Wintgens, T. & Melin, T. State-of-the-art of reverse osmosis desalination. *DES* **216,** 1–76 (2007).
17. Vrijenhoek, E. M., Hong, S. & ELIMELECH, M. Influence of membrane surface properties on initial rate of colloidal fouling of reverse osmosis and nanofiltration membranes. *Journal of Membrane Science* (2001).
18. Li, Q. *et al.* Antimicrobial nanomaterials for water disinfection and microbial control: Potential applications and implications. *Water Research* **42,** 4591–4602 (2008).
19. Greenlee, L. F., Lawler, D. F., Freeman, B. D., Marrot, B. & Moulin, P. Reverse osmosis desalination: Water sources, technology, and today's challenges. **43,** 2317–2348 (2009).
20. Matin, A., Khan, Z., Zaidi, S. & Boyce, M. C. Biofouling in reverse osmosis membranes for seawater desalination: phenomena and prevention. *Desalination* (2011). doi:10.1016/j.desal.2011.06.063
21. Baker, J. S. & Dudley, L. Y. Biofouling in membrane systems - A review. *Desalination*

1–9 (1998).
22. Wright, N. C. & Winter, A. G. Justification for community-scale photovoltaic-powered electrodialysis desalination systems for inland rural villages in India. *Desalination* (2014). doi:10.1016/j.desal.2014.07.035
23. Miller, J. E. Review of water resources and desalination technologies. *Sandia national labs unlimited release report ...* (2003).
24. Warsinger, D. M., Swaminathan, J., Guillen-Burrieza, E., Arafat, H. A. & Lienhard, J. H., V. Scaling and fouling in membrane distillation for desalination applications: A review. *Desalination* **356,** 294–313 (2015).
25. Summers, E. K. Development of energy efficient membrane distillation systems. (2013).
26. Summers, E. K., Enright, R. & Lienhard, J. H. Solar-Driven Air Gap Membrane Distillation System. (2013).
27. Camacho, L. *et al.* Advances in Membrane Distillation for Water Desalination and Purification Applications. *Water* **5,** 94–196 (2013).
28. Meindersma, G. W., Guijt, C. M. & de Haan, A. B. Desalination and water recycling by air gap membrane distillation. *Desalination* **187,** 291–301 (2006).
29. Ashoor, B. B., Mansour, S., Giwa, A., Dufour, V. & Hasan, S. W. Principles and applications of direct contact membrane distillation (DCMD): A comprehensive review. *Desalination* **398,** 222–246 (2016).
30. Chung, H. W., Swaminathan, J., Warsinger, D. M. & Lienhard, J. H., V. Multistage vacuum membrane distillation (MSVMD) systems for high salinity applications. *Journal of Membrane Science* **497,** 128–141 (2016).
31. Lu, Y. & Chen, J. Optimal Design of Multistage Membrane Distillation Systems for Water Purification. *Ind. Eng. Chem. Res.* **50,** 7345–7354 (2011).
32. Zhao, K. *et al.* Experimental study of the memsys vacuum-multi-effect-membrane-distillation (V-MEMD) module. *Desalination* **323,** 150–160 (2013).
33. Borsani, R. & Rebagliati, S. Fundamentals and costing of MSF desalination plants and comparison with other technologies. *Desalination* **182,** 29–37 (2005).
34. Husain, A., Woldai, A., Adel, A., Kesou, A. & Borsani, R. Modelling and simulation of a multistage flash (MSF) desalination plant. *Desalination* (1994).
35. El-Dessouky, H. T., Ettouney, H. M. & Al-Roumi, Y. Multi-stage flash desalination: present and future outlook. *Chemical Engineering ...* (1999).
36. Morel, F. & Hering, J. G. *Principles and Applications of Aquatic Chemistry.* (John Wiley & Sons, 1993).
37. Flemming, H. C. Biofouling in water treatment. *Biofouling and Biocorrosion in Industrial Water ...* (1991).
38. Wittholz, M. K., O'Neill, B. K., Colby, C. B. & Lewis, D. Estimating the cost of desalination plants using a cost database. *Desalination* **229,** 10–20 (2008).
39. Ghaffour, N., Missimer, T. M. & Amy, G. L. Technical review and evaluation of the economics of water desalination: current and future challenges for better water supply sustainability. *Desalination* **309,** 197–207 (2013).
40. Ahmed, M., Shayya, W. H., Hoey, D. & Mahendran, A. Use of evaporation ponds for brine disposal in desalination plants. *Desalination* (2000).
41. Lee, K. & Neff, J. *Produced Water.* (Springer Science & Business Media, 2011).
42. Haluszczak, L. O., Rose, A. W. & Kump, L. R. Geochemical evaluation of flowback brine from Marcellus gas wells in Pennsylvania, USA. *Applied Geochemistry* **28,** 55–61

(2013).
43. Jiang, M., Hendrickson, C. T. & VanBriesen, J. M. Life Cycle Water Consumption and Wastewater Generation Impacts of a Marcellus Shale Gas Well. *Environ. Sci. Technol.* **48,** 1911–1920 (2014).
44. Folger, P. & Tiemann, M. *Human-Induced Earthquakes from Deep-Well Injection: A Brief Overview*. 1–26 (Congressional Research Service, 2015).
45. Office, U. G. A. *Information on Shale Resources, Development, and Environmental and Public Health Risks*. 1–70 (2012).
46. Nowak, N. C. & Bradish, J. High Density Polyethylene (HDPE) Lined Produced Water Evaporation Ponds. 1–7 (2015).
47. National Weather Service. *Evaporation Atlas for the Contiguous 48 United States*. 1–41 (US Department of Commerce, 2007).
48. Ettouney, H. M., El-Dessouky, H. T. & Faibish, R. S. Evaluating the economics of desalination. *Chemical Engineering …* (2002).
49. Grandjean, A. Water requirements, impinging factors and recommended intakes. *ILSI North America* (2004).
50. Hanson, A. *et al.* Distillate water quality of a single-basin solar still: laboratory and field studies. *Solar Energy* **76,** 635–645 (2004).
51. Abu-Hijleh, B. A. & Rababa'h, H. M. Experimental study of a solar still with sponge cubes in basin. *Energy Convers. Manage.* **44,** 1411–1418 (2003).
52. Nafey, A. S., Abdelkader, M., Abdelmotalip, A. & Mabrouk, A. A. Enhancement of solar still productivity using floating perforated black plate. *Energy Convers. Manage.* **43,** 937–946 (2002).
53. Delano, W. Solar still with floating slab-supporting particulate radiant energy receptor. (1970).
54. Al-Karaghouli, A. A. & Minasian, A. N. A floating-wick type solar still. *Renewable Energy* **1,** 77–79 (1995).
55. Minasian, A. N. & Al-Karaghouli, A. A. An improved solar still: the wick-basin type. *Energy Convers. Manage.* **36,** 213–217 (1995).
56. Janarthanan, B., Chandrasekaran, J. & Kumar, S. Performance of floating cum tilted-wick type solar still with the effect of water flowing over the glass cover. *Desalination* **190,** 51–62 (2006).
57. Mahdi, J. T., Smith, B. E. & Sharif, A. O. An experimental wick-type solar still system: Design and construction. *Desalination* **267,** 233–238 (2011).
58. Abu-Hijleh, B. A. Enhanced solar still performance using water film cooling of the glass cover. *Desalination* **107,** 235–244 (2002).
59. El-Bahi, A. & Inan, D. Analysis of a parallel double glass solar still with separate condenser. *Renewable Energy* **17,** 509–521 (1999).
60. Kumar, S. & Tiwari, G. N. Life cycle cost analysis of single slope hybrid (PV/T) active solar still. *Applied Energy* **86,** 1995–2004 (2009).
61. Tiwari, G. N., Thomas, J. M. & Khan, E. Optimisation of glass cover inclination for maximum yield in a solar still. *Heat Recovery Systems and CHP* (1994).
62. Mukherjee, K. & Tiwari, G. N. Economic analyses of various designs of conventional solar stills. *Energy Convers. Manage.* 1–3 (2003).
63. Al-Hinai, H., Al-Nassri, M. S. & Jubran, B. A. Parametric investigation of a double-effect solar still in comparison with a single-effect solar still. *DES* **150,** 75–83 (2002).

64. Ranjan, K. R. & Kaushik, S. C. Economic feasibility evaluation of solar distillation systems based on the equivalent cost of environmental degradation and high-grade energy savings. *International Journal of Low-Carbon Technologies* ctt048 (2013). doi:10.1093/ijlct/ctt048
65. Bohn, M. S. & Wang, K. Y. Experiments and analysis on the molten salt direct absorption receiver concept. *J. Sol. Energy Eng.* **110,** 45–51 (1988).
66. Norton, B. *Harnessing Solar Heat.* **18,** 123–143 (Springer, 2013).
67. Thirugnanasambandam, M., Iniyan, S. & Goic, R. A review of solar thermal technologies. *Renewable and Sustainable Energy Reviews* **14,** 312–322 (2010).
68. Machinda, G. T., Chowdhury, S. P., Chowdhury, S., Kibaara, S. & Arscott, R. Concentrating solar thermal power technologies: A review. in 1–6 (IEEE, 1981). doi:10.1109/INDCON.2011.6139512
69. Tian, Y. & Zhao, C. Y. A review of solar collectors and thermal energy storage in solar thermal applications. **104,** 538–553 (2013).
70. Neumann, O. *et al.* Solar Vapor Generation Enabled by Nanoparticles. *ACS Nano* **7,** 42–49 (2013).
71. Bogaerts, W. F. & Lampert, C. M. Materials for photothermal solar energy conversion. *J. Mater. Sci.* **18,** 2847–2875 (1983).
72. Zhang, Q.-C. Recent progress in high-temperature solar selective coatings. *Sol. Energy Mater. Sol. Cells* **62,** 63–74 (2000).
73. Mills, D. Advances in solar thermal electricity technology. *Solar Energy* **76,** 19–31 (2004).
74. Kennedy, C. E. *Review of mid-to high-temperature solar selective absorber materials.* 1–58 (National Renewable Energy Laboratory Golden Colorado, 2002).
75. Agnihotri, O. P. & Gupta, B. K. *Solar selective surfaces.* **1,** (Wiley, 1981).
76. Kennedy, C. E.National Renewable Energy Laboratory (NREL). PROGRESS TO DEVELOP AN ADVANCED SOLAR-SELECTIVE COATING. 1–9 (2008).
77. Mahian, O., Kianifar, A., Kalogirou, S. A., Pop, I. & Wongwises, S. A review of the applications of nanofluids in solar energy. *Heat Mass Transf.* **57,** 582–594 (2013).
78. Zhai, Y. *et al.* Scalable-manufactured randomized glass-polymer hybrid metamaterial for daytime radiative cooling. *J. Sol. Energy Eng.* **124,** eaai7899 (2002).
79. Veeraragavan, A., Lenert, A., Yilbas, B., Al-Dini, S. & Wang, E. N. Analytical model for the design of volumetric solar flow receivers. *Heat Mass Transf.* **55,** 556–564 (2012).
80. Lenert, A., Zuniga, Y. S. P. & Wang, E. N. Nanofluid-based absorbers for high temperature direct solar collectors. in 499–508 (2010).
81. Lenert, A. & Wang, E. N. Optimization of nanofluid volumetric receivers for solar thermal energy conversion. *Solar Energy* **86,** 253–265 (2012).
82. Taylor, R. A., Phelan, P., Adrian, R., Gunawan, A. & Otanicar, T. Characterization of a Nanofluid Volumetric Solar Absorber/Steam Generator. in 1927–1936 (American Society of Mechanical Engineers, 2011).
83. Govorov, A. O. & Richardson, H. H. Generating heat with metal nanoparticles. *Nano Today* **2,** 30–38 (2007).
84. Carlson, M. T., Green, A. J. & Richardson, H. H. Superheating Water by CW Excitation of Gold Nanodots. *Nano Letters* **12,** 1534–1537 (2012).
85. Sanchot, A. *et al.* Plasmonic Nanoparticle Networks for Light and Heat Concentration. *ACS Nano* **6,** 3434–3440 (2012).

86. Tyagi, H., Phelan, P. & Prasher, R. Predicted Efficiency of a Low-Temperature Nanofluid-Based Direct Absorption Solar Collector. *J. Sol. Energy Eng.* **131,** 041004 (2009).
87. Taylor, R. A. *et al.* Applicability of nanofluids in high flux solar collectors. *J. Renewable Sustainable Energy* **3,** 023104 (2011).
88. Arai, N., Itaya, Y. & Hasatani, M. Development of a 'volume heat-trap' type solar collector using a fine-particle semitransparent liquid suspension (FPSS) as a heat vehicle and heat storage medium Unsteady, one-dimensional heat transfer in a horizontal FPSS layer heated by thermal radiation. *Solar Energy* **32,** 49–56 (1984).
89. Fend, T., Hoffschmidt, B., Pitz-Paal, R., Reutter, O. & Rietbrock, P. Porous materials as open volumetric solar receivers: Experimental determination of thermophysical and heat transfer properties. *Energy* **29,** 823–833 (2004).
90. Wijeysundera, N. E. & Thevendran, V. A two-dimensional heat transfer analysis of the thermal-trap collector. *Solar Energy* **40,** 127–133 (1988).
91. Fend, T., Pitz-Paal, R., Reutter, O., Bauer, J. & Hoffschmidt, B. Two novel high-porosity materials as volumetric receivers for concentrated solar radiation. *Sol. Energy Mater. Sol. Cells* **84,** 291–304 (2004).
92. Pitz-Paal, R., Hoffschmidt, B., Böhmer, M. & Becker, M. Experimental and numerical evaluation of the performance and flow stability of different types of open volumetric absorbers under non-homogeneous irradiation. *Solar Energy* **60,** 135–150 (1997).
93. Lansing, F. L., Clarke, V. & Reynolds, R. A high performance porous flat-plate solar collector. *Energy* **4,** 685–694 (1979).
94. Govorov, A. O. *et al.* Gold nanoparticle ensembles as heaters and actuators: melting and collective plasmon resonances. *Nanoscale Res. Lett.* **1,** 84–90 (2006).
95. Bertocchi, R., Karni, J. & Kribus, A. Experimental evaluation of a non-isothermal high temperature solar particle receiver. *Energy* **29,** 687–700 (2004).
96. Han, D., Meng, Z., Wu, D., Zhang, C. & Zhu, H. Thermal properties of carbon black aqueous nanofluids for solar absorption. *Nanoscale Res. Lett.* **6,** 1–7 (2012).
97. Miller, F. & Koenigsdorff, R. Theoretical analysis of a high-temperature small-particle solar receiver. *Sol. Energy Mater.* **24,** 210–221 (1991).
98. Otanicar, T. P., Phelan, P. E., Prasher, R. S., Rosengarten, G. & Taylor, R. A. Nanofluid-based direct absorption solar collector. *J. Renewable Sustainable Energy* **2,** 033102 (2010).
99. Boriskina, S. V., Ghasemi, H. & Chen, G. Plasmonic materials for energy: From physics to applications. *Mater. Today* **16,** 375–386 (2013).
100. Hogan, N. J., Urban, A. S., Ayala-Orozco, C. & Pimpinelli, A. Nanoparticles heat through light localization. *Nano Letters* **14,** 4640–4645 (2014).
101. Fang, Z. *et al.* Evolution of light-induced vapor generation at a liquid-immersed metallic nanoparticle. *Nano Letters* **13,** 1736–1742 (2013).
102. Lukianova-Hleb, E. *et al.* Plasmonic Nanobubbles as Transient Vapor Nanobubbles Generated around Plasmonic Nanoparticles. *ACS Nano* **4,** 2109–2123 (2010).
103. Saidur, R., Meng, T. C., Said, Z., Hasanuzzaman, M. & Kamyar, A. International Journal of Heat and Mass Transfer. *Heat Mass Transf.* **55,** 5899–5907 (2012).
104. Kim, S. J., Bang, I. C., Buongiorno, J. & Hu, L. W. Surface wettability change during pool boiling of nanofluids and its effect on critical heat flux. *International Journal of Heat and Mass Transfer* **50,** 4105–4116 (2007).

105. You, S. M., Kim, J. H. & Kim, K. H. Effect of nanoparticles on critical heat flux of water in pool boiling heat transfer. **83,** 3374 (2003).
106. Lombard, J., Biben, T. & Merabia, S. Kinetics of Nanobubble Generation Around Overheated Nanoparticles. *Phys. Rev. Lett.* **112,** 105701 (2014).
107. Baral, S., Green, A. J., Livshits, M. Y., Govorov, A. O. & Richardson, H. H. Comparison of Vapor Formation of Water at the Solid/Water Interface to Colloidal Solutions Using Optically Excited Gold Nanostructures. *ACS Nano* **8,** 1439–1448 (2014).
108. Baffou, G., Polleux, J., Rigneault, H. & Monneret, S. Super-Heating and Micro-Bubble Generation around Plasmonic Nanoparticles under cw Illumination. *J. Phys. Chem. C* **118,** 4890–4898 (2014).
109. Kotaidis, V., Dahmen, C., Plessen, von, G., Springer, F. & Plech, A. Excitation of nanoscale vapor bubbles at the surface of gold nanoparticles in water. *J. Chem. Phys.* **124,** 184702 (2006).
110. Keblinski, P., Cahill, D. G., Bodapati, A., Sullivan, C. R. & Taton, T. A. Limits of localized heating by electromagnetically excited nanoparticles. *J. Appl. Phys.* **100,** 054305 (2006).
111. Montes, M. J., Abánades, A. & Martínez-Val, J. M. Performance of a direct steam generation solar thermal power plant for electricity production as a function of the solar multiple. *Solar Energy* **83,** 679–689 (2009).
112. Kelly, B., Hermann, U. & Hale, M. Optimization studies for integrated solar combined cycle systems. in 393–398 (2001).
113. Quaschning, V. & Ortmanns, W. Specific Cost Development of Photovoltaic and Concentrated Solar Thermal Systems Depending on the Global Irradiation–A Study Performed with the Simulation environment, GREENIUS. in 14–19 (2003).
114. Resch, G. *et al.* Potentials and cost for renewable electricity in Europe. *Report (D4) of the IEE project OPTRES: Assessment and optimisation of renewable support schemes in the European electricity market* 35 (2006).
115. O'Gallagher, J. J. *Nonimaging Optics in Solar Energy*. **2,** 1–120 (Synthesis Lectures on Energy and the Environment: Technology, Science, and Society, 2008).
116. Kolb, G. J., Ho, C. K., Mancini, T. R. & Gary, J. A. *Power Tower Technology Roadmap and Cost Reduction Plan.* 1–38 (Sandia National Lab, 2011).
117. Neumann, O. *et al.* Compact solar autoclave based on steam generation using broadband light-harvesting nanoparticles. *Proc. Natl. Acad. Sci. U. S. A.* **110,** 11677–11681 (2013).
118. Su, C.-Y. *et al.* High-Quality Thin Graphene Films from Fast Electrochemical Exfoliation. *ACS Nano* **5,** 2332–2339 (2011).
119. Trisaksri, V. & Wongwises, S. Critical review of heat transfer characteristics of nanofluids. *Renewable and Sustainable Energy Reviews* **11,** 512–523 (2007).
120. Buongiorno, J. *et al.* A benchmark study on the thermal conductivity of nanofluids. *J. Appl. Phys.* **106,** 094312 (2009).
121. Xie, W. T., Dai, Y. J., Wang, R. Z. & Sumathy, K. Renewable and Sustainable Energy Reviews. *Renewable and Sustainable Energy Reviews* **15,** 2588–2606 (2011).
122. Taylor, R. A., Phelan, P. E., Otanicar, T. P., Adrian, R. & Prasher, R. Nanofluid optical property characterization: towards efficient direct absorption solar collectors. *Nanoscale Res. Lett.* **6,** 1–11 (2011).
123. Yu, W. & Xie, H. A Review on Nanofluids: Preparation, Stability Mechanisms, and Applications. *J. Nanomater.* **2012,** 1–17 (2012).

124. Fedele, L., Colla, L., Bobbo, S., Barison, S. & Agresti, F. Experimental stability analysis of different water-based nanofluids. *Nanoscale Res. Lett.* **6,** 1–8 (2011).
125. Hwang, Y. *et al.* Production and dispersion stability of nanoparticles in nanofluids. *Powder Technol.* **186,** 145–153 (2008).
126. Mehrali, M. *et al.* Investigation of thermal conductivity and rheological properties of nanofluids containing graphene nanoplatelets. *Nanoscale Res. Lett.* **9,** 1–12 (2014).
127. Modest, M. F. *Radiative Heat Transfer.* (Academic Press, 1993).
128. Stagg, B. J. & Charalampopoulos, T. T. Refractive indices of pyrolytic graphite, amorphous carbon, and flame soot in the temperature range 25 to 600 C. *Combust. Flame* **94,** 381–396 (1993).
129. Bergman, T. L., Levine, A. S., Incropera, F. P. & Dewitt, D. P. *Fundamentals of Heat and Mass Transfer.* (John Wiley & Sons, 2011).
130. Kerslake, D. M. *The Stress of Hot Environments.* (Cambridge University Press, 2011).
131. Chen, R.-H., Phuoc, T. X. & Martello, D. International Journal of Heat and Mass Transfer. *Heat Mass Transf.* **53,** 3677–3682 (2010).
132. Lee, S. *et al.* Experimental investigation of the latent heat of vaporization in aqueous nanofluids. **104,** 151908 (2014).
133. Huxtable, S. T. *et al.* Interfacial heat flow in carbon nanotube suspensions. *Nat. Mater.* **2,** 731–734 (2003).
134. Keblinski, P., Eastman, J. A. & Cahill, D. G. Nanofluids for thermal transport. *Mater. Today* **8,** 36–44 (2005).
135. Baffou, G. *et al.* Photoinduced Heating of Nanoparticle Arrays. *ACS Nano* **7,** 6478–6488 (2013).
136. Kim, H. Enhancement of critical heat flux in nucleate boiling of nanofluids: a state-of-art review. *Nanoscale Res. Lett.* **6,** 415 (2011).
137. Ghasemi, H. *et al.* Solar steam generation by heat localization. *Nature Communications* **5,** 1–7 (2014).
138. Downing, H. D. & Williams, D. Optical constants of water in the infrared. *Journal of Geophysical Research* (1975).
139. Quoilin, S., Orosz, M., Hemond, H. & Lemort, V. Performance and design optimization of a low-cost solar organic Rankine cycle for remote power generation. *Solar Energy* **85,** 955–966 (2011).
140. Delgado-Torres, A. N. M. & García-Rodríguez, L. Energy Conversion and Management. *Energy Convers. Manage.* **51,** 2846–2856 (2010).
141. Turgut, O. & Onur, N. An experimental and three-dimensional numerical study of natural convection heat transfer between two horizontal parallel plates. *International Communications in Heat and Mass Transfer* **34,** 644–652 (2007).
142. Globe, S. & Dropkin, D. *Natural convection heat transfer in liquids confined by two horizontal plates and heated from below.* (J. Heat Transfer, 1959).
143. Zhou, L. *et al.* 3D self-assembly of aluminium nanoparticles for plasmon-enhanced solar desalination. *Nature Photonics* 1–7 (2016). doi:10.1038/nphoton.2016.75
144. Liu, Z. *et al.* Extremely cost-effective and efficient solar vapor generation under nonconcentrated illumination using thermally isolated black paper. *Global Challenges* **1,** 1600003 (2017).
145. Kashyap, V. *et al.* A flexible anti-clogging graphite film for scalable solar desalination by heat localization. *J. Mater. Chem. A* **5,** 15227–15234 (2017).

146. Van der Bruggen, B. & Vandecasteele, C. Distillation vs. membrane filtration: overview of process evolutions in seawater desalination. in **143,** 207–218 (2002).
147. Kabeel, A. E. & El-Agouz, S. A. Review of researches and developments on solar stills. *Desalination* **276,** 1–12 (2011).
148. Kabeel, A. E., Hamed, A. M. & El-Agouz, S. A. Cost analysis of different solar still con. *Energy* **35,** 2901–2908 (2010).
149. Bhattacharyya, A. Solar stills for desalination of water in rural households. *International Journal of Environment and Sustainability* **2,** 21–30 (2013).
150. Lienhard, J., Antar, M. A., Bilton, A. & Blanco, J. Solar desalination. *Annual Review of Heat Transfer* 277–347 (2012).
151. Tleimat, B. W. & Howe, E. D. Comparison of plastic and glass condensing covers for solar distillers. *Solar Energy* **12,** 293–304 (1969).
152. Phadatare, M. K. & Verma, S. K. Effect of cover materials on heat and mass transfer coefficients in a plastic solar still. *Desalination and Water Treatment* **2,** 254–259 (2012).
153. Tow, E. W. The antireflective potential of dropwise condensation. *J. Opt. Soc. Am. A* **31,** 493 (2014).
154. Zhu, K., Huang, Y., Pruvost, J., Legrand, J. & Pilon, L. Transmittance of transparent windows with non-absorbing cap-shaped droplets condensed on their backside. *Journal of Quantitative Spectroscopy and Radiative Transfer* **194,** 98–107 (2017).
155. McAdams, W. H. *Heat Transmission.* (McGraw-Hill, 1954).
156. Shah, M. M. Analytical Formulas for Calculating Water Evaporation from Pools. (2008).
157. Bollen, S. Success in the Maldives. *Industrial Water & Wastes Digest* 10–12 (2014).
158. Ibrahim, M., Bari, M. R. & Miles, L. Water resources management in Maldives with an emphasis on desalination. *... of Maldives Available online at: http ...* (2002).
159. Rosen, M. F. & Bierman, D. IDEAS Maldives Market Research Trip, 2017. (2017).
160. Bailey, R. T., Khalil, A. & Chatikavanij, V. Assessing groundwater availability of the Maldives under future climate conditions. *Hydrol. Process.* **31,** 3334–3349 (2014).
161. Ayers, J. F. & Vacher, H. L. Hydrogeology of an atoll island: a conceptual model from detailed study of a Micronesian example. *Ground Water* (1986).
162. Bailey, R. T., Khalil, A. & Chatikavanij, V. Estimating Current and Future Groundwater Resources of the Maldives. *J Am Water Resour Assoc* **51,** 112–122 (2014).
163. Aulet, B. *Disciplined entrepreneurship: 24 steps to a successful startup.* (2013).